2019

PADDLE MIXER-EXTRUSION REACTOR FOR TORREFACTION AND PYROLYSIS

Stas Zinchik
Michigan Technological University, szinchik@mtu.edu

PADDLE MIXER-EXTRUSION REACTOR FOR TORREFACTION AND PYROLYSIS

By

Stas Zinchik

A DISSERTATION

Submitted in partial fulfillment of the requirements for the degree of

DOCTOR OF PHILOSOPHY

In Mechanical Engineering – Engineering Mechanics

MICHIGAN TECHNOLOGICAL UNIVERSITY

2019

This dissertation has been approved in partial fulfillment of the requirements for the Degree of DOCTOR OF PHILOSOPHY in Mechanical Engineering – Engineering Mechanics.

Department of Mechanical Engineering – Engineering Mechanics

Dissertation Co-Advisor:	*Dr. Ezra Bar-Ziv*
Dissertation Co-Advisor:	*Dr. Jordan L. Klinger*
Committee Member:	*Dr. Jeffrey D. Naber*
Committee Member:	*Dr. David R. Shonnard*
Committee Member:	*Dr. Armando G. McDonald*
Committee Member:	*Dr. Robert M. Baldwin*
Department Chair:	*Dr. William W. Predebon*

Table of Contents

List of figures

List of tables

Preface

This dissertation contains 7 chapters, as follows:

Chapter 1 provides the motivation for the research, a background that discusses current knowledge and torrefaction-pyrolysis and waste as a unique feedstock, and the thesis objectives. This chapter is based on the thesis defense document.

Chapter 2 is a comprehensive study on the paddle mixer where a small 25.4-mm (1-kg/hr) reactor was designed, built, tested and used for pyrolysis with biomass. This chapter was the basis of a published paper: ***Zinchik, S., Klinger, J. L., Westover, T. L., Donepudi, Y., Hernandez, S., Naber, J. D., & Bar-Ziv, E. (2018). Evaluation of fast pyrolysis feedstock conversion with a mixing paddle reactor. Fuel Processing Technology, 171, 124–132. https://doi.org/10.1016/j.fuproc.2017.11.012. Copyrights © 2018 Elsevier B.V.*** The lead of this work was S. Zinchik, with Klinger and Bar-Ziv as co-advisors, Westover and Hernandez feedstock preparation and some data analysis for pyrolysis, Donepudi helping with the experiment and data collection, and Naber for review and editing. Parts of this chapter are also based on a collaborative work with Ankith Ullal and presented in detail in: ***Ullal, A. (2017). HEAT TRANSFER ANALYSIS IN A PADDLE REACTOR FOR BIOMASS FAST PYROLYIS. In Dissertations, Master's Theses and Master's Reports. Retrieved from https://digitalcommons.mtu.edu/etdr/313***

Chapter 3 is a comprehensive study of industrial wastes as the main feedstock to be used in this thesis. This chapter includes characterization of the waste, its torrefaction at various conditions, reactor modeling and characterization of the torrefied waste. This chapter was the basis of a published paper: ***Xu, Z., Zinchik, S., Kolapkar, S. S., Conn, D.,***

Hansen, T., Bar-Ziv, E., & McDonald, A. G. (2018). Properties of Torrefied U.S. Waste Blends. Frontiers in Energy Research, 6(65), 1-13. doi.org/10.3389/fenrg.2018.00065. The lead of this study was Z. Xu, with Zinchik as a major contributor in experimental planning, data collection, and analysis, data interpretation, Kolapkar helping with experiment and data collection, Bar-Ziv as thesis advisor, Conn and Hansen as feedstock providers and characterization, McDonald helping in product characterization and interpretation.

Chapter 4 is a comprehensive study on the extrusion of non-torrefied and torrefied wastes studied in Chapter 3. It includes torrefaction, extrusion, characterization, and combustion. This chapter is the basis of a paper to be submitted for publication: ***Zinchik, S., Xu, Z., Kolapkar, S. S., Bar-Ziv, E., & McDonald, A. G. (2019). Properties of pellets of Torrefied U.S. Waste Blends. Waste Management***. The lead of this study is S. Zinchik, with Xu and Kolapkar contributors in experimental measurements and data collection, Bar-Ziv as thesis advisor, McDonald helping in extrusion, product characterization, and data interpretation.

Chapter 5 is the development of a 101.6-mm (100-kg/hr) integrated torrefaction-extrusion reactor that details a comprehensive study of this up-scaled integrated reactor system with in-depth study of the thermal dynamic behavior, residence time, heat transfer and the applicability of the system to torrefaction and pyrolysis. This chapter is the basis of a paper in preparation to be submitted to Waste Management: ***Zinchik, S., Kolapkar, S. S., Xu, Z., Bar-Ziv, E., & McDonald, A. G.. Paddle mixing-extrusion reactor***. The lead of this study is S. Zinchik, with Xu and Kolapkar contributors in experimental

measurements and data collection, Bar-Ziv as thesis advisor, McDonald helping in extrusion parameters, product characterization, and data interpretation.

Chapter 6 is the conclusion of the entire dissertation.

Chapter 7 is suggestions of future work with some preliminary experiments and simulations, specifically for fast heat transfer and pyrolysis.

Further, not included in this thesis the following studies that are currently in the state of papers in preparations:

Xu, Z., Kolapkar, S. S., Zinchik, S., Bar-Ziv, E., McDonald, A., "Comprehensive PVC Kinetic Modeling." To be submitted to Waste Management.

Albrecht, J., Xu, Z., Kolapkar, S. S., Zinchik, S., Bar-Ziv, E., McDonald, A., "Dechlorination of Industrial Wastes." To be submitted to Waste Management.

Acknowledgments

I would like to acknowledge the financial support I received from the Mechanical Engineering – Engineering Mechanics department at Michigan Tech, Battelle/INL (Contract #209856) and NSF-PFI.

I would like to acknowledge the mentoring of my co-advisors Dr. Ezra Bar-Ziv and Dr. Jordan L. Klinger. The opportunity to pursue this degree came from your sincere belief in my abilities. Without your guidance I will not be able to finish this work. The long discussion on many of the topics/problems have allowed me to develop the understanding of the physical and chemical phenomenon. This will serve me as a guide in the rest of my career, and I thank you!

I would like to acknowledge Dr. Jeffrey D. Naber, Dr. David R. Shonnard, Dr. Armando G. McDonald, and to Dr. Robert M. Baldwin for serving on my advisory committee, and for their careful review and support of my work. Your critical comments and discussions always kept my thoughts and research interpretations grounded, realistic, and focused.

I would like to acknowledge the many thoughtful discussions, contributions, and antics of my undergraduate research assistants (Josh Albrecht) and fellow/past graduate students, particularly Yashwanth Donepudi, Zhuo Xu, Shreyas Kolapkar.

I would like to acknowledge to acknowledge Universal Metal Works Co. and Michigan Tech machine shop for their support, time and technical help.

I would like to acknowledge my mom (Albina Zinchik), my dad (Gregori Zinchik), and my sister for their support in me to pursue this degree, I could not have done this without your patience and care.

Abstract

This work is focused on the fundamental understanding and the development of paddle mixer reactors (or modified screw augers). This work will contribute to the effort of thermal conversion of biomass and wastes. We developed and studied two paddle systems (i) 25-mm lab-scale (up to 1 kg/hr) and (ii) 101-mm pilot-scale (up to 100 kg/hr). Thermal behavior of the two systems was studied and it was estimated that the lab-scale system has high heating rate of up to 530 °C/s. Residence times were thoroughly measured and were determined as a function of rotation frequency and volume fraction. We also determined the specific process energy requirements and the specific heat of the material. Extensive pyrolysis experiments were carried out with many types of biomass. It was found that solid/liquid yields were comparable to those measured in circulating fluidized bed at NREL. Modification of the pilot-scale system are required to enhance the mass flow rates and the heating rate.

Fiber and plastic waste blends were thoroughly investigated in a mixture of 40% plastic and 60% fiber. Extensive torrefaction experiments were carried out and thermal and mechanical properties of the torrefied material were measured and correlated with mass loss. Degradation reaction of waste blends was modeled using a first order reaction. Excellent fit between the experimental and modeling results was obtained. Activation energy and pre-exponential factors were determined. One major finding was that the paddle mixer significantly increased the homogeneity of the waste blend and it is further increased as the size of the material reduces. Density was measured and found that at density of ~1200 kg/m^3, the water intake was 0.7% after 30 days of immersion in water. Extensive

grinding study was carried out with these torrefied waste blends and the grinding energy behavior was found similar to that of PRB coal. Heat content was measured, and it was shown that the initial heat content is ~30 MJ/kg and as the torrefaction process proceeds the value increases to ~35 MJ/kg at ~51% mass loss. Combustion experiments were carried out and showed that with the reduction of volatile matter (due to thermal degradation) the combustion time has increased.

1. Introduction

1.1. Motivation

Over the last few decades, there has been an increasing worldwide effort to study/stop/limit global warming and its effects. For these efforts to succeed, the use of renewable sources must be increased. Renewable sources are a resource that can be naturally replenished over the course of time. If the energy source is sustainable, it can be considered as having little to zero net effect on global warming. If used properly, renewable energy can be a source of a sustainable or unlimited source of power. Biomass is such a renewable energy source if managed properly, it can also be sustainable. Biomass is any organic material like plants or plant derivatives. The most common use of biomass is direct combustion, but recent technologies allow other conversions of biomass into fuels, chemical, etc.

There are two main pathways to produce renewable fuels from biomass: (i) Torrefaction, occurring at around 300°C, that can produce renewable solid fuel that can replace some of the coal; and (ii) fast pyrolysis, occurring in the temperatures range of 400-600°C, that can produce liquid fuels for transportation (the product of this technology is a black-brown liquid, as it presents a potential route for production of fuels with some properties similar to petroleum produced from crude oil).

Over recent years, the U.S. has implemented rulings with the common objective to reduce the harmful CO_2 emissions from fossil fuels. The new rulings, described in detail below, is designed to allow flexibility and a wide time frame to create a reliable, reasonable cost, and secure an alternative source of energy. In 2005 the U.S. Congress established the

Renewable Fuel Standard (RFS) as a section of the Energy Policy Act of 2005. This mandated that at least 4 billion gallons of renewable fuel be produced and used 2006 onwards. This was quickly amended and expanded two years later (RFSII) as part of broad energy policy reform described in the Energy Independence and Security Act of 2007 (EISA 2007). For solid fuels the EPA has released the final carbon emission guidelines in 2015 (US-EPA, 2015), known as the Clean Power Plant act, exerting an accelerated regulatory pressure on utilities utilizing coal. The EPA has proposed state by state goals to achieve CO_2 emission reductions from the power sector of approximately 30 percent from CO_2 emission levels in 2005. However, this guideline has been repealed by the Supreme Court in 2016 and replaced by the Affordable Clean Energy Act in Aug 2018. This act proposed a different pathway in order to reduce CO_2 emission by increasing efficiency of existing power plans and suggests a list of technologies that can help establish a "standard of performance".

In addition, the world has experienced a sharp increase in waste generation (World Bank, 2018). In 2015 the EPA released a waste composition report describing the U.S. waste composition and management operation. The U.S. waste composed mostly of fibers (paper cardboard) plastics and food. The majority of this waste is being landfilled (52%), the rest is being recycled (26%), used for energy production (13%), and composted (9%) (US-EPA, 2018). The recycled portion is anticipated to go down further after the recent (2018) China's ban on plastic import (Brooks, Wang, & Jambeck, 2018). On the other hand, there is a need for a clean, low-cost renewable fuel. This fuel can be generated from wastes as will be discussed in length in this work.

1.2. Background

1.2.1. Pyrolysis

The original RFS mandated that at least 4 billion gallons of renewable fuel be used in the national transportation fuel supply in 2006, with a steady quota growth to 7.5 billion gallons in use by 2012. Initially, this was met through the conversion of corn starch to ethanol through fermentation. The RFS was extended under Title II of EISA 2007 to expand not only the biofuels quotas (36 billion gallons by 2022) but also the types of biofuel allowable. These requirements were not only designed to promote usage of biofuels but to implement and to develop the advanced biofuels production methods. Of the 36 billion gallons of biofuels utilized by 2022, at least 21 billion gallons must be from advanced biofuels - or non-corn starch-based fuels that provide at least a 50% reduction in greenhouse gas emissions. In addition to conforming to the advanced biofuels regulations, at least 16 billion gallons must also be derived from cellulosic feedstock and provide at least 60% reduction in lifecycle greenhouse emissions and 1 billion gallons should be biomass-based biodiesel produced from non-esterification methods and provide at least 50% reduction in greenhouse gas emissions. Of these mandates, production of 16 billion gallons of fuels from cellulosic sources requires significant advancement and implementation of new technologies to successfully meet the requirements. Implementing regulation and enforcement of these standards was delegated to the U.S. Environmental Protection Agency (US-US-EPA, 2015).

In addition to the primary regulation, with RFSII, some states have also adopted a policy to enforce and/or promote the production and use of solid and liquid biofuels. In addition to the widely accepted tax credits and incentives for electric vehicles, fueling

infrastructure, and fuel economy regulations, some states have provided incentive programs and grants for the advancement of biodiesel and other advanced biofuels programs. As a specific example, Michigan offers an alternative fuel development property tax exemption where if the industrial property is used for high-technology fuel creation or advanced vehicle systems (in general electric or hybrid vehicles or alternative fuel generation), the site may be exempt from property taxes. Other states, such as California, have adopted their own low-carbon fuel use requirements. As dictated in the California Code of Regulations Title 17, out of total fuel purchased by the state government aggregately, 3% must be from low carbon sources starting January 1, 2017. In addition, the state has implemented the Low Carbon Fuel Standard (LCFS) program which mandates a minimum of 10% reduction in carbon intensity of fuels sold, supplied, or offered for sale by 2020.

One way of meeting these strict biofuels production requirements, specifically the advanced biofuels production from cellulosic sources, is by using pyrolysis. Fast pyrolysis is a high-temperature process around approximately 500°C in the absence of oxygen where the biomass components break down to form organic vapors. Upon cooling, these vapors form a brownish-black liquid referred to as pyrolysis oil or bio-oil. Pyrolysis offers a route to convert the low molecular weight substances (extractives) as well as the macromolecular structures (polysaccharides and lignin) into the liquid pyrolysis oil. Fast pyrolysis processes can generate 60-75 % oil, 15-25 % as solid char (mostly mineral matter and fixed carbon) and the remainder consists of gases such as carbon monoxide and carbon dioxide. Although the term "fast pyrolysis" is somewhat arbitrary, it is distinctly different from conventional pyrolysis which has been traditionally used to produce charcoal where very

slow and gradual heating of material is used. In addition to a fast heating rate, fast pyrolysis must also be accompanied by short vapor phase residence times (<2 s) and these vapors must be rapidly cooled to form the bio-oil.

According to Mohan, et al. (2006), bio-oil is a complex chemical mixture of species that has been suggested to contain well over 300 different chemical species (Mohan, Pittman, & Steele, 2006). The chemical groups identified within bio-oil include water, guaiacols, catecols, syringols, vanillins, furancarboxaldehydes, isoeugenol, pyrones, carboxylic acids, hydroxyaldehydes, hydroxyketones, sugars, anhydro-sugars, phenolics, other cyclic structures, hydrocarbons, and even oligomeric structures that are ejected from the biomass particle as aerosols, among others. A variety of techniques have been proposed to study the complex chemical nature, partially including gas chromatography (GC), gas chromatography-mass spectroscopy (GC-MS), high pressure liquid chromatography (HPLC), Fourier transform infrared spectroscopy (FTIR), electrospray ionization mass spectroscopy (ESI-MS), gel-permeation chromatography (GPC), small-angle neutron scattering (SANS), and nuclear magnetic resonance analysis (NMR). Typically, the woody biomass has an elemental composition of approximately 54-58%, 5.5-7.0%, and 35-40% carbon, hydrogen, and oxygen respectively. The liquid produced have high oxygenation levels originating from the highly oxygenated original biomass material and results in a liquid that is viscous (7-90 cSt at 50°C), acidic (pH ~2.5), and has a heating value (19.5 MJ/L) approximately half that of light or heavy fuel oil. The chemical composition and resulting physical properties depend primarily on the parent biomass materials and the conditions and production system through which it was generated. While the raw biomass is typically not variable (given economic constraints and outside of incremental changes

achievable through biological means of genetic modification or directed evolution) the process conditions and technology can be adapted to ensure efficient conversion to a liquid product (Mohan et al., 2006).

1.2.2. Torrefaction

With the reduced utilization of coal (US-EPA, 2015) and the tightening regulations, there is a demand for drop-in fuel. More specifically for solid fuels that boilers are designed to operate with (Broström, Nordin, Pommer, Branca, & Di Blasi, 2012). The best way is to use a drop-in fuel that has similar properties to coal and will require minimal changes to the feeding systems or any of the supply chain infrastructure. Such fuel can be produced through a thermochemical conversion of biomass known as torrefaction. Torrefaction is thermal degradation process that occurs in the range of 200°C to 350°C without the presence of oxygen (Chew & Doshi, 2011; Shankar Tumuluru, Sokhansanj, Hess, Wright, & Boardman, 2011). Torrefaction mostly focuses on the production of solids (60-90% yield), the rest is released as gas. While the gas stream contains mainly water, aldehydes, organic acids, and other gases (such as CO_2). The solid fraction contains 5-20 % more carbon and in turn has a higher heating value than the original biomass (Bridgeman, Jones, Shield, & Williams, 2008). In addition, the thermal decomposition has shown to modify the fibrous structure of the biomass and reduces the energy required for grinding or pulverizing, compared to the original biomass (Mani, Tabil, & Sokhansanj, 2004).

1.2.3. Waste as a feedstock

As discussed above, torrefaction has the potential to provide a replacement for coal, however, no commercially operated facilities have been developed in the US. The main reason for this is the high cost of the biomass feedstock and the low price of alternative fuel sources (such as natural gas). The use of wastes or residual materials can help with the deployment of the torrefaction technology since a tipping fee is paid for the handling of these wastes. The energy potential of these wastes can be utilized by the energy and power industry (US-EIA, 2010). Bar-Ziv el al. and others have suggested using wastes as a feedstock in torrefaction (Bar-Ziv, Saveliev, & Chudnovsky, 2012; Yuan, Wang, Kobayashi, Zhao, & Xing, 2015). Mumin et al. suggested wet torrefaction (Mu'min, Prawisudha, Zaini, Aziz, & Pasek, 2017). To use wastes as a fuel, a few issues should be addressed: (i) difficulty in conveying, (ii) inconsistency, (iii) high moisture content, (iv) high content of chlorine, sulfur, nitrogen and other compounds.

The EPA has defined a few solid waste streams as "secondary non-hazardous materials". These materials are suitable for fuel production and combustion under the 40 CFR Part 241 rule (40 C.F.R. § 241, 2011). The secondary non-hazardous materials definition includes (i) biomass and biomass residues, (ii) rail-road ties, (iii) scrap tires, (iv) paper recycling residues that may have a considerable amount of plastic, (v) post-consumer material, and (vi) post-industrial materials. The waste streams used in this work conform to these definitions.

1.3. Technology review

1.3.1. Pyrolysis and torrefaction

Pyrolysis is a thermal degradation process that occurs in the absence of oxygen. It is a promising route for creating a liquid fuel that can be upgraded to transportation fuels or used directly as a fuel. Of specific interest, biomass pyrolysis has been heavily investigated for the generation of bio-oil for upgrading to fuels with a significantly reduced or neutral carbon footprint. Balat et al. divided pyrolysis into three categories: conventional pyrolysis, fast pyrolysis, and flash pyrolysis (Balat, Balat, Kirtay, & Balat, 2009) based upon their reaction temperature, heating rate, solid residence time and particle size. Conventional pyrolysis is generally applied to relatively large particles (5-50mm) because conduction heat transfer limits the heating rates to less than 1 K/s. Fast pyrolysis is typically applied to small particles (<1 mm) for which heating rates of 10-200 K/s can be achieved. The residence time of fast pyrolysis reactions is usually in the range of 0.5-10 s. Flash pyrolysis is typically applied particles that are smaller than 0.2 mm at heating rates >1000 K/s and residence times <0.5 s.

Several recent reviews have presented various production technologies for pyrolysis including ablative (coil, mill, plate, vortex, etc.), circulating fluidized bed, entrained flow, fluidized bed, moving bed (vacuum, transported, stirred, horizontal, etc.), rotary hearth, microwave, and rotating cone (Bridgwater, 2003; Bridgwater, Meier, & Radlein, 1999; Butler, Devlin, Meier, & McDonnell, 2011; Venderbosch & Prins, 2010). Regardless of the technology, however, perhaps the most important factor for the conversion reactor is the heat transfer rate stemming from the reactor itself (reactor wall in

ablative pyrolysis, gas or wall contact in transport bed or entrained flow), or from use of a heat transfer medium (HTM) such as the bed material in a fluidized bed.

According to Briens et al., 2008, and Butler et al., 2011, the current technologies that can be commercially applied for bio-oil production are the bubbling fluidized bed (BFBs) and circulating fluidized beds (CFBs). However, auger reactors also have high market attraction because of their simplicity, robustness, and its long established history as effective conversion reactors (Briens, Piskorz, & Berruti, 2008; Butler et al., 2011). Particularly the Lurgi-Ruhrgas twin-screw mixer has been extensively investigated in the past for thermal treatment (focusing on coal degassing) and has been demonstrated at a capacity of at least 50 ton/day for pyrolysis (Butler et al., 2011; Venderbosch & Prins, 2010). In addition, McGee and Miao recently detailed the application of auger feeders in fast pyrolysis systems and difficulties in the continuous feed of biomass systems (McGee, 2012; Miao, Grift, Hansen, & Ting, 2014). It was found that the characteristics and performance of augers with biomass such as flow, the angle of response, particle mixing, efficiency, volumetric/mass flow, etc. are difficult to predict, do not typically match well-established auger correlations, and must be proven empirically. Because of the technology strength and potential market attractiveness, an auger-based reactor system was developed and is the focus of this work.

Specifically, for thermal treatment of materials, augers have been heavily studied in the disposal and recycling of waste materials, degassing of coals, and gasification. Chun et al. studied the pyrolysis gasification of sewer sludge in a pilot screw reactor (Chun, Kim, & Yoshikawa, 2011). Many studies have been done on the recycling/disposal of automotive waste and shredded tires in pilot conversion units ranging from 100 g/hr to 8

kg/hr (Aylón et al., 2010, 2008; Day, Shen, & Cooney, 1999; Haydary, Susa, Gelinger, & Čacho, 2016; Martinez, Murillo, Garcia, & Veses, 2013), and larger commercial units, such as that studied by Day et al. at 200 kg/hr (Day, Cooney, & Shen, 1996). In a study of the larger unit, Day et al. concluded that although the auger reactor is a good method of resource recovery and waste disposal, and is energetically self-sustaining, further development is required and there is vast room for improvement. Other studies have found similar results from medium density fiberboard scraps and aseptic packaging (Ferreira, Altafini, Perondi, & Godinho, 2015; Haydary, Susa, & Dudas, 2013). Many of these studies were performed using screw augers of approximately 2.0-5.0 cm in diameter and 0.5-2.0 m in length with residence times on the order of several minutes. However, several studies investigating treatment (desulfurization and carbonization e.g.) of coals typically concerned high temperatures and longer residence times due to its recalcitrant nature (Gao et al., 2014; Lin, Khang, & Keener, 1997; Roedig & Klose, 2009). Such experiments ranged from 40 seconds up to 3 hours with waste wood gasification and carbonization of waste wood from fruit orchard trees cuttings (Agirre, Griessacher, Rosler, & Antrekowitsch, 2013; Efika, Wu, & Williams, 2012). The range of studies that have been conducted using auger reactors demonstrates that such systems are robust for a wide variety of materials and processing conditions.

There are three main concepts for heating the biomass in auger-type reactors to produce bio-oils. The first is an increasing pressure gradient via reduction in screw size or pitch (Botten, Burbidge, & Blackburn, 2003; Chen & Pan, 2011); the second is through external heating of the auger or wall (Garcia-Perez, Adams, Goodrum, Geller, & Das, 2007; Ingram et al., 2008; Kelkar et al., 2015; Mohan et al., 2007; Pittman et al., 2012);

and the third (discussed in Chapter (2)) is through combined use of external heat and the addition of an inert heat transfer medium to enhance the heating rate through particle-particle conduction (Aramideh, Xiong, Kong, & Brown, 2015; Brown & Brown, 2012; Henrich, Dahmen, Weirich, Reimert, & Kornmayer, 2016; Sirijanusorn, Sriprateep, & Pattiya, 2013) or through using catalysts directly as heat transfer media to perform in-situ catalytic pyrolysis (Veses et al., 2015, 2014). In the first heating scheme, it was found that 500 °C was the optimum reaction temperature for the production of pyrolysis oils from the woody feedstock, with exception of the smallest particles sizes, with typical oil yield ranging from 50-60% (Botten et al., 2003; Chen & Pan, 2011). Kelkar et al. investigated the fast pyrolysis of spent coffee grounds in a mobile screw conveyor under the second heating scheme (Kelkar et al., 2015), who developed a statistical model with their empirical results for prediction of optimal processing conditions in their 1-6 kg/hr. mobile screw reactor. With the model supported by their empirical work, they identified that the optimal condition (70 RPM of the auger and 505 °C) in the investigated range would yield an approximate 62% liquid product. The idea of using an auger system as a portable method of densifying biomass-based energy through pyrolysis had been previously investigated in similar works (Ingram et al., 2008; Mohan et al., 2007; Pittman et al., 2012), which generally concluded that although such auger systems typically have slower heating rates, they are still a viable solution for production of pyrolysis oils. Other parametric works with similar indirectly heated auger systems support these claims and achieve reasonable yields from auger reactors (Bosong, Wei, Qi, Tiejun, & Longlong, 2014; Dahmen, Henrich, Dinjus, & Weirich, 2012; Garcia-Perez et al., 2007; Liaw et al., 2012; Liaw, Zhou, Wu, & Garcia-Perez, 2013; Morgano, Leibold, Richter, & Seifert, 2015; K Promdee & Vitidsant,

2014; Kittiphop Promdee & Vitidsant, 2013; Puy et al., 2011; R. Zhou, Lei, & Julson, 2013; S. Zhou et al., 2013). Such works have shown that although yields are comparable, it is important to note the liquid composition can be significantly affected by primary and secondary reactions arising from low particle heating rates and vapor-phase residence times.

To increase the heating rate of the biomass particles within auger reactors and to avoid such secondary charring/cracking reactions or long particle/vapor residence times, some development has been done to include a heat transfer medium (HTM). Through this addition, biomass particles are not only heated through contact with the hot reactor wall but mostly through contact with the preheated HTM. Several HTM have been investigated including silica sand and quartz (Henrich et al., 2016; Pfitzer et al., 2016), steel shot (Brown & Brown, 2012; Henrich et al., 2016), and various catalysts (clay minerals such as bentonite and sepiolite, and oxides of alkali metals such as calcium oxide) referenced above. Henrich et al. used a twin-screw auger (40 mm diameter screws, 1.5 m total length) with various heat transfer media to process hardwood, softwood, wheat bran, and straw (Henrich et al., 2016; Pfitzer et al., 2016). Average yields of 66.5%, 69.1%, 60.0%, and 51.4% were achieved for the respective feedstock with feeds of approximately 10 kg/hr raw biomass and 1,150 kg/hr. heat transfer media. Brown and Brown also found that auger type reactors are well suited for bio-oil production, and achieved yields of 73% in a surface response analysis of their 1 kg/hr. twin auger system (25.4 mm diameter screws, 0.56 m total length) with an HTM feed rate of 18 kg/hr. and 63 RPM (Brown & Brown, 2012). They report that the addition of a HTM reduces the solid residence time by more than 95%, and achieves 25% more liquid yield compared to other auger studies that use external

heating (Brown & Brown, 2012). Both studies used short solid residence times (ranging in 5-15 s) to demonstrate that HTM used within twin-screw auger reactors exhibits sufficient heat transfer to perform fast pyrolysis and produce yields comparable to fluid bed reactors. (Cremers et al., 2015; Nhuchhen, Basu, & Acharya, 2014)

For torrefaction, the technology used is similar to pyrolysis technologies described above. These technologies can be divided into two types, direct and indirect heating media. In direct heating reactors, the heating media (flue gasses, heat transfer material (HTM), etc.) is in direct contact with the feedstock. On the other hand, indirect heating application separates the heating media from the biomass by a conductive barrier such as metal walls.

Auger reactor – consist of one or more helix screws (augers) attached to the shaft in the center of a hollow cylinder. The feedstock is flown within the cylinder by the auger mechanism. The hot media is flown in a separate pipe (with a larger diameter) and around (co-centered) the cylinder containing the feedstock. Thus, creating indirect heating of the feedstock. Gasses generated by the reaction are separated from the solid stream at the end of the screw reactor.

Rotary drum reactor – Are adapted from the drying technology. The rotary drum reactor is a long, rotating hollow cylinder placed with a horizontal angle for material flow. As the cylinder rotates the feedstock inside mixes it. The feedstock can be directly heated or indirectly heated. The directly heated reactor utilizes super-heated steam or hot flue gasses from a combustion chamber to create a hot environment. Indirect heating utilizes burners that heat the outer cylinder walls. A few parameters control the torrefaction process: inlet temperature, rotation speed, the length of the reactor and slope angle. This

technology has been used for drying and reaction application and has an established industry.

Multiple Hearth Furnace (MHF) – a well-established technology that allows continuous operation. The MHF is built from round, multi-leveled, platforms. Each platform has its own heating mechanism, steam injection or internal gas burners. As the feedstock enters from the top of the furnace a mechanical mechanism will push the material toward the hole in the center of the platform. As the material falls through the hole, it lands in the center of the lower platform and is pushed toward the gap between the platform and the walls of the MHF. This operation principle can be duplicated as many times as needed for a certain processing level. Heating of each individual platform is done independently allowing better control over the torrefaction temperature. With this technology, drying can be done in the higher platforms followed by torrefaction at the lower platforms.

Microwave reactor – the feedstock is loaded into a chamber with microwave radiation that heats up the feedstock to the desired temperatures and thermochemically treats the biomass. It can provide uniform heating throughout the depth of the feedstock. The relatively large size particle can be efficiently treated.

1.4. Objectives and proposal structure

The objectives of the present study are:

(i) To demonstrate that paddle (auger) reactors can be considered in fast pyrolysis of biomass to obtain bio-oils.

(ii) Show the properties of waste as a potential feedstock for torrefaction.

(iii) Explore the properties of extruded waste (before and after torrefaction).

(iv) To demonstrate the first-of-a-kind combined paddle-extruder reactor for preparation of waste as a fuel.

The first objective is to demonstrate that a singled-shaft paddle reactor can achieve fast pyrolysis and produce bio-oil and char yields that are similar to those of other fast pyrolysis designs. The reactor's auger was modified to enhance the mixing between the feedstock and the HTM. The auger used in this work was designed with cuts in the flighting and mixing paddles within the auger pitches to promote solid mixing and reduce conveying efficiency, resulting in increased heat transfer rate between the feedstock and the HTM.

The second objective is to study the feasibility of utilizing wastes as a feedstock and study the properties of those materials. This was done by characterization of the fiber-plastic mix before and after torrefaction.

The third objective was studying the properties of the fiber-plastic mix (torrefied and untreated) after extrusion.

The last objective is to demonstrate the utilization of waste as a feedstock, is done by developing a first-of-a-kind combined paddle-extruder reactor. This reactor can process waste to produce a high density, consistent material

1.5. References

40 C.F.R. § 241., (2011).

Agirre, I., Griessacher, T., Rosler, G., & Antrekowitsch, J. (2013). Production of charcoal as an alternative reducing agent from agricultural residues using a semi-continuous semi-pilot scale pyrolysis screw reactor. *Fuel Processing Technology*, *106*(July 2016), 114–121. https://doi.org/10.1016/j.fuproc.2012.07.010

Aramideh, S., Xiong, Q., Kong, S. C., & Brown, R. C. (2015). Numerical simulation of biomass fast pyrolysis in an auger reactor. *Fuel*, *156*, 234–242. https://doi.org/10.1016/j.fuel.2015.04.038

Aylón, E., Fernández-Colino, A., Murillo, R., Navarro, M. V., García, T., & Mastral, A. M. (2010). Valorisation of waste tyre by pyrolysis in a moving bed reactor. *Waste Management*, *30*(7), 1220–1224. https://doi.org/10.1016/j.wasman.2009.10.001

Aylón, E., Fernández-Colino, A., Navarro, M. V., Murillor, R., García, T., & Mastral, A. M. (2008). Waste tire pyrolysis: Comparison between fixed bed reactor and moving bed reactor. *Industrial and Engineering Chemistry Research*, *47*(12), 4029–4033. https://doi.org/10.1021/ie071573o

Balat, M., Balat, M., Kirtay, E., & Balat, H. (2009). Main routes for the thermo-conversion of biomass into fuels and chemicals. Part 1: Pyrolysis systems. *Energy Conversion and Management*, *50*(12), 3147–3157. https://doi.org/10.1016/j.enconman.2009.08.014

Bar-Ziv, E., Saveliev, R., & Chudnovsky, B. (2012). Torrefied-Biomass (biocoal) from Municipal Solid Waste for Power productionied-Biomass. *International Conference on Waste Technology*, p25. https://doi.org/101208841

Bosong, L., Wei, L., Qi, Z., Tiejun, W., & Longlong, M. (2014). Pyrolysis and catalytic upgrading of pine wood in a combination of auger reactor and fixed bed. *Fuel*, *129*, 61–67. https://doi.org/10.1016/j.fuel.2014.03.043

Botten, A. J., Burbidge, A. S., & Blackburn, S. (2003). A model to predict the pressure development in single screw extrusion. *Journal of Materials Processing Technology*, *135*(2-3 SPEC.), 284–290. https://doi.org/10.1016/S0924-0136(02)00859-2

Bridgeman, T. G., Jones, J. M., Shield, I., & Williams, P. T. (2008). Torrefaction of reed canary grass, wheat straw and willow to enhance solid fuel qualities and combustion properties. *Fuel*. https://doi.org/10.1016/j.fuel.2007.05.041

Bridgwater, A. V. (2003). Renewable fuels and chemicals by thermal processing of biomass. *Chemical Engineering Journal*, *91*(2–3), 87–102. https://doi.org/10.1016/S1385-8947(02)00142-0

Bridgwater, A. V., Meier, D., & Radlein, D. (1999). An overview of fast pyrolysis of biomass. *Org. Geochem.*, *30*(12), 1479–1493. https://doi.org/10.1016/S0146-6380(99)00120-5

Briens, C., Piskorz, J., & Berruti, F. (2008). Biomass Valorization for Fuel and Chemicals

Production -- A Review. *International Journal of Chemical Reactor Engineering*, *6*(1). https://doi.org/10.2202/1542-6580.1674

Brooks, A. L., Wang, S., & Jambeck, J. R. (2018). The Chinese import ban and its impact on global plastic waste trade. *Science Advances*. https://doi.org/10.1126/sciadv.aat0131

Broström, M., Nordin, A., Pommer, L., Branca, C., & Di Blasi, C. (2012). Influence of torrefaction on the devolatilization and oxidation kinetics of wood. *Journal of Analytical and Applied Pyrolysis*. https://doi.org/10.1016/j.jaap.2012.03.011

Brown, J. N., & Brown, R. C. (2012). Process optimization of an auger pyrolyzer with heat carrier using response surface methodology. *Bioresource Technology*, *103*(1), 405–414. https://doi.org/10.1016/j.biortech.2011.09.117

Butler, E., Devlin, G., Meier, D., & McDonnell, K. (2011). A review of recent laboratory research and commercial developments in fast pyrolysis and upgrading. *Renewable and Sustainable Energy Reviews*, *15*(8), 4171–4186. https://doi.org/10.1016/j.rser.2011.07.035

Chen, Y. C., & Pan, Y. N. (2011). Effects of Grain Size and Rotational Speed on the Bio-Oil Yield in a Fast Pyrolysis Reactor Employing a Single Tapered Screw Extruder. *Advanced Materials Research*, *347–353*, 153–156. https://doi.org/10.4028/www.scientific.net/AMR.347-353.153

Chew, J. J., & Doshi, V. (2011). Recent advances in biomass pretreatment - Torrefaction fundamentals and technology. *Renewable and Sustainable Energy Reviews*. https://doi.org/10.1016/j.rser.2011.09.017

Chun, Y. N., Kim, S. C., & Yoshikawa, K. (2011). Pyrolysis gasification of dried sewage sludge in a combined screw and rotary kiln gasifier. *Applied Energy*, *88*(4), 1105–1112. https://doi.org/10.1016/j.apenergy.2010.10.038

Cremers, M., Koppejan, J., Middelkamp, J., Witkamp, J., Sokhansanj, S., Melin, S., & Madrali, S. (2015). Status overview of torrefaction technologies: A review of the commercialisation status of biomass torrefaction (2015). ISBN 978-1-910154-23-6. In *IEA Bioenergy*.

Dahmen, N., Henrich, E., Dinjus, E., & Weirich, F. (2012). The bioliq® bioslurry gasification process for the production of biosynfuels, organic chemicals, and energy. *Energy, Sustainability and Society*, *2*(1), 1–44. https://doi.org/10.1186/2192-0567-2-3

Day, M., Cooney, J. D., & Shen, Z. (1996). Pyrolysis of automobile shredder residue: An analysis of the products of a commercial screw kiln process. *Journal of Analytical and Applied Pyrolysis*, *37*(1), 49–67. https://doi.org/10.1016/0165-2370(96)00938-2

Day, M., Shen, Z., & Cooney, J. D. (1999). Rapid #: -10789723. *Journal of Analytical and Applied Pyrolysis*, *51*(1), 181–200.

Efika, C. E., Wu, C., & Williams, P. T. (2012). Syngas production from pyrolysis-catalytic steam reforming of waste biomass in a continuous screw kiln reactor. *Journal of*

Analytical and Applied Pyrolysis, *95*, 87–94. https://doi.org/10.1016/j.jaap.2012.01.010

US-EPA. (2015). Carbon Pollution Emission Guidelines for Existing Stationary Sources: Electric Utility Generating Units; Final Rule. In *Federal register* (Vol. 80). Retrieved from https://www.gpo.gov/fdsys/pkg/FR-2015-10-23/pdf/2015-22842.pdf

Ferreira, S. D., Altafini, C. R., Perondi, D., & Godinho, M. (2015). Pyrolysis of Medium Density Fiberboard (MDF) wastes in a screw reactor. *Energy Conversion and Management*, *92*, 223–233. https://doi.org/10.1016/j.enconman.2014.12.032

Gao, H. J., Zhu, Y. Z., Chen, H. J., Liao, C. H., Du, Y., & Wu, H. (2014). Pyrolysis of Hailar Lignite: Experiments with a Tubular Reactor and a Continuous Screw Kiln Reactor. *Applied Mechanics and Materials*, *672–674*, 665–671. https://doi.org/10.4028/www.scientific.net/AMM.672-674.665

Garcia-Perez, M., Adams, T. T., Goodrum, J. W., Geller, D., & Das, K. C. (2007). Production and fuel properties of pine chip bio-oil/biodiesel blends. *Energy and Fuels*, *21*(4), 2363–2372. https://doi.org/10.1021/ef060533e

Haydary, J., Susa, D., & Dudas, J. (2013). Pyrolysis of aseptic packages (tetrapak) in a laboratory screw type reactor and secondary thermal/catalytic tar decomposition. *Waste Management*, *33*(5), 1136–1141. https://doi.org/10.1016/j.wasman.2013.01.031

Haydary, J., Susa, D., Gelinger, V., & Čacho, F. (2016). Pyrolysis of automobile shredder residue in a laboratory scale screw type reactor. *Journal of Environmental Chemical Engineering*, *4*(1), 965–972. https://doi.org/10.1016/j.jece.2015.12.038

Henrich, E., Dahmen, N., Weirich, F., Reimert, R., & Kornmayer, C. (2016). Fast pyrolysis of lignocellulosics in a twin screw mixer reactor. *Fuel Processing Technology*, *143*, 151–161. https://doi.org/10.1016/j.fuproc.2015.11.003

Ingram, L., Mohan, D., Bricka, M., Steele, P., Strobel, D., Mitchell, B., … Pittman, C. U. (2008). *Pyrolysis of Wood and Bark in an Auger Reactor : Physical Properties and Chemical Analysis of the Produced Bio-oils Pyrolysis of Wood and Bark in an Auger Reactor : Physical Properties and Chemical Analysis of the Produced Bio-oils*. (15), 614–625. https://doi.org/10.1021/ef700335k

Kelkar, S., Saffron, C. M., Chai, L., Bovee, J., Stuecken, T. R., Garedew, M., … Kriegel, R. M. (2015). Pyrolysis of spent coffee grounds using a screw-conveyor reactor. *Fuel Processing Technology*, *137*(July 2016), 170–178. https://doi.org/10.1016/j.fuproc.2015.04.006

Liaw, S. S., Wang, Z., Ndegwa, P., Frear, C., Ha, S., Li, C.-Z., & Garcia-Perez, M. (2012). *Effect of pyrolysis temperature on the yield and properties of bio-oil obtained from the auger pyrolysis of Douglas Fir Wood*. *93*, 52–62.

Liaw, S. S., Zhou, S., Wu, H., & Garcia-Perez, M. (2013). Effect of pretreatment temperature on the yield and properties of bio-oils obtained from the auger pyrolysis of Douglas fir wood. *Fuel*, *103*, 672–682. https://doi.org/10.1016/j.fuel.2012.08.016

Lin, L., Khang, S. J., & Keener, T. C. (1997). Coal desulfurization by mild pyrolysis in a dual-auger coal feeder. *Fuel Processing Technology*, *53*(1), 15–29. https://doi.org/10.1080/15435070701583110

Mani, S., Tabil, L. G., & Sokhansanj, S. (2004). Grinding performance and physical properties of wheat and barley straws, corn stover and switchgrass. *Biomass and Bioenergy*. https://doi.org/10.1016/j.biombioe.2004.03.007

Martinez, J. D., Murillo, R., Garcia, T., & Veses, A. (2013). Demonstration of the waste tire pyrolysis process on pilot scale in a continuous auger reactor. *Journal of Hazardous Materials*, *261*, 637–645. https://doi.org/10.1016/j.jhazmat.2013.07.077

McGee, E. (2012). Continuous Combustion: Plug Screw Feeder Technology for Biomass Pyrolysis System. *Bulk Solids Handling*, *32*(2), 44–46.

Miao, Z., Grift, T. E., Hansen, A. C., & Ting, K. C. (2014). Flow performance of ground biomass in a commercial auger. *Powder Technology*, *267*, 354–361. https://doi.org/10.1016/j.powtec.2014.07.038

Mohan, D., Pittman, C. U., Bricka, M., Smith, F., Yancey, B., Mohammad, J., … Gong, H. (2007). Sorption of arsenic, cadmium, and lead by chars produced from fast pyrolysis of wood and bark during bio-oil production. *Journal of Colloid and Interface Science*, *310*(1), 57–73. https://doi.org/10.1016/j.jcis.2007.01.020

Mohan, D., Pittman, C. U., & Steele, P. H. (2006). Pyrolysis of Wood / Biomass for Bio-oil : A Critical Review. *Energy & Fuesl*, *20*(4), 848–889. https://doi.org/10.1021/ef0502397

Morgano, M. T., Leibold, H., Richter, F., & Seifert, H. (2015). Screw pyrolysis with integrated sequential hot gas filtration. *Journal of Analytical and Applied Pyrolysis*, *113*, 216–224.

Mu'min, G. F., Prawisudha, P., Zaini, I. N., Aziz, M., & Pasek, A. D. (2017). Municipal solid waste processing and separation employing wet torrefaction for alternative fuel production and aluminum reclamation. *Waste Management*. https://doi.org/10.1016/j.wasman.2017.05.022

Nhuchhen, D., Basu, P., & Acharya, B. (2014). A Comprehensive Review on Biomass Torrefaction. *International Journal of Renewable Energy & Biofuels*. https://doi.org/10.5171/2014.506376

Pfitzer, C., Dahmen, N., Troeger, N., Weirich, F., Sauer, J., Günther, A., & Müller-Hagedorn, M. (2016). FAST PYROLYSIS OF WHEAT STRAW IN THE BIOLIQ® PILOT PLANT. *Energy & Fuels*, *30*(10), 8047–8054. https://doi.org/10.1021/acs.energyfuels.6b01412

Pittman, C. U., Mohan, D., Eseyin, A., Li, Q., Ingram, L., Hassan, E. B. M., … Steele, P. H. (2012). Characterization of bio-oils produced from fast pyrolysis of corn stalks in an auger reactor. *Energy and Fuels*, *26*(6), 3816–3825. https://doi.org/10.1021/ef3003922

Promdee, K, & Vitidsant, T. (2014). *Applied Thermal Pyrolysis of Cogongrass in Twin*

Screw Reactor 1. *61*(8), 612–617. https://doi.org/10.1134/S0040601514080102

Promdee, Kittiphop, & Vitidsant, T. (2013). Synthesis of char, bio-oil and gases using a screw feeder pyrolysis reactor. *Coke and Chemistry*, *56*(12), 466–469. https://doi.org/10.3103/S1068364X13120107

Puy, N., Murillo, R., Navarro, M. V., López, J. M., Rieradevall, J., Fowler, G., … Mastral, A. M. (2011). Valorisation of forestry waste by pyrolysis in an auger reactor. *Waste Management*, *31*(6), 1339–1349. https://doi.org/10.1016/j.wasman.2011.01.020

Roedig, M.-K., & Klose, W. (2009). Modelling of coal pyrolysis using a twin screw reactor. *Revue de Metallurgie*, *106*(10), 404–409.

Shankar Tumuluru, J., Sokhansanj, S., Hess, J. R., Wright, C. T., & Boardman, R. D. (2011). REVIEW: A review on biomass torrefaction process and product properties for energy applications. *Industrial Biotechnology*. https://doi.org/10.1089/ind.2011.7.384

Sirijanusorn, S., Sriprateep, K., & Pattiya, A. (2013). Pyrolysis of cassava rhizome in a counter-rotating twin screw reactor unit. *Bioresource Technology*, *139*, 343–348. https://doi.org/10.1016/j.biortech.2013.04.024

US-EIA. (2010). Total MSW generation Per capita generation. Retrieved from https://archive.epa.gov/epawaste/nonhaz/municipal/web/pdf/msw_2010_rev_factsheet.pdf

US-EPA. (2018). *Advancing Sustainable Materials Management: 2015 Fact Sheet Assessing Trends in Material Generation, Recycling, Composting, Combustion with Energy Recovery and Landfilling in the United States*.

Venderbosch, R., & Prins, W. (2010). Fast pyrolysis technology development. *Biofuels, Bioproducts and Biorefining*, *4*(2), 178–208. https://doi.org/10.1002/bbb.205

Veses, A., Aznar, M., López, J. M., Callén, M. S., Murillo, R., & García, T. (2015). Production of upgraded bio-oils by biomass catalytic pyrolysis in an auger reactor using low cost materials. *Fuel*, *141*, 17–22. https://doi.org/10.1016/j.fuel.2014.10.044

Veses, A., Aznar, M., Martinez, I., Martinez, J. D., Lopez, J. M., Navarro, M. V., … Garcia, T. (2014). Catalytic pyrolysis of wood biomass in an auger reactor using calcium-based catalysts. *Bioresource Technology*, *162*, 250–258. https://doi.org/10.1016/j.biortech.2014.03.146

World Bank. (2018). What a Waste 2.0. *World Bank*. https://doi.org/10.1596/978-1-4648-1329-0

Yuan, H., Wang, Y., Kobayashi, N., Zhao, D., & Xing, S. (2015). Study of Fuel Properties of Torrefied Municipal Solid Waste. *Energy and Fuels*. https://doi.org/10.1021/ef502277u

Zhou, R., Lei, H., & Julson, J. (2013). The effects of pyrolytic conditions on microwave pyrolysis of prairie cordgrass and kinetics. *Journal of Analytical and Applied Pyrolysis*, *101*, 172–176. https://doi.org/10.1016/j.jaap.2013.01.013

Zhou, S., Mourant, D., Lievens, C., Wang, Y., Li, C. Z., & Garcia-Perez, M. (2013). Effect of sulfuric acid concentration on the yield and properties of the bio-oils obtained from the auger and fast pyrolysis of Douglas Fir. *Fuel*, *104*, 536–546. https://doi.org/10.1016/j.fuel.2012.06.010

2. Fast pyrolysis with mixing paddle reactor

2.1. Summary

We have developed a pyrolysis reactor based on a unique auger-paddle configuration with heat transfer material (HTM) and proved to achieve high heating rates and fast pyrolysis. We tested ten different biomass types and obtained bio-oil yields ranging from approximately 40% for thermally treated wood, to approximately 57% for crop residues (corn stover) and 67% yield for woody feedstocks (tulip poplar). These results, as well as the solid char yields, are similar to those obtained for the same feedstock using a circulating fluidized bed. Tests conducted without HTM resulted in lower bio-oil yields (ranging from 8 to 18% decrease in yield) and higher char yields with similar changes in magnitude, which is indicative of slow pyrolysis. In addition, a comprehensive study and analysis of the material residence time and mixing characteristics of the novel auger-paddle system is presented. These results demonstrate that an auger-paddle configuration is capable of achieving the high heating rates required for fast pyrolysis.

2.2. Mixing paddle reactor system

The fast pyrolysis system consists of four main parts: (1) the HTM dosing system (2) the biomass dosing system (3) the heating zone for the HTM (4) fast pyrolysis reactor zone similar to the HTM heater. The current system is semi-continuous and is shown schematically in , but is easily adaptable to continuous operation; the cartoon in the figure is not-drawn-to-scale. The solid stream bio-char exit the system into a sealed container (not drawn). The gas stream (condensable – bio-oil – and non-condensable) flows through a

heated transfer line and through an effective condenser that collects the liquid produced into a sealed tank (not drawn). The cold non-condensable gasses are flown through a cold-water bath to capture remaining bio-oil that was not captured by the condenser (not drawn). The system is kept inert with a sweep stream of nitrogen. The nitrogen flow rate is adjusted so that the time of the gasses in the transfer line will not exceed 2 s.

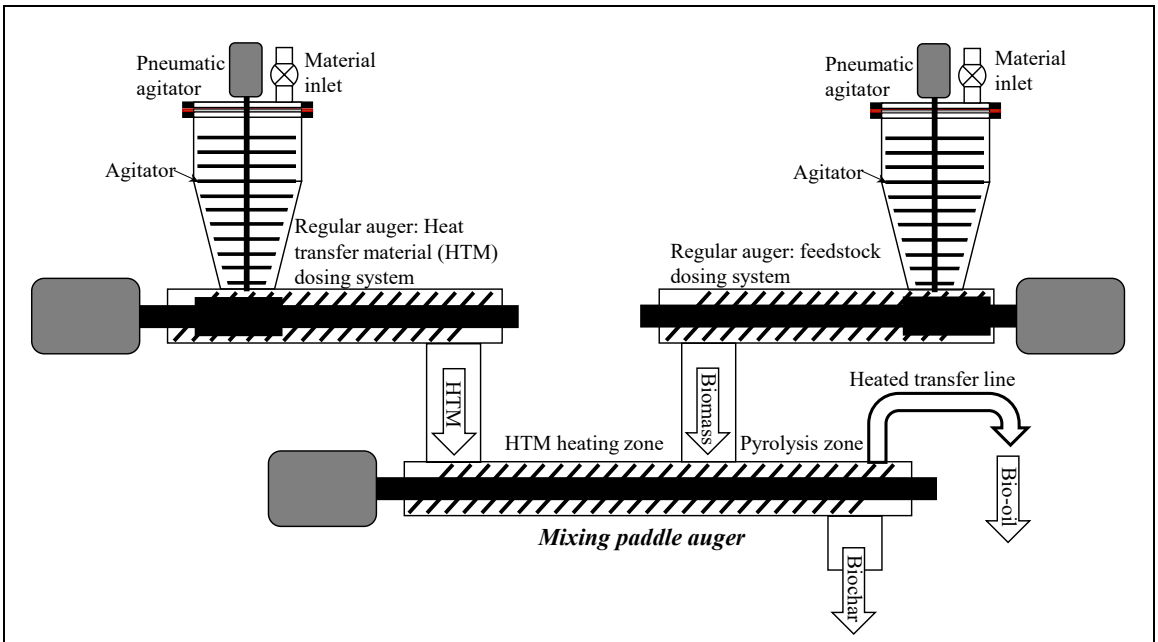

Figure 2.1. Process schematic showing major inlet/outlet streams from the pyrolysis reactor.

An important aspect of any similar system is the consistent and continuous flow of both HMT and feedstock. The HTM feed system consisted of a bin that flood-feeds a standard 2.54 cm diameter regular screw auger flight with a pitch of 2.54 cm. A pneumatic agitator was placed inside the feed bin to avoid bridging. This agitation was essential for the smooth and continuous operation of the system as it ensures rather constant mass flow rates. The agitator has operated a frequency with a duty cycle of 50-100%. A similar agitation configuration was used for the feedstock as well with the same duty cycle. This agitation mechanism avoided bridging and ensure the consistent and continuous flow of

the HTM and feedstock. The shaft of the dosing augers reduces in diameter from the flood fed bin area to the main delivery shaft to allow for a flood fed mouth and avoid material plugging (depicted in Figure 1). The shaft has a diameter of approximately 1.6 cm under the feed bin that decreases to 1.27 cm after the material feed bin. The feed bin can accommodate approximately 3.5 L of material and is sealed after material charging. The feed rate is controlled with a motor equipped with a variable frequency drive. The shaft has packing gland seals with graphite packing on both ends of the auger housing to prevent air from entering the system. The biomass is metered into the system in an identical manner. The pyrolysis reactor acts to (i) a heat the HTM, (ii) mix the HTM with biomass, and (iii) ensure fast biomass pyrolysis.

Heating of the mixing paddle reactor was accomplished by 12, 25.4-mm-wide heating bands (Watlow, MB1E1AN2-E12) of 250 W each with attached thermocouples that are inserted into the reactor and touching the moving material without touching the auger paddles. Figure 2.2 shows a cartoon of the heating control configuration. Each thermocouple measures the material temperature at the respective location and controls the operation of the respective heating band. A programmable logical controller (PLC) monitors all temperatures and uses a proportional-integral-derivative (PID) controller to operate the heating bands independently. Both temperature and heating duty-cycles are recorded continuously to interpret heating rates of the material.

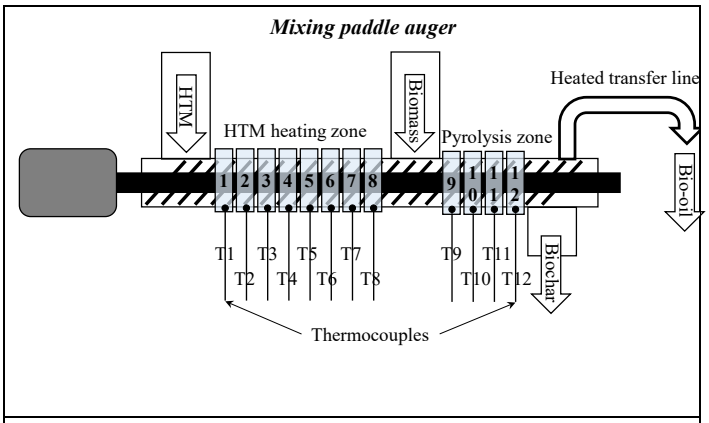

Figure 2.2. Heating of the mixing paddle reactor.

The mixing auger that serves both as a heater for the HTM and pyrolysis of the feedstock is comprised of two mixing elements: (1) cuts in the auger flighting and (2) mixing paddles within each flight pitch. These features are known to enhance mixing rather significantly. These features were selected due to the necessity of superior mixing required for fast pyrolysis that is not attainable in conventional single auger configurations. The diameter of the mixing auger is 2.54 cm with a pitch of 5.08 cm and a shaft of 1.27 cm. The flighting cuts consist of five equal segments of approximate length and spacing of 36 degrees each. Approximately 40% of the flighting area within the 36 degrees of the flight is cut away and leads to material effectively not being conveyed forward and being mixed with the incoming materials from the previous pitch. Four paddles were also placed within each pitch to push the material both sideways and forward, and also lift and retain the solids. The paddles, then, act as an internal mixing device within each pitch and are placed at 45 degrees to the shaft. The paddles are of similar dimensions to the flighting cuts but extend from auger shaft to the same diameter as the normal flighting and four paddles are spaced evenly within each pitch. Features of the reactor configuration are shown in Figure 2.3. Cut flightings and paddles slow down significantly the conveyance of the particles and

enhance solids mixing. The mixing auger extends through the HTM pre-heat zone and the pyrolysis zone. Both sections were heated externally through 250 W band heaters placed down the length of the system (approximately 45 cm length). Each band heater was also paired with a thermocouple that was placed next to the heater and through the housing of the auger, such that the thermocouple was exposed to flowing solid material.

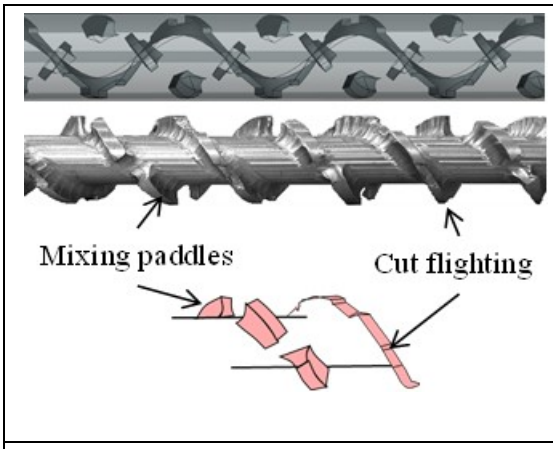

Figure 2.3. Top: 3-D model cutaway showing the mixing features of the auger reactor. Middle - a photograph of the actual paddle reactor. Bottom: details of the cut flighting and paddles.

The pyrolysis gasses and vapors are carried with high purity nitrogen sweep gas to a single pass shell-and-tube condenser with three condensing tubes. The jacket of the condenser is chilled with cold water with ice maintained at approximately 0 °C. Pyrolysis gasses and uncondensed vapors are then bubbled through an ice water bath maintained at approximately 0 °C to capture additional volatile organics before being vented. Oils from the exchanger were collected in standard plastic bottles and stored at approximately 0 °C away from light sources. The solids fall under gravity into a sealed collection bin after the pyrolysis zone. The char collector is not insulated and remains at a relatively low

temperature (<200 °C) compared to the reactor, ensuring that the material does not continue to react.

2.3. Reactor flow analysis

2.3.1. Mass flow rate

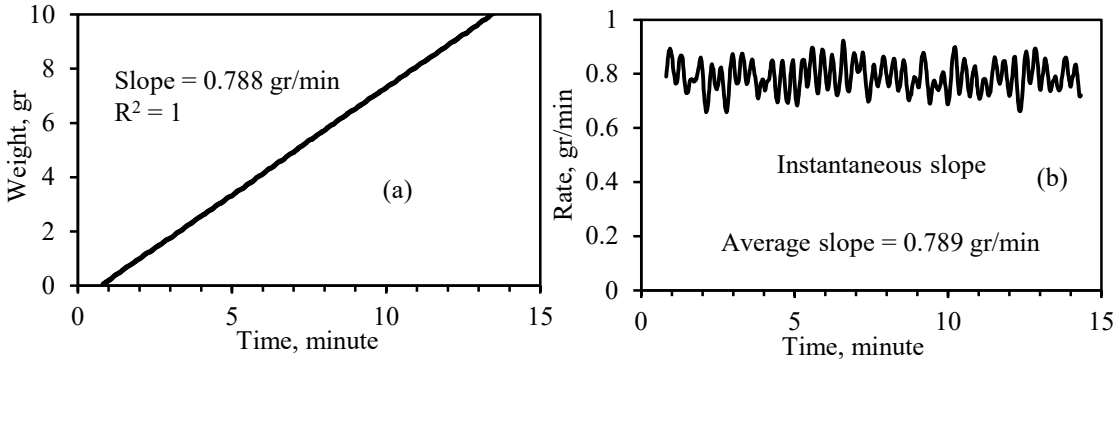

Figure 2.4. Typical weight transients of biomass (a) and instantaneous calculated rates (b).

Mass flow calibration tests were performed with the HTM and biomass materials to determine the rotation frequency required in the dosing feeders to deliver the required mass flows. In these experiments, the material was flown from the respective feed bins by the dosing auger, at a certain shaft rotation and weighed continuously by a scale. The material weight was monitored continuously by the PLC. Mass flow rates were readily available by the automatic derivative of the weight transients. Figure 2.4a shows typical weight transients of biomass as a function of time as measured by the weighing system with a data acquisition rate of 10 Hz. The data is presented without averaging, yielding a slope of 0.788 g/min with an $R^2 = 1$. Figure 2.4b is an instantaneous slope calculated at time intervals of 20 seconds; showing an average slope of 0.789 gr/min. The periodical

behavior of the instantaneous rate is inherent in auger operation due to the pitch structure of an auger and is responsible for a majority of the rate fluctuation.

Calibration of the two dosing systems was done by selecting a feedstock and measuring the feed rates as described above as functions of the auger shaft rotation frequency. Figure 2.5a shows mass flow rates for the HTM-sand; with results fitted to a straight line with a slope of 412 $g.h^{-1}$/rpm. Figure 2.5b shows mass flow rates for blended sawdust; with results fitted to a straight line with a slope of 41.7 $g.h^{-1}$/rpm. Because the mass flow rate depends on material density, each biomass type at the specific particle size distribution should be calibrated. The high quality of data shown in Figure 2.5 also indicates that one can obtain an accurate desired mass flow rate by the respective shaft rotation frequency.

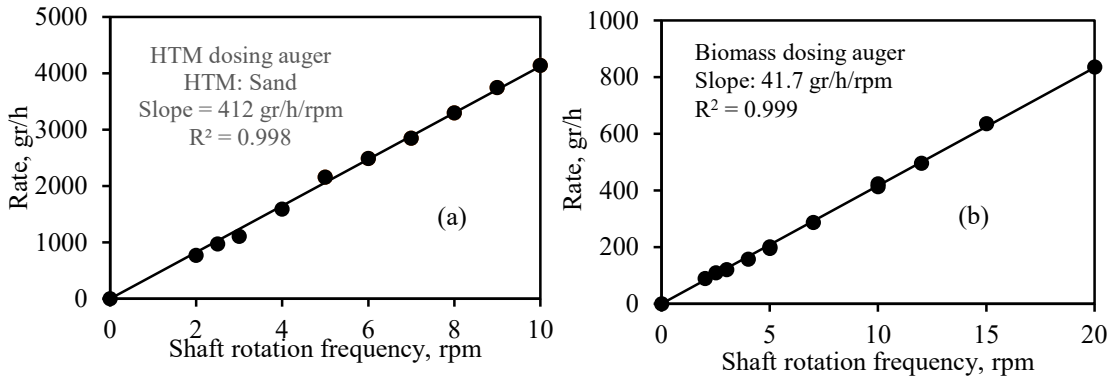

Figure 2.5. Calibration of the HTM - silica sand - dosing system (a) and the biomass dosing system for mixed hardwood sawdust (b).

2.3.2. Residence time evaluation

Figure 2.6 shows the respective rotation frequencies and the residence times for each component. The system has four characteristic residence times: t_{HTM}, t_{bio}, which are the residence times for the HTM and biomass augers, respectively, and t_{heat}, and t_{pyr}, which are the residence times in the heating and pyrolysis zones, respectively. The sum of later

two is the residence time in the reactor, or $t_{reactor} = t_{heat} + t_{pyr}$. The system also has three rotation frequencies as variables: υ_{HTM} and υ_{bio} are the frequency of the HTM and biomass dosing augers respectively; and $\upsilon_{reactor}$, which is the rotation frequency of the reactor. The figure also shows the balance that measures the weight coming out of the reactor outlet.

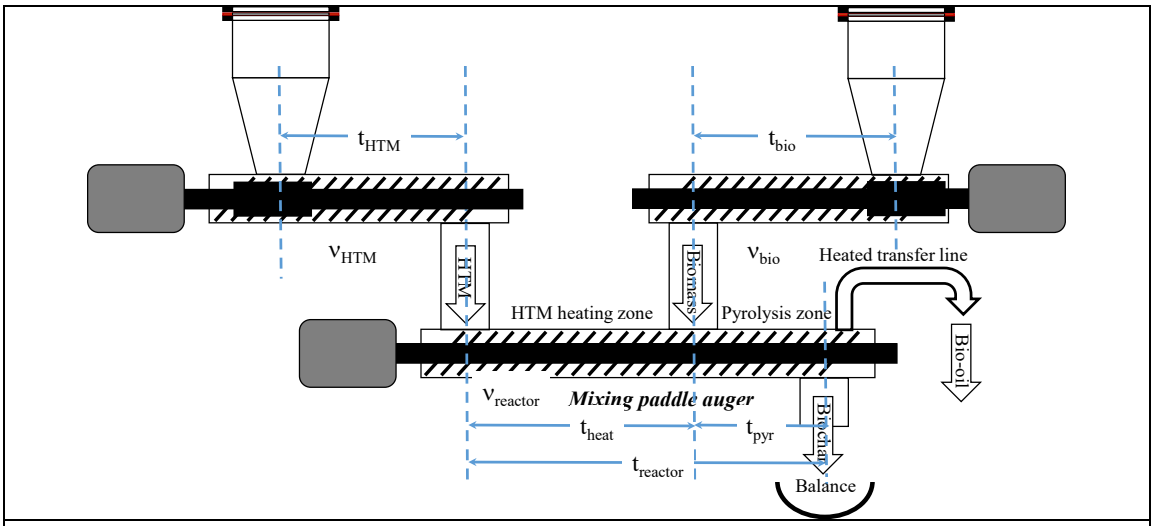

Figure 2.6. Residence time in each part of the system.

The residence time in a regular screw is given by Eq. (2.1)

$$t_{residence} = \frac{c}{\upsilon} \tag{2.1}$$

where υ and c are the rotation frequency and the number of pitches in the auger. Numerous experiments were done with the two dosing augers (HTM and biomass).

Figure 2.7 shows typical results of weight measurements of biomass where the dosing auger is started at time 0, until the biomass reached the balance, from which t_{HTM} and t_{bio} (referred to as t_{tot}), as well as the mass flow rate, were determined for each run. To calculate c, we plotted t_{HTM} (and t_{bio}) vs. $1/\upsilon$ at a constant reactor frequency with typical results shown in Figure 2.8, from which c_{HTM} and c_{bio} were determined to equal 5.72 pitches for both augers.

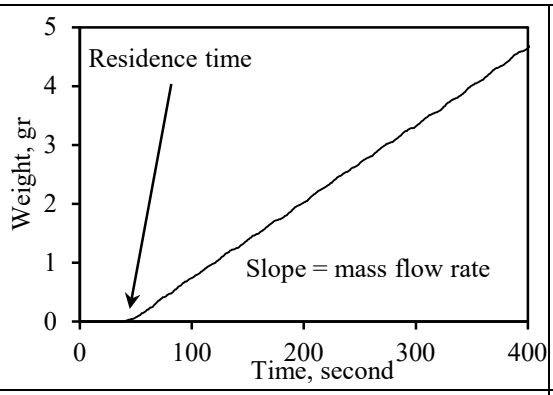

Figure 2.7. Biomass weight transients for determining t_{tot}.

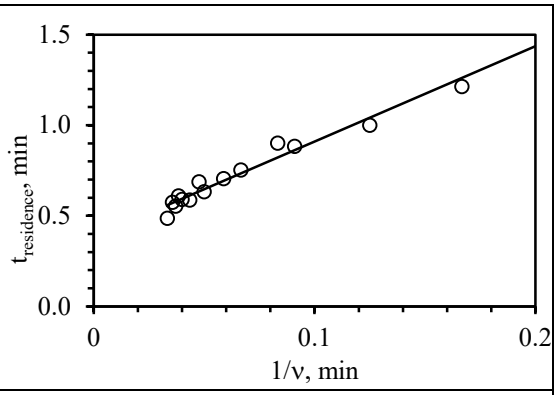

Figure 2.8. t_{tot} from biomass feed to reactor outlet vs. inverse biomass dosing frequency.

The mixing paddle reactor, however, is not a screw auger and has a rather complex structure, and therefore Eq. (2.1) is not valid for the description of the residence time behavior with the rotation of the reactor shaft. A correlation was determined to find the relationship between the residence time and the rotation frequencies. Material in this reactor is moved in a complex way; there are three components in the particle movement, one that pushes the material forward by the movement of the flightings and axial component of the paddles, another that pushes the particles backward by the cuts in the flightings, and the third push the particles sideways by the radial component of the paddles. In fact, the residence time in the reactor should depend on two main factors: (i) the percent filling in the reactor, which in turns depends linearly on the rotation frequency of the dosing auger; and (ii) the rotation frequency of the reactor.

The reactor has two characteristic residence times−one that relates to the entire reactor, $t_{reactor}$ (see Figure 2.6) and another that relates to the pyrolysis time, t_{pyr} (see Figure 2.6). The heating time is $t_{heat} = t_{reactor} - t_{pyr}$ (see Figure 2.6). Let us assume an empirical correlation for the dependence of each of the residence times on the respective dosing auger

rotation frequency (in other words the percent filling of the reactor) and the rotation frequency of the reactor, analogous to that of Eq. (2.1) by Eq. (2.2):

$$t_{reactor} = \frac{c_{eff}(\nu_{reactor}, \nu_{HTM})}{\nu_{reactor}} \tag{2.2}$$

where $c_{eff}(\nu_{reactor}, \nu_{HTM})$ is an analogous number of pitches of the reactor that depends on the HTM and frequency respective frequencies. The parameter $c_{eff}(\nu_{reactor}, \nu_{HTM})$ can also be called the effective number of pitches of the reactor. Let us further assume that the reactor effective number of pitches is given by Eq. (2.3)

$$c_{eff}(\nu_{reactor}, \nu_{HTM}) = a\nu_{HTM}^{m}\nu_{reactor}^{n} \tag{2.3}$$

where *a* is a constant, and n and m are powers. Introducing Eq. (2.3) into (2.2) yields Eq. (2.4)

$$t_{reactor} = a_{reactor}\nu_{HTM}^{m}\nu_{reactor}^{n-1} \tag{2.4}$$

Eq. (2.4) has three parameters, *m*, *n*, and *a*, which can be determined experimentally by measuring $t_{reactor}$ at various reactor and HTM frequencies and carrying out a non-linear regression fitting procedure. To determine these parameters the following experiment was conducted: (i) the HTM was filled than it was stopped; (ii) the reactor auger was turned on continuously; (iii) the HTM auger and balance (see Figure 2.6) were turned on simultaneous. The balance measured weight continuously and both the residence time and mass flow rate were determined as shown in Figure 2.7. The rotation frequency of the HTM auger was changed in the range 6-18 rpm and reactor frequency was varied in the range 20-200 rpm. Figure 2.9 shows the measured residence time results in the reactor, $t_{reactor}$, vs. the calculated time by Eq. (2.4) for best-fit values which were a=9.68, m=0.25, and n=-

0.50; these values are also shown in the figure. Thus, the effective number of pitches in the entire reactor equals (where c_{eff} is dimensionless) is given by Eq. (2.5)

$$c_{reactor}(\nu_{reactor}, \nu_{HTM}) = 9.68\nu_{HTM}^{-0.25}\nu_{reactor}^{0.5} \quad (2.5)$$

The effective number of pitches of the reactor $c_{eff}(\nu_{reactor}, \nu_{HTM})$ was calculated from Eq. (2.3) and typical results are shown in Table 1; as expected, the effective number of pitches depends on both frequencies, however, they are varied in the range 33-88 pitches (depending on the rotation frequencies of the HTM auger and the reactor. In fact, the effective number of pitches shed light on the mixing quality, and hence the heat transfer rate. Clearly, the higher the effective number of pitches the better the mixing and the higher the heating rate.

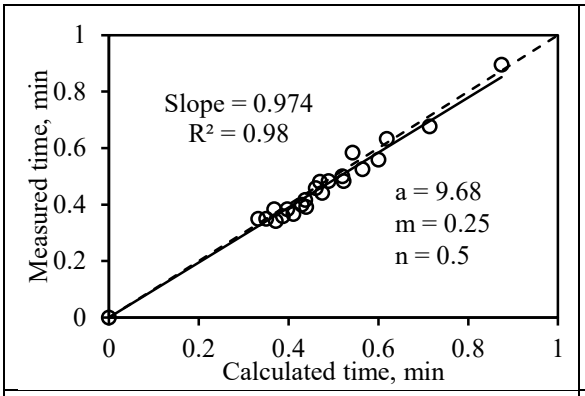

Figure 2.9. Measured $t_{reactor}$ vs. calculated time by Eq. (2.5).

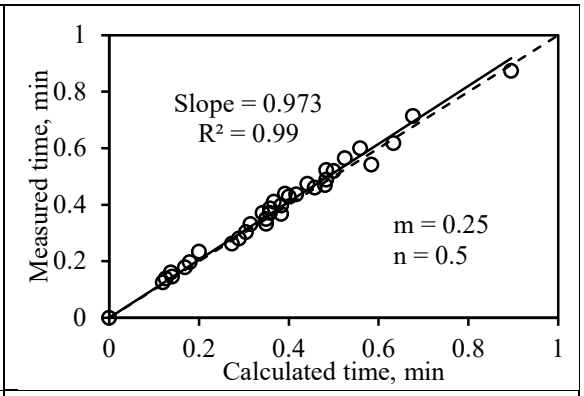

Figure 2.10. Measured residence time in the entire reactor and pyrolysis zone vs. calculated time.

One can define a new parameter that perhaps can be used to determine the mixing quality, and the heating rate, as:

$$p = \frac{c_{eff}(\nu_{reactor}, \nu_{HTM})}{c_{design}} \quad (2.6)$$

or by introducing Eq. (2.3) into (2.5) yields

$$p = \frac{a v_{HTM}^{m} v_{reactor}^{n-1}}{c_{design}} \tag{2.7}$$

where c_{design} is the number of pitches of the designed configuration

Table 2.1. The effective number of pitches (c), and the pitch number (p, in parenthesis) in the reactor at various frequencies of the HTM and reactor.

	Effective number of pitches		
Reactor, rpm	HTM @6 rpm	HTM @12 rpm	HTM @18 rpm
50	43.7 (4.9)	36.8 (4.1)	33.2 (3.7)
100	61.8 (6.9)	52.0 (5.8)	47.0 (5.2)
150	75.8 (8.4)	63.7 (7.1)	57.6 (6.4)
200	87.5 (9.7)	73.6 (8.2)	66.5 (7.4)

The parameter p in Eq. (2.6), will be referred to as the pitch number, can probably serve as a measure of the quality of mixing because higher p values indicate better mixing. The values of c_{design} are in this particular system is 9 pitches; p was calculated by Eq. (2.6) and results are summarized in Table 2.1.

The value of p varies in the range 3.7-9.7, which indicate a significant increase in the mixing propensity. The value of p also indicates a ratio of the equivalent axial length (and thus equivalent time) solid particles would spend in a traditional screw reactor at the same RPM. A value greater than one suggests that the design footprint of the reactor can be significantly reduced, while simultaneously enhancing the time solid particles mix and comingle. The results presented here suggest that given a constrained residence time (such as that required for pyrolysis), the size of a reactor can be reduced by up to an order of magnitude at high RPM (material throughput) compared to traditional screws. In addition to this effectively enhanced residence time, the reactor paddles ensure that particles retained in each pitch are thoroughly mixed.

The same analysis was conducted for the pyrolysis zone with the similar power terms, however with a different scalar, thus the effective number of pitches in the pyrolysis zone was found to be as presented in Eq. (2.8)

$$c_{py}(\nu_{reactor}, \nu_{HTM}) = 3.67\nu_{bio}^{-0.25}\nu_{reactor}^{0.5} \quad (2.8)$$

The residence time data for the entire reactor and the pyrolysis zone were plotted in Figure 2.10 to show a perfect fit for a straight line with a slope of almost unity.

The ratio between the two effective numbers (of pitches) is Eq. (2.5) divided by Eq. (2.8) to yield 2.63. On the other hand, this ratio should be close to the ratio of the length of the entire reactor to the length of the pyrolysis zone, which is 3, very close to the determined ratio. This is a strong indication that the flow of material within the reactor reached orderly and steady flow at a much shorter distance than the reactor length. In other words, the residence time within the reactor is linear with the reactor axial coordinate.

2.4. Thermal characteristics

2.4.1. Reactor thermal dynamics

To demonstrate that this reactor configuration can indeed perform fast pyrolysis, it is essential to understand the thermal characteristics of the system. As indicated above, the heating zone was kept at a set point of 550 ºC (T1-T8 in Figure 2.2), while the pyrolysis zone was maintained at 500 ºC (T9-T12 in Figure 2.2). Table 2.2 shows: (i) the setpoints (second column) at the two zones; (ii) the temperature after heating was turned on and system reached steady-state (third column), showing a stable temperature mostly around $\pm$0.1 ºC and negligible difference from the set points except in a few points; (iii) the temperatures after flowing the HTM and reaching a second steady-state, showing

negligible changes in the temperatures (this is of course attributed to the fact that were sufficient heating capacity by the heating bands to account for all required heat); (iv) after feeding the biomass and reaching a third thermal steady-state again showing very negligible changes in the temperatures in all zones.

Table 2.2. Temperature setpoints and stabilized temperatures at various stages of operation.

	Set-point(°C)	Empty System (°C)	With HTM (°C)	HTM and Feed(°C)
T1	550	550.0±0.1	550.4±1.0	550.2±0.9
T2	550	558.4±0.1	557.3±0.5	556.5±0.4
T3	550	550.0±0.1	550.4±0.3	550.0±0.1
T4	550	550.0±0.2	550.3±0.4	549.9±0.2
T5	550	550.0±0.3	550.3±0.6	550.0±0.2
T6	550	558.0±0.1	555.0±0.5	558.3±0.1
T7	550	573.5±0.1	562.0±0.4	575.6±0.1
T8	550	550.0±0.1	550.3±0.4	549.9±1.4
T9	500	500.0±0.1	514.6±0.5	500.0±1.6
T10	500	500.0±0.1	500.4±0.3	500.2±0.5
T11	500	498.6±0.1	494.2±0.2	496.5±0.3
T12	500	500.0±0.1	500.2±0.1	500.1±0.1

Figure 2.11 is a graphical portrayal of the temperature of thermocouples 1-8 (top) and duty-cycle of heaters 1-8 (bottom) in the preheating zone. We note the following: (i) A start-up period, starting at t=0, where only the metal is being heated with no material flowing, thermal steady-state was achieved after about (both temperatures and duty cycles) was stabilized about 1.50 hours. (ii) We kept the system stable for about 1.2 hours which is indicated by very stable temperatures and duty cycles in all zones. (iii) At t ~ 2.6 hr. HTM was flown which in noted the sudden drop in temperatures of T1 and immediate increase of duty-cycle of heater 1. Other zones were affected, but not as much. This means

that the first heater had sufficient heat capability to increase the temperature of all HTM almost instantly. (iv) After about 20 minutes the system reached again thermal steady-state, noticed by constant temperatures and duty cycles of all heaters. (v) At t ~ 3.4 hr. biomass was flown with very small changes both in temperatures and duty cycles. (vi) After about 40 minutes, the system reached again thermal steady-state, noted by no change in temperatures and duty cycles.

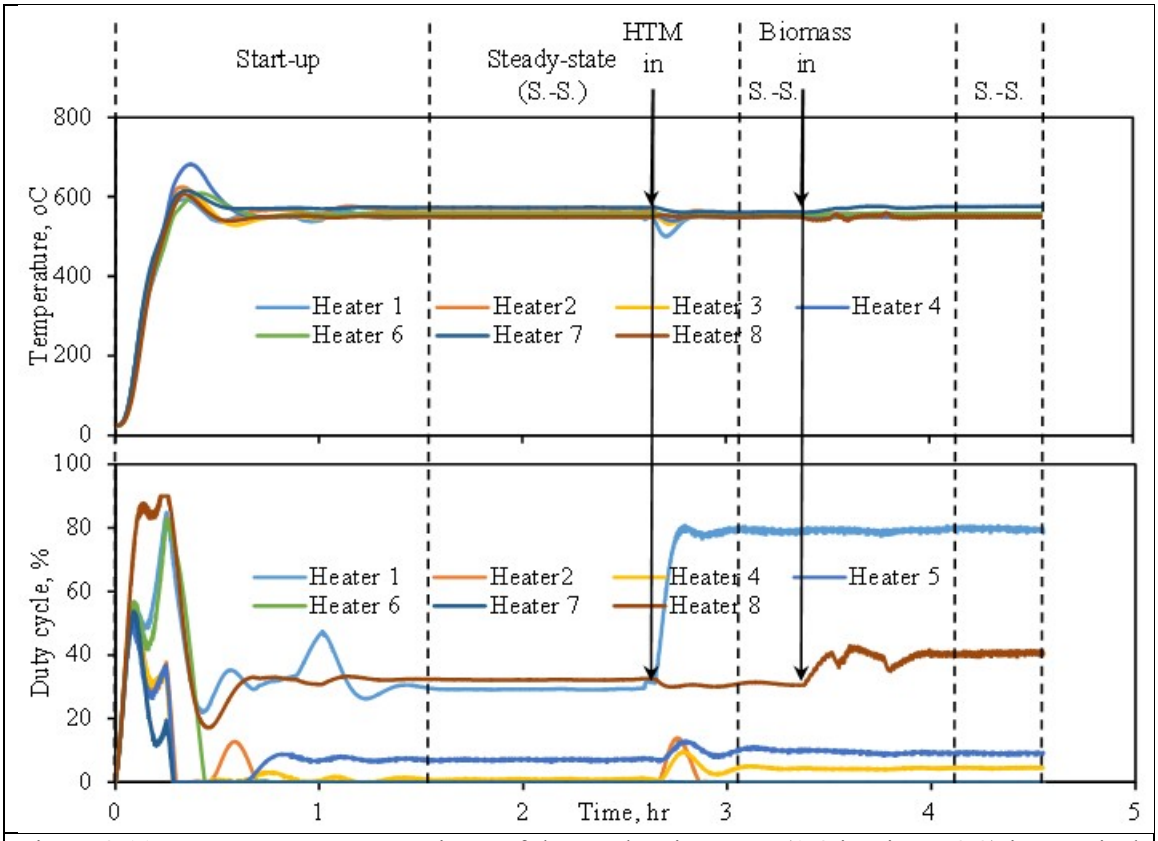

Figure 2.11. Top: temperature transients of the pre-heating zone (1-8 in Figure 2.2) in a typical run were all heaters were controlled according to temperature setpoints listed in Table 2. Bottom: duty-cycles of heaters 1-8.

Figure 2.12 is a graphical portrayal of the temperature of thermocouples 9-12 (top) and duty-cycle of heaters 9-12 (bottom) in the pyrolysis zone. The behavior here follows that in the preheat zone, except that the changes are very small: At t ~ 2.6 hr. HTM was

flown which is noted by a very small drop in temperatures of T9 and very small changes in duty-cycle of heaters; at t ~ 3.4 hr. biomass was flown with very small changes both in temperatures and duty cycles.

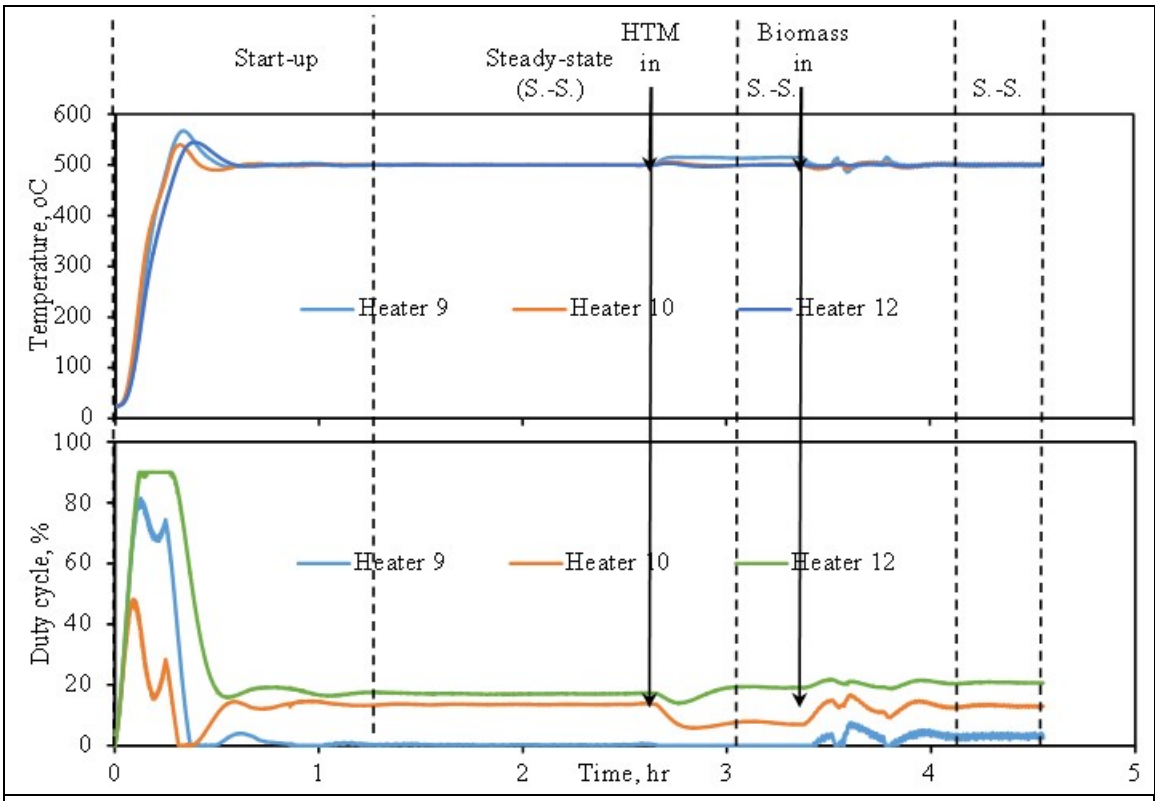

Figure 2.12. Top: temperature transients of the pyrolysis zone (9-12 in Figure 2.2) in a typical run were all heaters were controlled according to temperature setpoints listed in Table 2.2. Bottom: duty-cycles of heaters 9-12.

One can gain insight into the heating rate between the HTM and the biomass by studying the behavior of the duty cycle for each heater. In fact, what is important in examining the duty cycles of each heater, is not the absolute value of the duty cycle, but the difference between the final steady-state when both HTM, as well as biomass, are flown, and the initial steady-state for each heater without material. Heat losses from the reactor to the surroundings vary significantly in different regions of the reactor; the heaters compensate for these heat losses by operating in different duty cycle according to the need

to keep constant temperatures in the various regions in the reactor. Once the temperature profiles reached steady-state, the heat losses depend only on the temperature differences between the reactor and surroundings. Therefore, the difference between the final steady-state value of the duty cycle in each heater and its initial steady-state value depends only on the requirement to heat the material in the specific location. We have plotted in Figure 2.13 typical results for this difference vs. the location of the heater. The difference in duty cycle in heater 1 is significant because this is where the HTM s heated from its original ambient temperature to the required 550 ^{o}C (we note that material at this location did indeed reach this temperature as shown in Figure 2.11 and Table 2.2). Heaters 2-7 display negligible difference (within the scatter of the duty cycle results), that can be considered zero. This means that the first heater was mostly responsible for heating the HTM. To help follow the results an exponential decay was fit. The difference in the duty-cycle of Heater 8 increases to about 8% and that of 9 increased by about 3%. Here too to help follow the results, a Gaussian function was fit; not surprisingly the peak appears exactly where the biomass is flown into the pyrolysis part. Table 2.3 summarizes average results for duty cycles for Heaters 9 and 10 with their respective standard deviations and the difference in the duty cycles; while the difference in duty cycles for heater 9 is ~ 3.1$\pm$0.6%. Heaters 10-12 display zero duty cycle difference. The important implication of these interesting results is the heating rate of the biomass. The fact that the increase in the duty cycle differences in Heaters 8 and 9 are very small is not surprising because the HTM is already hot and should require little heat (if at all) to increase the temperature of the biomass from ambient to 500 ^{o}C. What is important to indicate, is that from the width of the Gaussian distribution one can estimate the width of the heating region for the biomass to be approximately 12.25 mm

(0.5 pitch). This can be roughly translated into time (see detailed residence time analysis above) into less than 1 s required to heat the biomass from ambient temperature to 500 ˚C, which is the required heating time for fast pyrolysis.

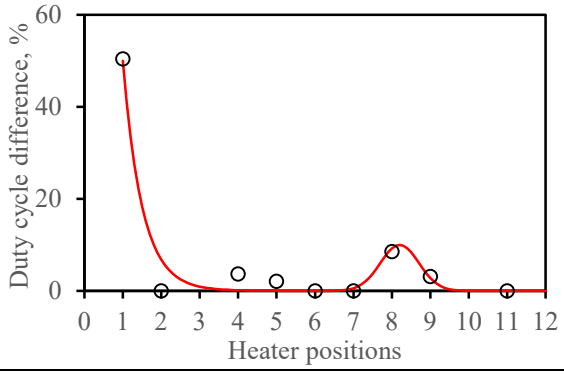

Figure 2.13. Difference between final and initial duty-cycles for each heater (after reaching steady-state operation.

Table 2.3. Duty cycle difference between the final state to the initial state for Heaters 8 and 9.

	Duty-cycle	
Status	Heater 9 (%)	Heater 10 (%)
Before material flow	0.25 + 0.10	13.5 + 0.1
After material flow	3.32 + 0.47	13.2 + 0.2
Difference	3.07 + 0.57	-0.3 + 0.3

2.4.2. Determination of heat capacity

The specific heat capacity is an essential property that must be known for any heat energy balance calculations. Often this property is not known for the feedstock used in fast pyrolysis. Heat capacity depends strongly on moisture content and other variables that are not constant. This implies that a method for measuring heat capacity should be developed within the reactor in use. Further, the temperature dependence of specific heat capacity is an important factor to consider, hence must be measured as well.

In this study, a method has been developed for measuring the specific heat capacity of any feedstock. We demonstrated this method for biomass and silica sand over a large range of mass flow rates and temperature.

The heat rate required to increase the material temperature from T_o to T_2, at thermal steady-state, is presented by Eq. (2.9)

$$\dot{q}_{tot}(\dot{m}, T) = \dot{m} \int_{T_o}^{T_2} c_p(T) dT \tag{2.9}$$

where $\dot{q}_{tot}$ is the total heat required to heat the material, that is contributed by all heating elements (See Figure 2.2), $\dot{m}$ is mass flow rate of the material and c_p is specific heat capacity. If we assume a very common dependence of c_p on T as $c_p = c\sqrt{T}$, then Eq. (2.9 becomes Eq. (2.10)

$$\dot{q}_{tot}(\dot{m}, T) = \dot{m}c \frac{2\left(T_2^{3/2} - T_o^{3/2}\right)}{3} \tag{2.10}$$

The dependence of the specific heat capacity on temperature can be determined by varying the mass flow rates and temperature and plotting $\dot{q}_{tot}$ vs. $\dot{m} \frac{2\left(T_2^{3/2} - T_o^{3/2}\right)}{3}$ and determining the value of c through a curve-fitting procedure.

To determine the value of c the following experiments were carried out:

(i) The reactor shaft was set at a specific rotation frequency in the range 10-200 rpm.

(ii) The reactor was purged with nitrogen at a flow rate in the region 0.1-0.25 L/min.

(iii) The reactor walls were heated (till reaching thermal steady-state) either uniformly or at two temperatures along the axial coordinate. The initial

temperature was ambient (20°C) and final temperature varied in the range 50-500°C for sand and 50-350°C for biomass (to prevent pyrolysis).

(iv) The duty cycles at steady state of all heaters with nitrogen were recorded and average power for each heater was determined. The sum of powers of all heaters is the heat rate required to increase the nitrogen temperature from T_o to T_2 and all heat losses. By varying the nitrogen flow rate one can obtain the rate of heat losses (as it they are not affected by the flow rate).

(v) A specific feedstock was flown into the reactor (either sawdust or sand) at a given flow rate in the range 10-1500 g/hr for biomass and 1000-6000 g/hr for sand. The sum of powers of all heaters is the heat rate required to increase the temperature of nitrogen and material from T_o to T_2 and all heat losses. The net heat rate required just for the material is obtained by subtracting the respective values for nitrogen heating and heat losses as explained in (iv).

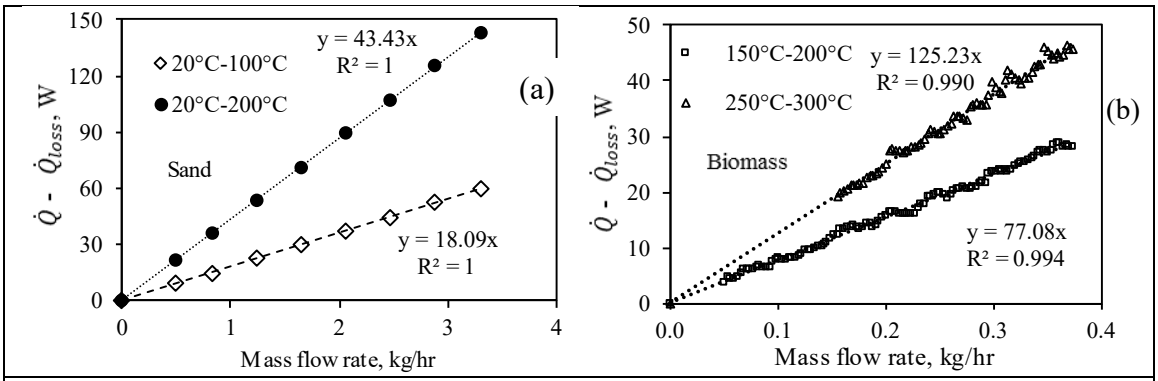

Figure 2.14. Net heat rate (subtracted by the rate heat losses) required to heat sand (a) and biomass (b) from ambient.

Figure 2.14 (a) and (b) some examples are shown for the dependence of the net heat rate (without losses) on mass flow rate for both sand and biomass respectively at two different temperature ranges. Linear behavior of the heat rate with mass flow rate for both

materials is observed. In Figure 2.14 (a), two experiments are shown, when all heaters were set to 100°C and to 200°C and the material was heated from 20°C to 100°C and from 20°C to 200°C, respectively. In Figure 2.14 (b), heaters 1-5 were set to 150°C and heaters 6-12 were set to 200°C and the net heat rate from 20°C to 200°C was determined (as explained above). Similarly, for the case 250°C-300°C case, heaters 1-5 were set to 250°C and heaters 6-12 were set to 300°C. In both cases, the summation of heat rates of all heaters was recorded and plotted vs. mass flow rate.

A correlation for the specific heat capacity of sand is present by Eq. (2.11)

$$c_p(T) = 44.4\sqrt{T} \tag{2.11}$$

and for biomass (sawdust) presented by Eq. (2.12)

$$c_p(T) = 78.8\sqrt{T} \tag{2.12}$$

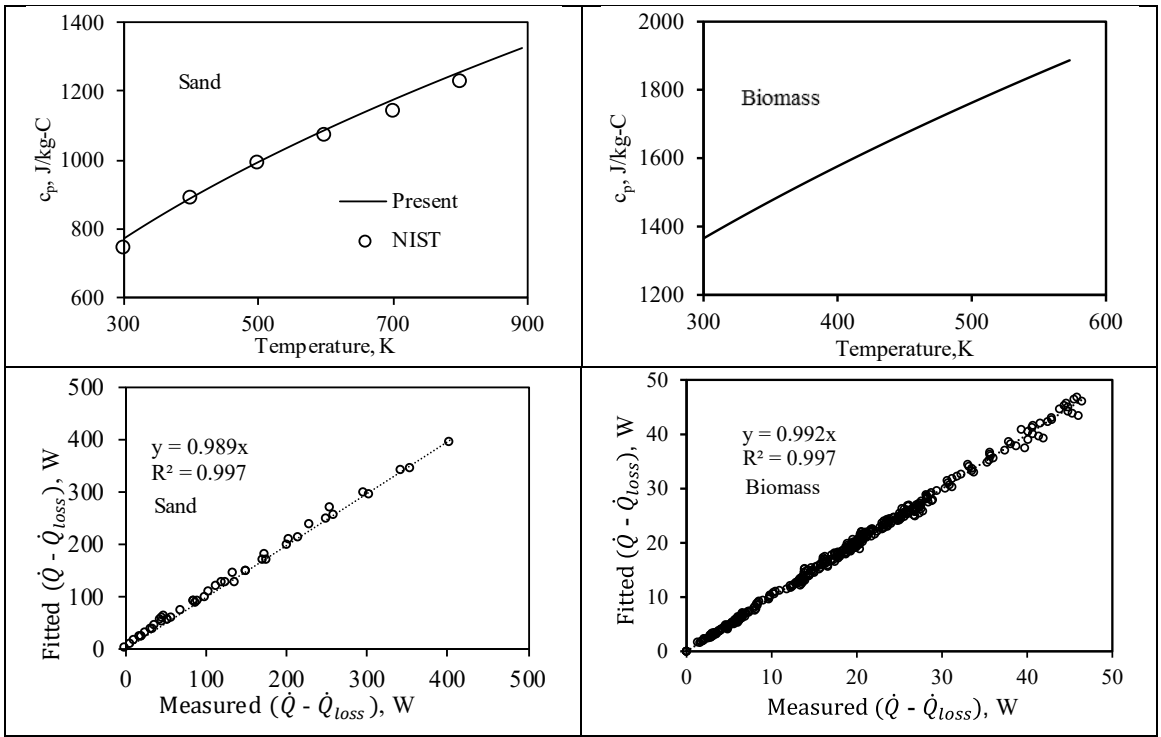

Figure 2.15. Top: Specific heat capacity for sand (left) and for biomass (right). Bottom: Heat rate fitted (by eq. 2) vs. measured heat rate for sand (left, with c=44.4 J/kg-K$^{3/2}$) and for biomass (right, with c=78.8 J/kg-K$^{3/2}$).

Figure 2.15-Top shows the variation of specific heat capacity with temperature for sand (left) and biomass (right). It is observed that the experimentally determined c_p for sand is in excellent agreement with the data for quartz from NIST. Biomass c_p values from the literature typically range from 1300-2000 J/kg-K. Our predicted values are within the range observed in other published works.

Substituting Eq. (2.11) and (2.12) in Eq. (2.9) the heat rate calculated and plotted vs. the measured total heat rate in Figure 2.15-Bottom for sand (left) and biomass (right). It is seen that there is a very good agreement in the results between measured and fitted values. This is an indication of the accuracy of measurement for determining the specific heat. These correlations for specific heat are used in the subsequent sections of thermal analysis.

2.5. Fast pyrolysis feedstock conversion with HTM

2.5.1. Feedstock

In this work, we show the reactor configuration and parameters that determine residence time and mixing (heat transfer) rates. Results for ten biomass feedstocks that were tested within the mixing auger reactor system are presented to evaluate conversion performance and pyrolysis characteristics. The feedstocks include switchgrass, corn stover, hybrid poplar, clean loblolly pine, construction and demolition wood residues (C&D waste), thermally treated loblolly pine, miscanthus, tulip poplar, piñion juniper, and a blended feedstock consisting of clean loblolly pine, tulip poplar, and switchgrass. These feedstocks were ground using a knife mill equipped with a 2-mm screen (Thomas Wiley Laboratory Mill Model 4, 1 hp; Thomas Scientific, NJ) and then tested in a pilot-scale

reactor described above, and compared to results obtained from a circulating fluidized bed reactor. In chapters (3)-(5) we will discuss the use of wastes as a feedstock for torrefaction and pyrolysis applications.

2.5.2. Experimental procedure

During the experimental trials, the system was brought to an initial thermal steady state prior to flowing the HTM, where the HTM preheat zone with all eight heating bands (heaters 1-8 in Figure 2.2) were controlled to a setpoint of 550 °C. The pyrolysis reactor zone, with all four heating bands (heaters 9-12 in Figure 2.2) was controlled to a set point of 500 °C. The idea was that because of the large ratio between the HTM and biomass, this 50 ºC difference will suffice for heating the biomass instantly thus creating fast heating rates and consequent fast pyrolysis. The vapor transfer line to the condenser was controlled to 400-425 ºC during all trials to prevent condensation of liquid product. After the system reached the respective stable temperatures (approximately 30 minutes), the flow of HTM (sand) was fed at a continuous 1,500 g/hr. This caused the initial heaters to deviate from their set points until the PID controllers could accommodate the temperature drop and increase the duty cycle on the affected band heaters and re-approach a steady-state (approximately 15 minutes). After this steady state was reached, the biomass was fed at a continuous rate of approximately 100 g/hr. A high flow of HTM relative to the biomass was used to ensure sufficient heat was available within the mixing solids, and provide a mechanism for fast heat transfer. It is likely that the amount of HTM could be significantly reduced through optimization of temperatures and flow rates, but was not investigated in this proof-of-concept study. Approximately 400 grams of biomass was tested for each trial.

Duplicate and triplicate trials were performed on select feedstock to understand repeatability, it was found that liquid product yield varied by less than 2% demonstrating very good experimental repeatability. To accommodate the material and provide sufficient mixing, the reactor auger was maintained at a rotation frequency of 50 RPM. Throughout the experiment, high purity nitrogen was passed through the system at a rate of at least 0.24 standard liters per minute. The system temperature profiles and other characteristics are described below in the Results and Discussion section below.

After concluding the experiment and allowing the system to cool to <50°C, the unit was opened for cleaning and product recovery. Between each trial, the material feed hoppers were completely emptied of material and weighed to factor into the mass balance. The system was also opened and cleaned at the various drop tubes, transfer lines, seals, etc. for the collection of fugitive materials to refined the trial's mass balance. Typical values for collected unreacted solids were less than one percent. The solids collector was weighed before and after each trial in addition to the solids recovered from the collector. Small amounts of char and HTM (<1% of the combined masses) were also collected and considered from the tube connecting the solid collector to the reactor. The total liquid yield was comprised of the sum of the oil collected in the condenser bottle (>85% liquid mass), the difference in weight of the water bubbler/scrubber before and after a trial (~8% liquid mass), and oil residues remaining on the condenser tubes and transfer line.

2.5.3. Comparison with NREL results

As mentioned above, the main objective of the present work is to demonstrate the applicability of our proposed reactor system to fast pyrolysis. We selected to compare our

pyrolysis results with those of NREL's 50.8 mm fluidized bed reactor (2FBR) using the same biomass feedstocks (Howe et al., 2013; Carpenter et al., 2016). The comparison was made only for the measured char and bio-oil yields. Pyrolysis of the ten-tested biomass feedstock was carried out with the following conditions: 2.5-3 RPM for HTM yielding approximately 1,500 g/hr, and 3-4 RPM of biomass yielding approximately 100g/hr flow of biomass. The reactor was maintained at 50 RPM for all trials. The target conversion temperature for all feedstocks was 500°C. This is a ratio of 15 mass unit of sand to 1 mass unit of biomass. These values are consistent with those used by (Brown & Brown, 2012) (18:1) and by (Henrich, Dahmen, Weirich, Reimert, & Kornmayer, 2016), and (Pfitzer et al., 2016) (11:1). We selected a ratio of 15:1 because this corresponded to a particle ratio of 5:1 under the studied sand and biomass sizes. Figure 2.16 displays char and bio-oil yields plotted vs. NREL's results for the same materials (Westover et al. 2013; Howe et al. 2015; Carpenter et al., 2016). The yield of char and liquid (char yield %, liquid yield %) for switchgrass, corn stover, clean pine, thermally treated pine, blend (clean pine, tulip poplar, switchgrass), pinion-juniper, tulip poplar, hybrid poplar, C&D waste, and miscanthus were (19.7,64.8), (8.6, 56.8), (10.8, 64.6), (33.2, 39.6), (13.2, 58.5), (12.1, 66.0), (8.5, 66.7), (7.6, 61.6), (11.3, 59.6), and (11.4, 58.1) respectively. The species with the highest liquid yield was tulip poplar (66.7%), while the lowest yield was obtained from the thermally treated pine (39.6%), followed by corn stover (56.8%). The highest char production was observed from the thermally treated pine (33.2%) followed by switchgrass (19.7%), while the lowest char was observed from hybrid poplar (7.6%) The solid line in the plot represents a perfect fit (slope of 1). The dashed line is the best linear regression fit of the results with a slope of also 1 and an intercept of 0.02, indicating an excellent fit between our results

and those of NREL's for the same materials. We also carried out the same pyrolysis runs without HTM. Figure 2.17 displays char and bio-oil yield results for the same materials as in Figure 2.16 plotted vs. NREL's results, without the flow of HTM. The solid line has a slope of 1, and the dashed line is the best linear regression fit of the results with a slope of also 0.64, indicating that the pyrolysis performed without HTM does not produce yields equal to those produced by fast pyrolysis. The pyrolysis liquid yield obtained without the use of HTM ranged from 8 to 18% lower than the respective tests with an HTM. In other words, under the current design and operation mode, HTM is an essential requirement for the high heating rate that is needed to maximize bio-oil yields.

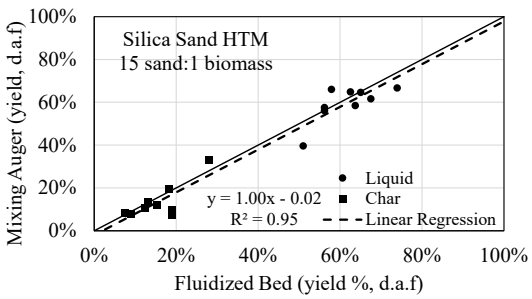

Figure 2.16. Plot of char and bio-oil yields vs. those of NREL for the same materials. The ratio between HTM and biomass was 15:1.

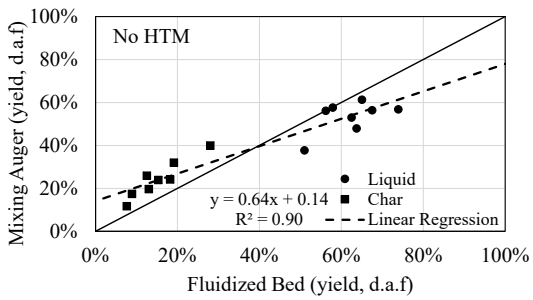

Figure 2.17. Plot of char and bio-oil yields vs. those of NREL for the same materials of Figure 2.16, without HTM.

2.5.4. Heat transfer analysis

Heat transfer analysis plays an important role in designing a thermochemical process. Understanding the heat transfer can explain the results from the pyrolysis experiment (Figure 2.16., and Figure 2.17). According to Di Blasi et al., there is little effect on the final liquid yield distribution of fast pyrolysis products, if the heating rate is greater than 15 °C/s (Di Blasi, 1996). In the work of Ullal, a method of modeling the heat transfer rate was developed (Ullal, 2017). As can be seen by the temperature and heating rate

transient presented in Figure 2.18(a) and Figure 2.18(b) the instantaneous heating rate can reach up to 530 °C/s. This high heating rate explains the similarities of the experimental results of the liquid and char yields (as compared with NREL Fluidized Bed yields, Figure 2.16).

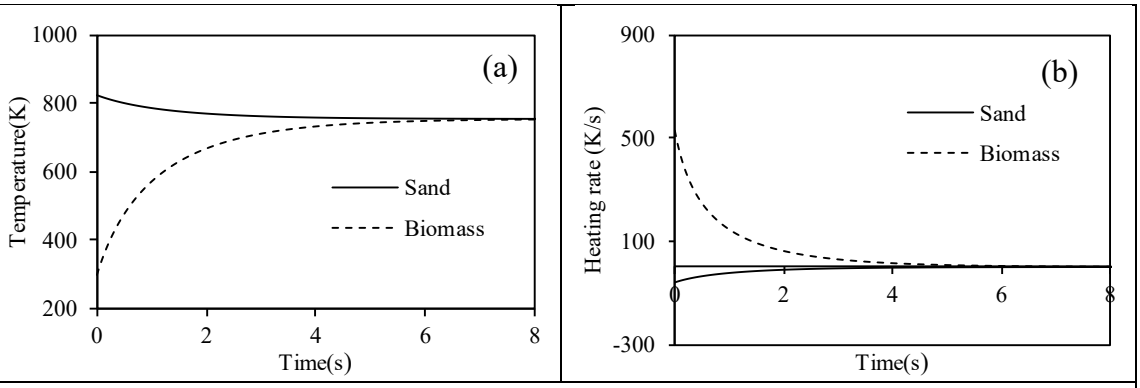

Figure 2.18 – Temperature transient (a) and heating rate (b) of fast pyrolysis of biomass (sawdust) with sand as HTM. (Ullal, 2017).

2.6. Conclusions

We have developed a pyrolysis reactor system that is based on mechanical conveying using a unique auger-paddle configuration with HTM as an essential part for achieving high mixing rates and as a consequence high heating rate. This, in turn, enables fast biomass pyrolysis. In this study the focus was on the proof of concept and the characterization of residence times and heating rates. Residence times were measured in the reactor and a correlation was developed for the residence time and reactor shaft frequency. Further, we have conducted a comprehensive thermal characterization of the system and showed that heating rates are approximately 530 °C/s which is significantly faster than those required for fast pyrolysis. We tested ten different biomass types and obtained char and bio-oil yields similar to those obtained by NREL using a circulating

fluidized bed with the same feedstocks. Thus, our system with the current operation mode has high heating rates that enable fast pyrolysis.

2.7. References

Brown, J. N., & Brown, R. C. (2012). Process optimization of an auger pyrolyzer with heat carrier using response surface methodology. *Bioresource Technology*, *103*(1), 405–414. https://doi.org/10.1016/j.biortech.2011.09.117

Di Blasi, C. (1996). Kinetic and Heat Transfer Control in the Slow and Flash Pyrolysis of Solids. *Industrial and Engineering Chemistry Research*, *35*(1), 37–46. https://doi.org/10.1021/ie950243d

Henrich, E., Dahmen, N., Weirich, F., Reimert, R., & Kornmayer, C. (2016). Fast pyrolysis of lignocellulosics in a twin screw mixer reactor. *Fuel Processing Technology*, *143*, 151–161. https://doi.org/10.1016/j.fuproc.2015.11.003

Howe, D., Westover, T., Carpenter, D., Santosa, D., Emerson, R., Deutch, S., … Lukins, C. (2015). Field-to-fuel performance testing of lignocellulosic feedstocks: An integrated study of the fast pyrolysis-hydrotreating pathway. *Energy and Fuels*. https://doi.org/10.1021/acs.energyfuels.5b00304

Pfitzer, C., Dahmen, N., Troeger, N., Weirich, F., Sauer, J., Günther, A., & Müller-Hagedorn, M. (2016). FAST PYROLYSIS OF WHEAT STRAW IN THE BIOLIQ® PILOT PLANT. *Energy & Fuels*, *30*(10), 8047–8054. https://doi.org/10.1021/acs.energyfuels.6b01412

Ullal, A. (2017). HEAT TRANSFER ANALYSIS IN A PADDLE REACTOR FOR BIOMASS FAST PYROLYIS. In *Dissertations, Master's Theses and Master's Reports*. Retrieved from https://digitalcommons.mtu.edu/etdr/313

Westover, T. L., Phanphanich, M., Clark, M. L., Rowe, S. R., Egan, S. E., Zacher, A. H., & Santosa, D. (2013). Impact of thermal pretreatment on the fast pyrolysis conversion of southern pine. *Biofuels*, *4*(1), 45–61. https://doi.org/10.4155/bfs.12.75

3. Properties of Torrefied U.S. Waste Blends

3.1. Summary

Power generation facilities in the U.S. are looking for a potential renewable fuel that is sustainable, low-cost, complies with environmental regulation standards and is a drop-in fuel in the existing infrastructure. Although torrefied woody biomass, meets most of these requirements, its high cost, due to the use of woody biomass, prevented its commercialization. Industrial waste blends are suitable for torrefaction and are an economically viable solution, this may prolong the life of some of the existing coal power plants and provide a renewable (partially) solid fuel to be used in for power production applications. We focus on the torrefaction dynamics of the paper fiber-plastic waste blend of 60% fiber and 40% plastic and the characterization of its torrefied product as a function of reaction extent (mass loss). Two forms of the blend are used, one is un-densified and the other is in the form of pellets with three times the density of the un-densified material. Torrefaction of these blends was conducted at 300°C in the mass loss range of 0-51%. The torrefied product was characterized by moisture content, grindability, particle size distribution, energy content, molecular functional structure, and chlorine content. It was shown that although torrefaction dynamics of the two forms differs significantly from each other, their properties and composition depend on the mass loss. Fiber content was shown to decrease relative to plastic upon the extent of torrefaction. Further, the torrefied product demonstrates a similar grinding behavior to Powder River Basin (PRB) coal. Upon grinding, the fiber was concentrated in the smaller size fractions, while the plastic was concentrated in the larger size fractions.

3.2. Introduction

The U.S. Environmental Protection Agency (EPA) has accelerated regulatory pressure on utilities burning pulverized coal by issuing carbon emission guidelines on June 18, 2014. (US-EPA, 2014). The EPA has proposed state by state goals to achieve CO_2 emission reductions; 30% from the power sector as compared to CO_2 emission levels in 2005 (US-EPA, 2015). The ultimate fate and form of the EPA proposed rule may not be known for some time until the rule-making process is complete but the past history of utility emissions regulation and Supreme Court decisions on EPA rule-making authority indicate a high probability that some form of CO_2 regulation will be implemented (White 2014). Internationally, the U.S. has announced the reduction of greenhouse gas emissions by 26-28% below 2005 levels by 2025 (Nakamura and Mufson, 2014).

Torrefied-biomass is a high-energy fuel that can be used in combustion, gasification, and pyrolysis, and is considered either fully or partially renewable and complies with the above EPA regulations (US-EPA, 2015). Kiel (Kiel, 2012) suggested the use of biomass for coal power plants. Potential users of torrefied biomass are suggested for refineries to produce bio-oil (De Rezende Pinho et al., 2017; Wang, Li & Fang., 2016) and syngas producers (TRI, 2018). A considerable amount of studies, pilot-scale plants, patents, and commercial efforts have been devoted to torrefaction and torrefied materials. The entries “torrefaction” and “torrefied” in the title, shows 790 papers, 19 reviews, and 50 patents, between 1990 and 2017. The 50 patents comprise many technologies for torrefaction, most of which are based on mechanical mixing. Although torrefaction technology is well developed, it has not yet moved to the commercial market. The consensus is that the main hindrance to the commercialization of this technology is the use

of high-cost woody biomass as a feedstock (Kumar, Koukoulas, Mani, & Satyavolu, 2017; Radics, Gonzalez, Bilek, & Kelley, 2017).

The use of wastes (for example, municipal solid wastes – MSW – or industrial manufacturing residuals – fiber and plastic blends) can be the answer to the deployment of this technology as tipping fees are paid for the waste destined for landfill. U.S. wastes possess substantial energy content that can be utilized for energy and power (US-EIA, 2010). Wastes, as a feedstock in torrefaction, has been suggested by Bar-Ziv et al. (Bar-Ziv & Saveliev, 2013; Bar-Ziv, Klinger, Zinchik, & Donepudi, 2016) and others, using regular torrefaction (Yuan et al., 2015), wet torrefaction (Mumin, Prawisudha, Zaini, Aziz, & Pasek, 2017), and microwave torrefaction (Iroba, Baik, & Tabil, 2017a, 2017b;). Some difficulties have been recognized while using waste for torrefaction because of difficulties in conveying, pretreatment and potential emissions. Other hurdles were also identified while using waste feedstocks in torrefaction: (i) inconsistency in feedstock, (ii) possibility of high Cl, S, and N content, (iii) binders required for compaction of torrefied biomass (Bar-Ziv & Saveliev, 2013; Bar-Ziv et al., 2016), (iv) high moisture content in MSW and the like, and (v) high contaminant content that leads to emissions issues.

The EPA regulatory actions (US-EPA, 2014; US-EPA, 2015) regarding the use of alternative fuels raise the likelihood that torrefied waste will find a market to replace pulverized coal in energy production. One other recent development affecting the market for torrefied biomass from MSW was a memorandum from the EPA's Office of Air and Radiation addressing the framework for determining the carbon neutrality of biomass (McCabe, 2014).

There is a significant amount of waste in the U.S., which is being disposed of in landfills, that can be used as an energy source. Table 3.1 summarizes the various wastes, totaling ~110,000 ton per year, as well as their calorific values. This significant amount, if torrefied, can replace coal and be considered renewable and clean fuel. From an energy perspective, except plastic wastes with very high heat content ~ 36 MJ/kg, the rest have heat values in the range 15-17 MJ/kg. The weighted average heat content in U.S. waste is ~21 MJ/kg, which is comparable to that of Powder River Basin (PRB) coal that has a heat content of ~ 17 to 19 MJ/kg (Luppens, 2011). This indicates that 1 dry ton of U.S. waste can replace 1 ton of PRB coal. With current coal consumption of ~650,000 tons/d of coal in the U.S. (with over 50% PRB coal) (US-EIA, 2018), U.S. waste could replace well over 15% of the U.S. coal.

Table 3.1. U.S. wastes, quantities and heat content. *

Waste type	Quantity, in 1000 ton	%	Heat content (db), MJ/kg	Source
Paper	19,470	18%	14.7	Demirbas, 1999
Plastic	25,100	23%	35.7	Themelis and Mussche, 2014
Rubber and leather	4,150	4%	36.5	Unapumnuk et al., 2006
Textile	10,000	9%	17	Miranda et al., 2007
Wood	11,010	10%	15-16	McKendry, 2002
Food	29,319	27%	15-16	US-EIA, 2010
Yard trimmings	10,790	10%	15-16	McKendry, 2002
Total	109,839	100%	-	-

*There is a discrepancy between the data of the references presented in this table and the data presented by EPA in 2018 (US-EPA, 2018). EPA reported a total of 232,430 ton per year of generated solid waste.

The present paper deals with torrefaction of certain U.S. wastes, including plastics, which can be converted into drop-in fuels as a replacement of coal in coal power plants. Specifically, the paper deals with wastes blends from the paper/carton (wood fibers) and

plastics. As such, the torrefied fuel should be shown to match the characteristics and properties of coals.

3.3. Materials and methods

3.3.1. Materials

Table 3.2. Properties of CE material averaged over a seven-year period.

Proximate	Values	Ash	Values, %	Other	Values, ppm	Fusion Temp	Value °C
Moisture, %	3.3±0.5	SiO2	33±18	Cl	1162±487	Reducing	
Ash, %	6.0±0.6	A2O3	27±11	F	75±75	Deformation	1,319
Volatiles, %	83.5±2.6	TiO2	7.2±3.4	Hg	0.01±0.01	Softening	1,359
Fixed Carbon, %	7.2±2.0	Fe2O3	0.9±0.9	Sn	2.9±0.9	Hemispherical	1,374
Sulfur, %	0.2±0.1	CaO	21±12	As	1.1±0.9	Fluid	1,396
HHV, MJ/kg	26.1±1.1	MgO	3.0±3.0	Be	0.3±0.8	Oxidizing	
Ultimate	Values, %	K2O	0.6±0.4	Cr	2.2±1.2	Deformation	1,327
Carbon	55.4±1.8	Na2O	1.6±0.7	Co	0.21±0.16	Softening	1,369
Hydrogen	7.9±0.3	MnO2	0.02±0.01	Pb	1.1±1.4	Hemispherical	1,384
Nitrogen	0.3±0.1	BaO	0.2±0.2	Ni	0.81±0.57	Fluid	1,406
Oxygen	27.1±1.6	Others	2.8±1.4	Se	1.5±1.8		

Convergen Energy (CE) developed a fuel, by sorting and blending feedstocks of fiber and plastic, removing metal and shredding down to 25 mm by 1 mm flakes by which waste blends of fibers (from paper, label matrix residuals, and laminated non-recyclable papers/plastics and the like) and plastics, become uniform, flowable and consistent, with a bulk density in the range 200-300 kg/m^3. CE also developed a pelletization process that produces pellets (12 mm OD and 50 mm long) that are rather uniform with a density of

750-800 kg/m^3 and bulk density of 400-450 kg/m^3. The binder for the CE palletization process was the plastic component in the blend.

CE characterized their product for over seven years with properties that showed rather consistent products. Table 3.2 shows the average properties of waste blends of 60% fiber with 40% plastics, with standard deviations of its product over a seven-year period. As seen, the properties in Table 3.2 are indicative of reproducible and consistent material. This material was the feedstock in the torrefaction process, both in un-densified and densified forms.

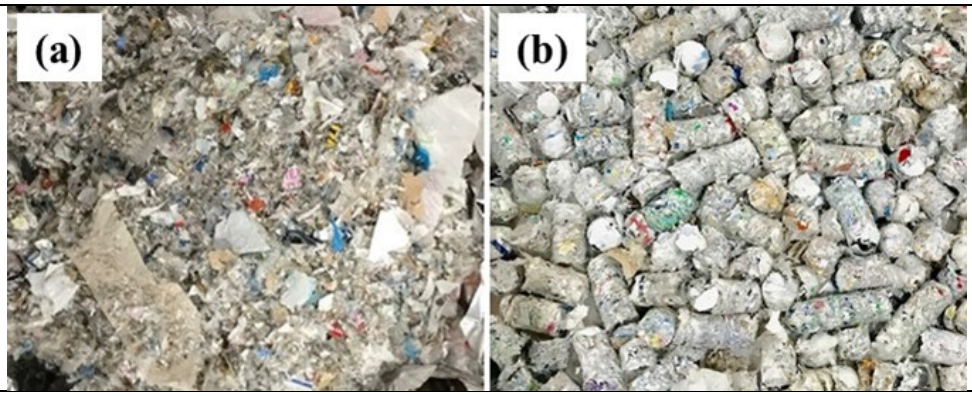

Figure 3.1. (a) Un-densified CE material. (b) Densified (pellets) CE material.

In this study, both the un-densified as well as the densified material (pellets indicated above) were used. Figure 3.1 shows both forms before torrefaction, used in this study: (a) un-densified CE material; and (b) CE pellets.

3.3.2. Waste and product characterization

The properties depicted in Table 3.2 are part of the routine characterization of CE products, both before and after pelletization. Other characterization methods are as follows. All data presented in this paper were averaged over 3-5 data points.

3.3.2.1. Grinding

Grindability is an important characteristic that has an essential impact on the applicability of torrefied material as a drop-in fuel in coal power plants. Typically, coal power plant use pulverizers of type MPS 89 (Storm, 2009), however, for the grinding tests, blade grinders (that operate at 24,000 rpm) were used. The grinding results presented in this paper are for comparison purposes. Two blade grinders were used in this study: Model CIT-FW-800 and Model CIT-FW-200. An on-line power meter - Wattsup pro was used for power vs. time measurements. Also, note that CE material was torrefied in both non-densified and densified (pellets) forms and grinding tests were carried out for both materials. Two types of grinding tests were performed as follows:

(vi) A 100-200 g torrefied sample (either un-densified or pellet form) was placed in the grinder, which was continuously operated for up to 120 s time interval (to avoid damage to the motor); the power was measured continuously during the experiment. If necessary, grinding was repeated in a similar manner for a total of 1800 s.

(vii) A 100-200 g torrefied sample was placed in the grinder and operated for short time intervals - 15-30 s. After each grinding run (time interval) the pulverized material was sifted to seven sizes, in the range of 150-2,000 μm, after which all size fractions were mixed and were further pulverized for another time interval. This process was repeated until the size fractions reached asymptotic values.

In both methods, the power was measured with and without the sample in the grinder. The power without the sample was subtracted from that with the sample, which

provided the net power required to grind the sample. Figure 3.2 shows a typical plot of power vs. time with and without a sample (in this case, 200 g of a torrefied non-densified material at 21.4% mass loss during torrefaction). Note that the startup is accompanied by an overshoot, in both cases.

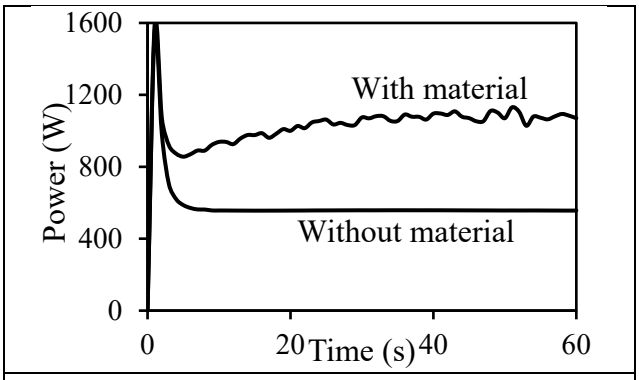

Figure 3.2. Examples of power vs. time traces of the grinder without material and with 200 g torrefied un-densified material.

3.3.2.2. Sifting

Sifting of the pulverized material was carried out in a W.S Tyler, RX-86 model sieve shaker. Seven size fractions were obtained with screen sizes of 75 µm, 150 µm, 180 µm, 250 µm, 425µm, and 850 µm. At each time interval after grinding, all the material inside the grinder was taken out and put into the shaker to sift for an hour. The weights of all the screens before and after the sifting were measured. The difference in these weights provided the sample weight of each size fractions.

3.3.2.3. Heat content

Heat content was measured by Parr 6100 Compensated Jacket Calorimeter, where 1 g samples were placed inside sampling bowl/tray, and the sample was connected to the electric circuit using fuse string. This setup was put into a bomb and then filled with

oxygen. The bomb was then put into a bucket with 2,000 ±0.5 g of distilled water. The process involved the ignition of the sample using an ignition circuit and subsequent measurement of temperature difference after the burning of the measured sample. The heating value was displayed by the calorimeter based on the calibration and temperature difference.

3.3.2.4. Moisture content

Moisture content was measured using HFT-1000 moisture analyzer. Around 1 g of sample was put into the analyzer. After starting the analysis, the heating coil would heat up and the moisture inside the material would volatilize. The analyzer would show the moisture content by measuring the difference of the weight before and after the experiment. Moisture content was measured before and after torrefaction. The values were rather consistent before torrefaction moisture was in range 2-3% and after torrefaction, 0%.

3.3.2.5. Density measurements

Density measurement of pellets was done using a scale (model A&D HR-60) with a readability of 0.0001 g. The Archimedes' principle/buoyancy method was used for density measurement. A simple stand with suspended metal wire setup was used to dip the pellet in water. The procedure followed was as below:

(viii) The pellet was placed on a scale and dry weight, *w*, was noted.

(ix) A beaker filled with a set level of distilled water was placed on the scale and tared zero.

(x) The stand and wire setup were placed next to scale such that some part of wire dipped in the water. The scaled was tared zeroed again.

(xi) The sample was attached to a wire and the sample was dipped in water. Care was taken that entire sample dipped in well and did not touch the bottom of the beaker. The reading with the suspended sample, w_s, was noted.

The density was obtained from the ratio of suspended sample weight, w_s and dry weight w.

3.3.2.6. FTIR

FTIR spectra were obtained on (i) 20 randomly selected pieces of mixed waste and (ii) screened fractions of the torrefied material (in triplicate) using a Nicolet-iS5 FTIR spectrometer, 64 scans, with an attenuated total reflectance accessory (ZnSe crystal, iD5) and data analyzed and averaged with the OMNIC v9.8 software and Aldrich, Hummel, and Nicolet spectral libraries. Carbonyl index (CI), cellulose index (CeI), and hydroxyl index (HI) were calculated as the ratio of the band intensity (absorbance) at 1720 cm^{-1}, 1024 cm^{-1}, and 3342 cm^{-1}, respectively, to the band 2916 cm^{-1} for the -CH_2- groups (Wei, McDonald, Freitag & Morrell, 2013).

3.3.3. Experiments

3.3.3.1. Torrefaction

Torrefaction experiments were carried out by placing a motionless sample at the center of a convection furnace, Lindenberg/Blue type BF51828C-1, with the flow of inert gas, either N_2 or CO_2 to avoid oxidation of the material. For un-densified CE material,

typically samples of 150 g were placed in a thin aluminum foil at the furnace center, with residence time in the range 1-40 min. For CE pellets, the sample size was ~300 g and torrefaction residence time was between 3 to 120 min.

3.4. Results

3.4.1. Torrefaction

As mentioned, all current torrefaction experiments were carried out by introducing un-densified material and pellets in a convective furnace at 300 ^{o}C, with the initial temperature of the particle, T_o, at ambient temperature. The material was placed in the furnace center and was kept stationary. In this case, the particle was heated by heat transported from the hot walls at temperature (T_w) to the particle surface by convection; the heat was then transported into the particle by conduction. Numerous torrefaction experiments were carried out for pellets as well as un-densified material. In both cases, the results show clear trends, with a delay in the onset of mass loss followed by an increase in the mass loss with time. The dynamic behavior in the two cases differed significantly from each other; for the un-densified material, the mass loss starts at around 3 min, whereas for the pellets, it starts at around 9 min. Further, for the un-densified material, mass loss increase with time was faster compared to pellets. This behavior was indicative of the heat-transfer-chemical-reaction system. To determine the regime that best fits the description of the system behavior, one should start with the analysis with Biot number (Bi) and thermal Thiele modulus (M); the former is related to the heating regime of the particle, and the latter relates to the propagation of the torrefaction reaction within the particle. The Bi and M, which are defined as:

$$Bi = \frac{h}{\lambda/L_c} \tag{3.1}$$

$$M = \frac{R^{\dagger}}{\lambda/(c_p L_c^2)} \tag{3.2}$$

where h is the convective heat transfer coefficient, λ is the particle thermal conductivity, L_c is the particle characteristic length, $R^{\dagger}$ is the torrefaction reaction rate within the particle, c_p is the particle heat capacity, and ρ is particle density.

The parameters required to determine Bi and M from Eqs. (1) and (2) are not easy to determine as the material is not well defined and therefore, can only provide an estimate. The value of heat transfer coefficient, h, was selected to be 10 (W/m^2-K) and was the closest to the flow conditions prevailing in the furnace (Incropera & DeWitt, 2002). The value for thermal conductivity, λ, varies between 0.15 (W/m-K) for PVC, to 0.38 (W/m-K) for polyethylene (Incropera & DeWitt, 2002; Patterson & Miers, 2010); for biomass and fibers the values range in 0.03-0.29 (W/m-K) (Mason, Darvell, Jones, Williams, 2016). A value of 0.2 (W/m-K) was selected which was an average of the above. Literature data on reaction rates of the material used were even more scattered than thermal conductivity, therefore they were measured by thermogravimetry in the furnace. The rate of mass loss of the CE material from both measurements at 300 ºC was about 0.03%/s, where the material temperature has been equal to the wall temperature (T_w); using the density of each form to obtain a value of 0.2-0.3 (kg/m^3-s) for the un-densified material and 0.1-0.2 (kg/m^3-s) for the pellets. In this study, the density was 1,150 (kg/m^3) for the un-densified material and 850 (kg/m^3) for the pellets. Heat capacity was both taken from the literature (Incropera & DeWitt, 2002) and measured to yield an acceptable value of 1,600 (J/kg-K) (Donepudi,

2017). The characteristic lengths of the two forms were measured (very accurately for the pellets and rather scattered for the un-densified material).

Table 3.3. Estimated values for the parameters to determine the Bi and M.

Parameter	Value	Source
h, W/m^2-K	10	Incropera and DeWitt, 2002
λ for CE material, W/m-K	0.2	Incropera and DeWitt, 2002
$R^{\dagger}$ for un-densified material, kg/m^3-s	0.3	Measured in current study
$R^{\dagger}$ for pellets, kg/m^3-s	0.2	Measured in current study
ρ for un-densified material, kg/m^3	1150	Measured in current study
ρ for pellets, kg/m^3	850	Measured in current study
c_p, J/kg-K	1600	Incropera and DeWitt, 2002 Donepudi, 2017
L_c thickness for un-densified material, m	0.002	Measured in current study
L_c diameter for pellets, m	0.007	Measured in current study
368Bi for un-densified material	0.1	Current result
Bi for pellets	0.35	Current result
M for un-densified material	0.01	Current result
M for pellets	0.08	Current result

Table 3.3 summarizes all properties required for the determination of *Bi* and *M*, yielding values for (i) *Bi* of ~0.1 for the un-densified material and ~0.35 for the pellets and (ii) *M* of ~0.01 for the un-densified material and ~0.08 for the pellets. The values for *Bi* in the range 0.1-0.35 indicate that the rate of heat transfer by convection from the furnace walls to the particle was lower than the rate of heat transfer into the particle. The values of *M* are in the range 0.01-0.08 which indicate that the reaction rate was significantly slower than the heat transfer into the particle, and the particles equilibrate its temperature faster than the reaction rate. This analysis indicates that the reaction propagation was controlled by the rate of heat transfer from the furnace walls to the particle surface, after which the particle temperature equilibrates instantly.

Establishing that the torrefaction reaction rate was controlled by the heat transfer from the walls to the particle surface and that the particle temperature was uniform at all times, means that the reaction propagates with the rate of the ramp-up of the particle temperature. To calculate the particle temperature, the equation of the heat rate, *dQ(t)/dt*, from the walls to the particle surface was needed to be solved, which was equal to

$$\frac{dQ(t)}{dt} = hA[T_w - T_s(t)] \tag{3.3}$$

where Tw and Ts(t)=T(t) are wall and particle surface (or particle) temperatures, respectively. *Q(t)* is the heat required to increase the particle temperature, or

$$Q(t) = mc_p[T(t) - T_o] + mh_r \tag{3.4}$$

where m and c_p are particle mass and specific heat capacity, respectively, T_o is the particle core temperature, which is also equal to the initial temperature of the particle, and h_r is enthalpy of reaction.

It was a challenge to find values for h_r as the torrefied material was not well defined, it comprises fibers (mostly cellulose) and a large variety of plastic materials. Cellulose torrefaction in the 25-300°C temperature range starts as an endothermic reaction and continues as an exothermic reaction (Bates and Ghoniem, 2012). Enthalpies of reaction for plastic in the same temperature range were always positive and vary in the range (12.55-147.86 J/kg) (Zhao, Liu, & Zhang 2017), which is smaller than the value of $c_p(T-T_o)$ (~400 kJ/kg) in Eq. (3.4). Thus, for simplification, this term was ignored. Introducing Eq. (3.4), without h_r, into Eq. (3.3) and integration from T_w to $T(t)$ yields

$$\frac{T_w - T(t)}{T_w - T_o} = e^{-\frac{t}{\tau}} \tag{3.5}$$

where τ is a characteristic time, defined as

$$\tau = \frac{mc_p}{hA} \tag{3.6}$$

For the pellets (cylinders), $\tau_{cyl}=d\rho c_p/4h$ (d is cylinder diameter, ρ is particle density) and for the un-densified material (slab) it is $\tau_{slab}=d\rho c_p/2h$ (d is slab thickness). Rearrangement of Eq. (3.5) yields

$$T^*(t) = 1 - (1 - \frac{T_o}{T_w})e^{-\frac{t}{\tau}} \tag{3.7}$$

T^* is defined as

$$T^*(t) = \frac{T(t)}{T_w} \tag{3.8}$$

To model the mass loss, the torrefaction reaction rate was assumed to be represented by a first-order reaction, which a rather common assumption in many torrefaction studies (Lédé, 2010; Funke, 2017), or

$$R^{\dagger} = \rho \frac{d\alpha(t)}{dt} = -\rho k \alpha(t) \tag{3.9}$$

where $\alpha = m/m_o$ is the ratio of mass-to-initial-mass, k is rate coefficient assumed to follow an Arrhenius behavior,

$$\rho k(T) = A^{\dagger} e^{\frac{-T_a}{T(t)}} \tag{3.10}$$

where $A^{\dagger}$ is a pre-exponential factor and T_a is a characteristic temperature equals $T_a = E_a/R$, E_a is activation energy and R is gas constant. Introducing Eq. (3.10) into Eq. (3.9) and integrating yields an expression for the mass loss, $1-\alpha$, equals

$$1 - \alpha = 1 - e^{-\int_0^t k dt} \tag{3.11}$$

The required values for determining τ, Eq. (3.6), for each case are given in Table 3.3. Introducing these values in Eq. (3.6) yields $\tau_{slab}=184$ (s) and $\tau_{cyl}= 475$ (s), the subscript

slab is for the un-densified material and *cyl* is for the pellets. Using these values, the particle temperatures were calculated and presented in Figure 3.3.

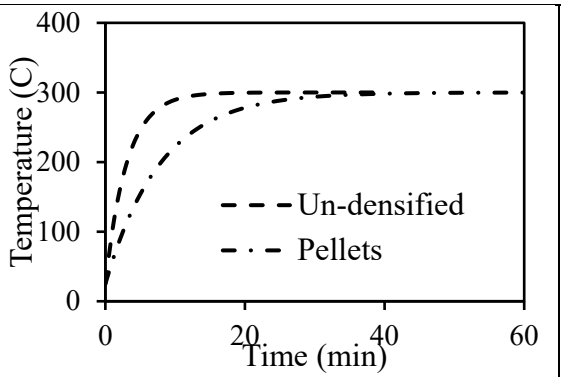

Figure 3.3. Temperature transient for the un-densified material and the pellets, using Eq. (3.7) and characteristic times of 160 (s) for the former and 475 (s) for the later

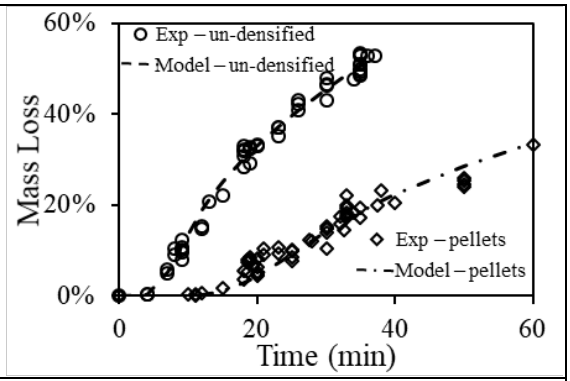

Figure 3.4. Experimental and modeled mass loss transients for the un-densified material and the pellets, using Eq. (3.11), the temperature transients of Figure 3 and fitting for T_a and A†.

As noted, the particle temperature in the un-densified case increases much faster than that of the pellets. Note from Figure 3.3 the temperature of the un-densified material reaches the wall temperature after 10 minutes, whereas for the pellets, it reaches the wall temperature after 30 minutes. The values for $(A^{\dagger}/\rho)$ and T_a were determined by fitting the model results for mass loss of Eq. (3.11), using the temperature transients of Eq. (3.7) (Figure 3.3), to the experimental results. Figure 3.4 shows the measured mass loss vs. time data (scattered results) and the model results using Eq. (3.11). Clearly, the model results yielded an excellent fit to the experimental data. The fitting process yielded for the un-densified material (slab) values of $(A^{\dagger}/\rho)_{slab}=1.23x10^{8}$ and $(T_a)_{slab}=15,200\ (K)$, and for the pellets (slab) values of $(A^{\dagger}/\rho)_{slab}=1.08x10^{8}$ and $(T_a)_{cyl}=15,800\ (K)$. The values of $A^{\dagger}/\rho$ and T_a for both forms of materials are very close to each other which is a strong indication that the model proposed here is representing the actual system behavior rather well.

3.4.2. Grinding energy

The method of determining the grinding behavior has been explained above, with power that was continuously measured as a function of time during grinding for a given sample weight. Numerous grinding tests were conducted, in the mass loss range 10-51%, for the two forms of torrefied materials: un-densified and pellets. All net power transient results portrayed distinct behavior that showed two characteristic times: short and much longer. Further, the net grinding power transients for all samples fitted a double exponential rise of the form:

$$P(t) = a_1\left(1 - e^{-\frac{t}{\tau_1}}\right) + a_2\left(1 - e^{-\frac{t}{\tau_2}}\right) \tag{3.12}$$

where τ_1 and τ_2 are the short (1) and long (2) characteristic times, respectively, and a_1 and a_2 are the asymptotic values of the power for the short and long characteristic times, respectively.

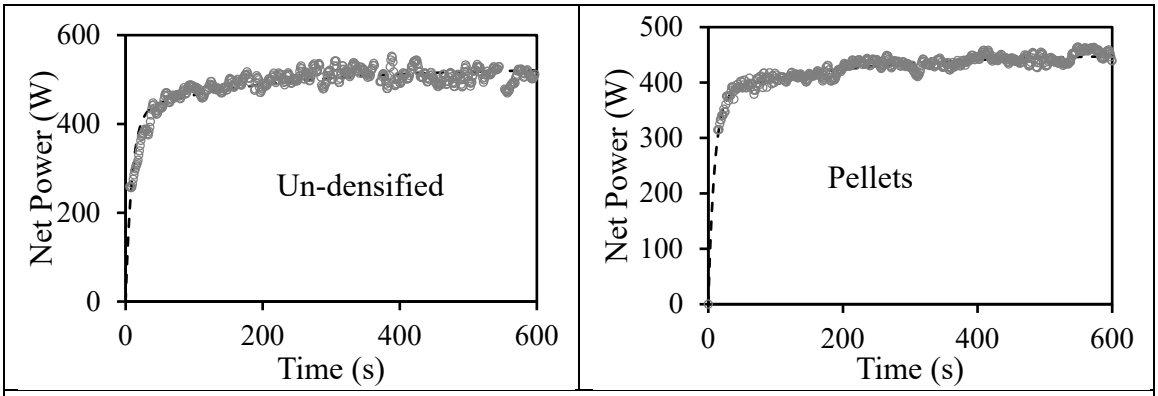

Figure 3.5. Symbols - measured net power vs. time of 200 g samples during grinding of torrefied CE, un-densified material and pellets. Dashed lines, fits of net power to Eq. (3.12) for the short characteristic time, τ_1=9.2s; and characteristic time τ_2=203.0 s.

Figure 3.5 shows typical examples of the measured (symbols) net power vs. time of two 200 g samples during grinding of torrefied CE, un-densified material and pellets

and fits (dashed lines) of the net power to Eq. (3.12). In both cases, the short characteristic time was found τ_1=9.2 s and characteristic time τ_2=203 s.

All results for the torrefied samples and pellets in the range 10-51% mass loss were fitted to Eq. (3.12) to yield: for the short characteristic time of τ_1=*9.1±0.5* s, and for a long time, it was τ_2=*203±10* s with the respective asymptotic values of a_1=*378.1* W and a_2=73.0 W that varied within ±5%. To demonstrate the general behavior of torrefied samples, Figure 3.6 shows normalized net grinding power (by the asymptotic values) vs. time for the short time range, showing clearly identical behavior for all samples tested. The dashed line in the figure is a unity line that shows the normalized asymptotic value. The fact that the grinding dynamics is characterized by two characteristic times, that significantly differ from each other, indicates clearly that there are two materials. A detailed discussion of these two materials is given in the energy content section below.

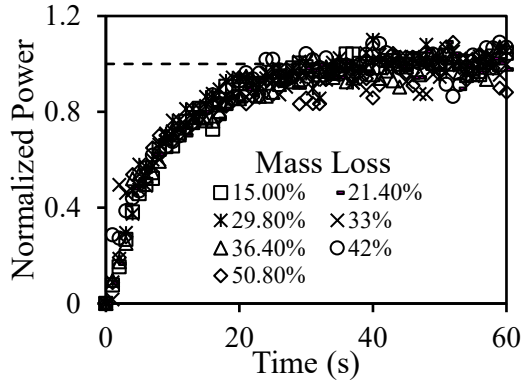

Figure 3.6. Normalized net grinding power vs time for torrefied material at various mass losses; with τ_g=9.1 (s)

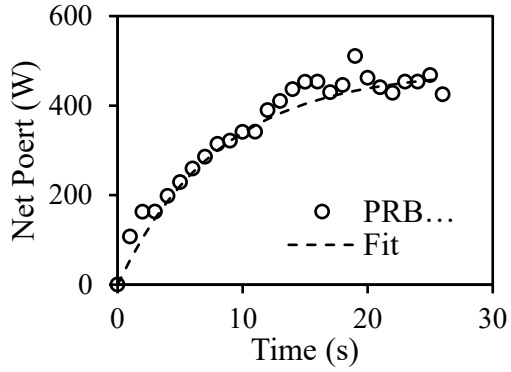

Figure 3.7. Grinding power vs. time for PRB coal with τ_g=9.1 (s).

As will be shown below, most of the material was ground and characteristic grinding energy can be determined by integrating the power over a certain time, which we selected as 1 τ_g, 2 τ_g, and 3 τ_g (or, 8.1 s, 16.2 s, 24.3 s). Table 3.4 shows the values of the

specific grinding energy for three characteristic grinding times, *1* τ_g, *2* τ_g, *3* τ_g, where τ_g *=8.1* (s) in kJ/kg and is commonly used kWh/ton units. As expected, the specific grinding energies increase strongly with the integration time. The values determined here are similar to values obtained in other studies at 8.23 kWh/ton (Khalsa, 2016). For comparison, grinding characteristics of PRB were also studied with power vs. time results for a 200 g PRB coal sample shown in Figure 3.7. A fit of these results with characteristic grinding time, τ_g, of 8.1 was done and specific grinding energies were calculated as shown in Table 3.4. The values for the specific grinding energies for the torrefied (un-densified) material are within the experimental uncertainty to those of the PRB coal and smaller than the energy required to grind the torrefied biomass (Wang et al., 2017).

Table 3.4. Specific grinding energy

Grinding specific energy	Integration time		
	1 τ_g	2 τ_g	3 τ_g
Torrefied un-densified material, kJ/kg (kWh/ton)	9.3±0.8 (2.59)	25.7±1.5 (7.13)	44.7±2.5 (12.4)
PRB coal, kJ/kg (kWh/ton)	8.6±0.5 (2.38)	24.3±1.4 (6.75)	42.4±2.4 (11.8)
Torrefied biomass, kJ/kg (kWh/ton)	N/A	N/A	43-54 (12-15)

3.4.3. Sizing distribution

Many sifting experiments were done as a function of grinding time (or grinding energy), where the samples were sifted in size range 150 µm – 3 mm in 5 size fractions: x<150 µm, 150<x<250 µm, 250<x<425 µm, 425<x<850 µm, x>850 µm (x denotes size). It was observed that after reaching steady-state (i.e., the net grinding power reached an asymptotic value), the size distribution did not change anymore. Therefore, most of the sifting experiments were done after reaching grinding steady state. The initial sample was

around 100 grams, and after grinding and sifting, there was ~ 1 gram of sample loss during the transferring procedure, which occurred only once during the process. Therefore, the loss was not more than 1%. Although there is scatter in the results, there are clear trends: the size fraction >850 µm decreased with mass loss and the size fraction <150 µm increased with mass loss and the size fractions in between did not change much with mass loss. Therefore, the behavior in two size fractions: under and above 850 µm was further investigated. Figure 3.8 shows the size fraction as a function of mass loss for the torrefied un-densified material and pellets for these two size fractions. It is interesting to note that for each size fraction, the dependence on mass loss is rather similar (the line is a fit to a straight line). For the size under 850 µm, its fraction starts at 82% for 4.5% mass loss and reaches almost 100% at 51% mass loss, the size fraction above 850 µm balances the smaller size fraction.

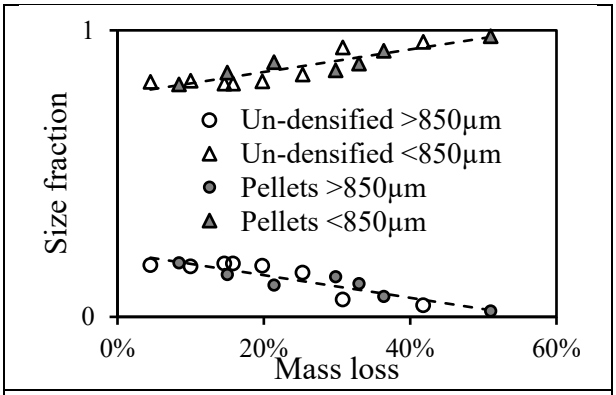

Figure 3.8. Size fraction for the torrefied un-densified material and pellets vs. mass loss for size fractions under and above 850 µm.

Table 3.5 shows fraction<74 µm of pulverized torrefied material at various mass losses. The table indicates that above 8.4% mass loss, after grinding the fraction of <74 µm

is >70%, which is consistent with of the typical coal power plant requirements (Helble, Srinivasachar & Boni 1990).

Table 3.5. Fraction <74 µm of torrefied material in various mass losses

Mass loss	Fraction <74 µm
8.4%	67.0%
15.0%	73.9%
21.4%	77.3%
33.0%	77.5%
36.4%	89.2%
51.0%	95.4%

3.4.4. FTIR spectroscopic characterization

The CE waste mix plus fiber (20 random pieces selected) was analyzed by FTIR spectroscopy to determine their chemical identity with spectra library matching. The mix was shown to be comprised of three cellulose/paper, three polypropylene (PP), three polyethylene (PE), four polyethylene terephthalate (PET), silicone, three cellulose/silicone mix, two paper/acrylate mix, and one nylon samples. A composite FTIR spectrum is shown in Figure 3.9a and shows the major bands associated with PE, PP, PET, and paper. No characteristic bands at 610 cm^{-1} (C-Cl stretch) and 1425 cm^{-1} (C-H_2 bending) were observed for polyvinylchloride (Krimm, 1963).

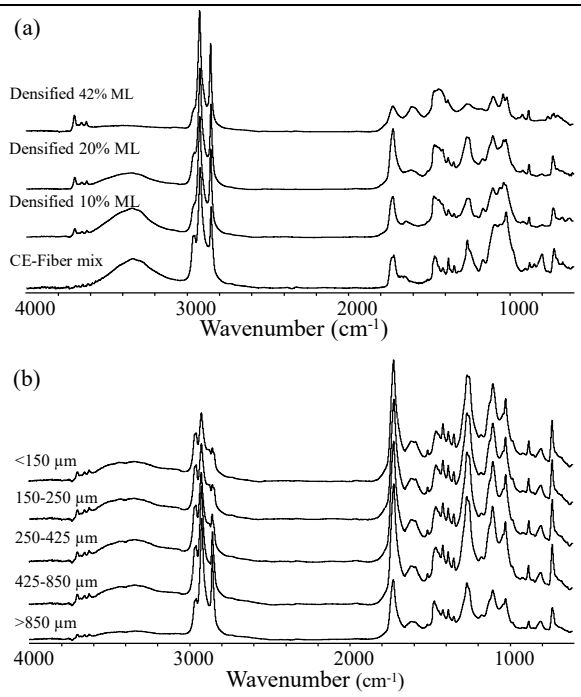

Figure 3.9. FTIR spectra of (a) CE-fiber mix and ground/screened (425-850 µm) torrefied (10, 20 and 42% mass loss) densified material and (b) ground/screened (<150 µm, 150-250 µm, 250-425 µm, 425-850 µm, and >850 µm) un-densified torrefied (30% mass loss) material

The major chemical changes that occurred upon torrefaction on densified and un-densified material and subsequent particle screening (<150 µm, 150<x<250 µm, 250<x<425 µm, 425<x<850 µm, and >850 µm) after grinding were also monitored by FTIR spectroscopy. The spectra for the ground screened 425<x<850 µm fraction for the densified torrefied (10, 20 and 42% mass loss) material as well as the CE-fiber mix are shown in Figure 3.9a. The spectra for the ground screened fractions for the un-densified torrefied (30% mass loss) material are shown in Figure 3.9b. Specific spectral bands can provide information on specific chemical changes that occur during thermal treatment (Balogun, Sotoudehniakarani, McDonald, 2017). All the samples had C-H stretching bands at assigned to methyl (2960 cm^{-1} and 2870 cm^{-1}) and methylene (2916 cm^{-1} and 2850 cm^{-1}) groups mainly associated with PP and PE plastic (Mayo, 2004a). In the ground screened

torrefied material, plastic was generally concentrated in the larger sized fractions (425<x<850 µm and >850 µm) (Figure 3.9b). The O-H stretching band 3100-3600 cm^{-1} was present in all samples and progressively decreased in intensity upon the extent of torrefaction due to dehydration reactions (Wang et al. 2014) (Figure 3.9b). A broad carbonyl (C=O) band at 1690-1750 cm^{-1} was observed and assigned to mainly an ester in linkage in PET and acrylate and an amide linkage in nylon (Mayo, 2004b). A small band at 1505 cm^{-1} was assigned to lignin from paper (Faix, 1992). The spectral region between 1000 and 1070 cm^{-1} has been assigned to C–O stretching in wood cellulose and hemicellulose and decreased in intensity with torrefaction mass loss (Pandey, 1999). All samples were shown to have cis- and trans-vinylene bands at 727 cm^{-1} and 974 cm^{-1}, respectively (Miller, 2004).

The relative changes in carbonyl, cellulose and hydroxyl content to methylene groups (plastic) that occurred during torrefaction were examined by calculating CI, CeI and HI, respectively (Figure 3.10). Low values of CI, CeI, and HI means that there was a higher level of polyolefin plastic in the material. The CI generally decreased for all torrefied samples with an increase in particle size (from <150 µm to 425<x<850 µm), except for the >850 µm fraction (Figure 3.10a).

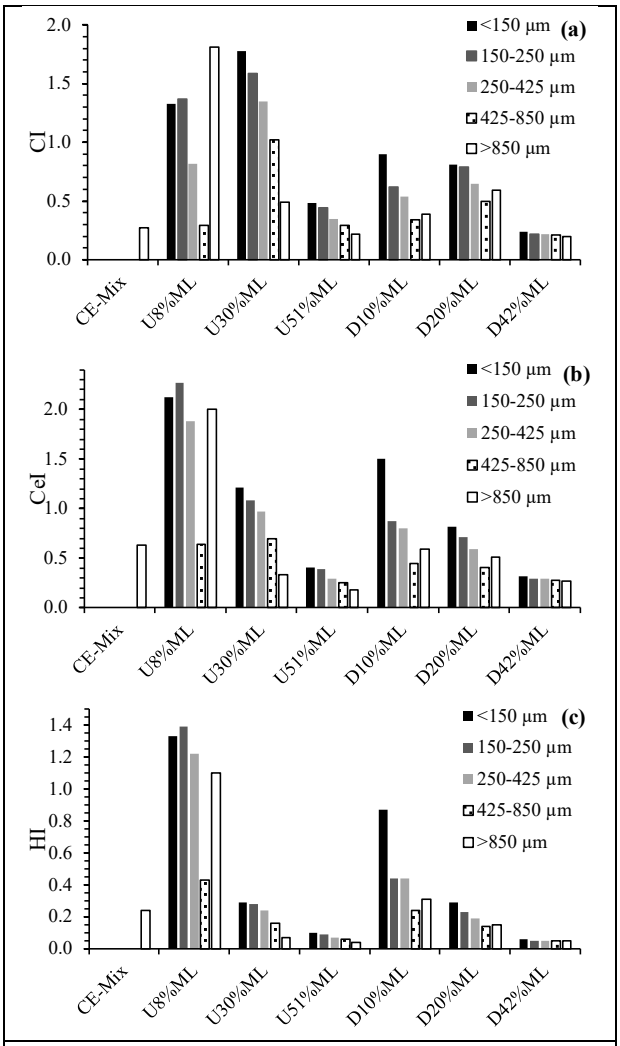

Figure 3.10. Plots showing changes in (a) carbonyl index (CI), (b) cellulose index (CeI), and (c) hydroxyl index (HI) for ground screened fractions (<150 µm, 150<x<250 µm, 250<x<425 µm, 425<x<850 µm, and >850 µm) of torrefied densified (D) and un-densified (U) material

For example, in the 30% mass loss torrefied material the CI decreased from 1.78 to 0.49 going from <150 µm to >850 µm particle size. For the low to moderate level of torrefaction (8-20% mass loss) the >850 µm fraction the higher CI values could be associated with higher levels of PET plastic. Furthermore, the CI levels were also shown to decrease, associated with cleavage of the ester linkages in PET/acrylates and removal of

the volatile degradation products (Cepeliogullar and Putun, 2014), with the extent of torrefaction. Generally, for both CeI (Figure 3.10b) and HI (Figure 3.10c) decreased for all torrefied materials as screened particle size increased (<150 µm to >850 µm), suggesting that the cellulose fiber was mainly in the finer screened fractions. For example, in the 30% mass loss torrefied material the CeI and HI respectively decreased from 1.21 to 0.33 and 0.29 to 0.07 going from <150 µm to >850 µm particle size. Again, at low-moderate torrefaction levels (8-20% mass loss), the CeI and HI levels were high, suggesting that undegraded paper fragments were collected in the >850 µm fraction. Moreover, Both CeI and HI were shown to decrease as torrefaction severity increased. These findings support that the cellulose content decreased relative to plastic with the extent of torrefaction as a result of dehydration and degradation reactions (Wang et al. 2014).

3.4.5. Energy content

The energy content was originally measured for un-sifted pulverized samples; however, it was discovered that scooping a sample of 1 g for the heat content test from a 200 g of the pulverized material gave very large scatter in the measured value. This was because the pulverized material has a large size distribution (as observed above) and the scooping did not necessarily give uniform size distribution. Therefore, it was decided to measure the heat content for five size fractions: $x<150$ µm, $150<x<250$ µm, $250<x<425$ µm, $425<x<850$ µm, and $x>850$ µm separately. Although the heat content for all sifted samples in these size fractions, for the sake of brevity heat content was shown for the following consolidated fractions: $x<150$ µm, $150<x<850$ µm, $x>850$ µm, and the calculated

total heat content (from the fraction and heat content for each fraction). Heat content results presented here are the dry- ash-free basis.

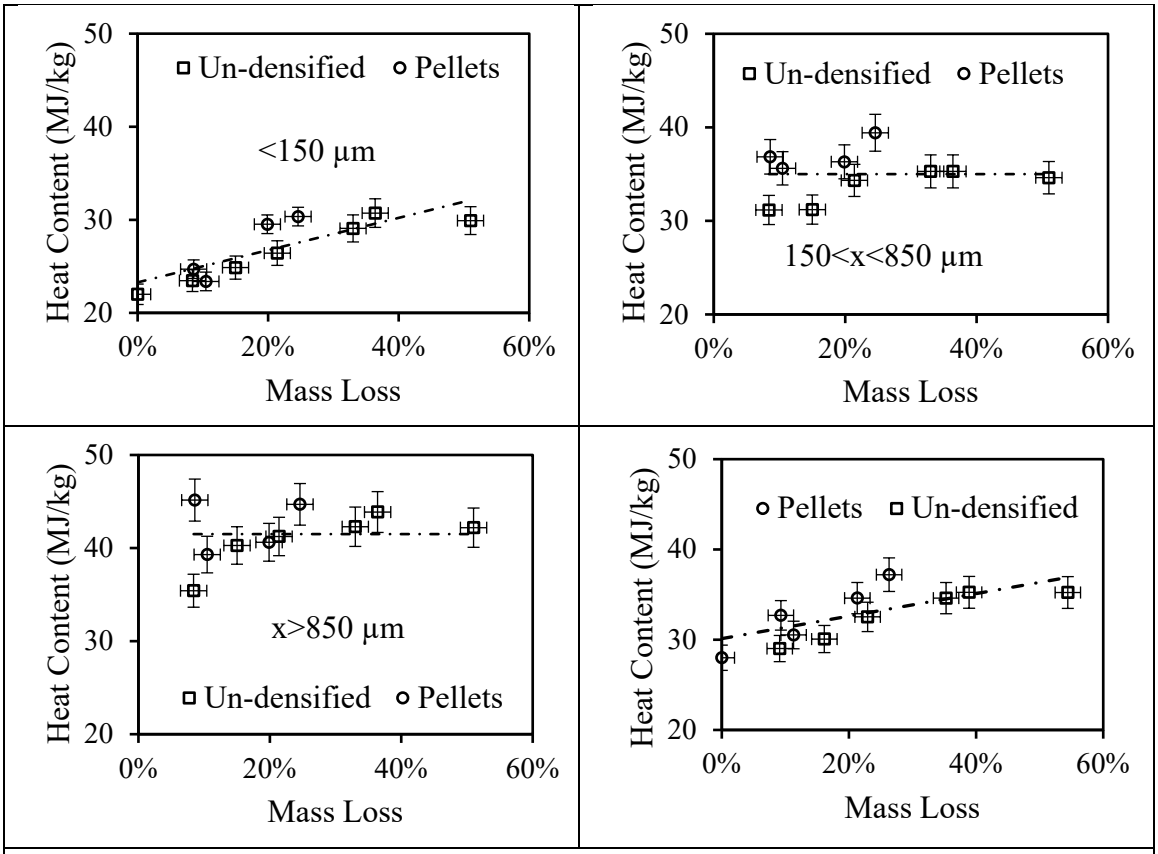

Figure 3.11. Top left. The heat content of the size fraction x<150 µm. Top right, same for 150<x<850 µm. Bottom left. Same for x>850 µm. Bottom right. Total heat content.

Figure 3.11 Top-left is a plot of the heat content of the x<150 µm fraction as a function of mass loss. The point at zero mass loss is the heat content of the blend prior to torrefaction and the dashed line is a linear trend line to lead the eye. Clearly, the main source of this fraction was pulp fibers that increase heat content with an increase in the mass loss as predicted by Klinger et al. (Klinger, Bar-Ziv & Shonnard, 2013; Klinger, Bar-Ziv, & Shonnard, 2015; Klinger et al, 2015). Figure 3.11 Top-right is a plot of the heat content of the 150 µm<x<850 µm fraction as a function of mass loss. The heat content does not seem to change with mass loss and has an average heat content of 35±3 MJ/kg; this

value was lower than that of plastic and it was assumed as a combination of fiber and plastic materials. Figure 3.11 bottom-left is a plot of the heat content of the x>850 µm fraction as a function of mass loss. The heat content does not seem to change with mass loss and has an average heat content of 41.5±3.0 MJ/kg; this value was similar to most of the plastic material (Sonawane, Shindikar, & Khaladkar, 2013) and thus was attributed as plastic. Figure 3.11 bottom-right is a plot of the total heat content, as calculated from all fractions, as a function of mass loss. The slope of heat content increase was identical to that of the fiber.

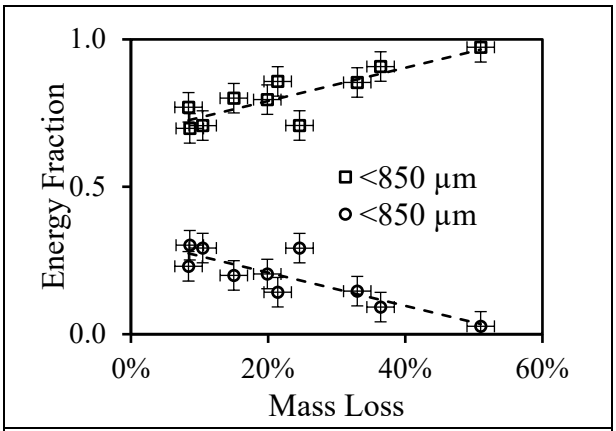

Figure 3.12. The energy contribution of the above and under 850 µm size fractions to the total heat content of both un-densified material and pellets as a function of mass loss.

Although the entire sample was pulverized, two materials (fibers and plastics) clearly retain their original structure which is indicated by the size distribution as shown above and the heat content as shown here. However, this material distinction diminishes as the torrefaction reaction proceeds (seen from the decrease of fraction x>850 µm). To further quantify this process, a plot of the contribution of the <850 µm fraction, which is a combination of torrefied material (from fibers) and fibers and the fraction >850 µm, which

was entirely from plastic. Figure 3.12 shows results of the contribution to the total energy from each fraction, showing that the contribution from plastics was about 20% at about 5-8% mass loss and became zero at 50% mass loss, where the plastic lost its original integrity.

3.5. Conclusions

In the present study blends of fiber and plastic wastes at a ratio of 60:40 (fiber-to-plastic) were used as feedstock for torrefaction. Both the un-densified material and pellets were torrefied at 300 ºC with different time periods. It was observed that the two forms have significantly different torrefaction dynamics. Un-densified material takes less time to start torrefaction compared to the pellets, which is due to the faster heat transfer to the un-densified material. The torrefied samples were characterized by moisture content, grindability, particle size distribution, energy content, molecular functional structure, and chlorine content. It was shown that although torrefaction dynamics is of the two forms differs significantly from each other, their properties depend on the mass loss. The fiber content was shown to decrease relative to plastic with the extent of torrefaction (mass loss) as determined by FTIR spectroscopy. Further, chemical (cellulose, hydroxyl, and carbonyl) changes were also shown to progressively decrease by torrefaction mass loss. Grinding characteristics, size distribution after grinding gave similar results as a function of mass loss during torrefaction, for the forms of material. Further, the torrefied product demonstrates a similar grinding behavior to PRB coal. The heat content of the material with size $x>850$ μm is much higher than that of size $x<150$ μm; the former attributed to the plastic material, whereas the latter was attributed to the fibers. The total heat content was shown to increase with mass loss. Chlorine in the torrefied samples was removed by a high

shear mixing in aqueous solution showing that 5 minutes was sufficient to remove all chlorine after 30% mass loss. Overall, the waste blends studied in this paper showed that they can be used as a drop-in fuel in coal power generation facilities since this fuel is low-cost, it also meets the environmental regulation standard.

3.6. References

Balogun, A., Sotoudehniakarani, F., McDonald, A.G. (2017). Thermo-kinetic, spectroscopic study of brewer's spent grains and characterization of their pyrolysis products. Journal of Analytical and Applied Pyrolysis. 127: 8-16. https://doi.org/10.1016/j.jaap.2017.09.009.

Bar-Ziv, E., and Saveliev, R. (2013). Torrefied-Biomass from Municipal Solid Waste for Power Production. ASME-Power2013-98044.

Bar-Ziv, E., Klinger, J., Zinchik, S., and Donepudi, Y. (2016). Torrefied-Biomass from Municipal Solid Waste for Power Production. ASME-PowerEnergy2016-59179.

Bates, R.B., and Ghoniem, A.F. (2013). Biomass torrefaction: Modeling of reaction thermochemistry. Bioresource Technology 134, 331-340.

Cepeliogullar, O., and Putun, A.E. (2014). A pyrolysis study for the thermal and kinetic characteristics of an agricultural waste with two different plastic wastes. Waste Management & Research 32(10), 971-979.

Demirbas, A. (1999). Physical properties of briquettes from waste paper and wheat straw mixtures. Energy Conversion & Management 40, 437-445.

De Rezende Pinho, A., De Almeida, M. B., Mendes, F. L., Casavechia, L. C., Talmadge, M. S., Kinchin, C. M., (2017). Fast pyrolysis oil from pinewood chips co-processing with vacuum gas oil in an FCC unit for second generation fuel production. Fuel 188, 462-473.

Donepudi, Y. (2017) Impact of pretreatment methods on fast pyrolysis of biomass. [dissertation]. [Houghton (MI)]: Michigan Technological University

US-EPA, Environmental Protection Agency "Carbon Pollution Emission Guidelines for Existing Stationary Sources: Electric Utility Generating Units." Federal Register. Environmental Protection Agency, 18 June 2014. Web. 30 Nov. 2014.

US-EPA, Environmental Protection Agency, 2015, "Carbon pollution emission guidelines for existing stationary sources: electric utility generation units," EPA-HQ-OAR-2013-0602, 1560 pp., published 08-03-2015.

US-EPA, Environmental Protection Agency, "Assessing Trends in Material Generation, Recycling, Composting, Combustion with Energy Recovery and Landfilling in the United States," Report EPA 530-R-17-01, 91 pp., November 2016.

US-EPA. (2018). Advancing Sustainable Materials Management: 2015 Fact Sheet Assessing Trends in Material Generation, Recycling, Composting, Combustion with Energy Recovery and Landfilling in the United States.

Faix, O. (1992). Fourier transform infrared spectroscopy. In: Lin SY, Dence CW, editors. Methods in lignin chemistry. Berlin: Springer-Verlag. p. 83–132.

Funke, A., Henrich, E., Dahmen, N. and Sauer, J. (2017). Dimensional Analysis of Auger-Type Fast Pyrolysis Reactors. Energy Technology 5 (1): 119-129. DOI:10.1002/ente.201600095

Helble, J.J., Srinivasachar, S. and Boni, A.A. (1990). Factors influencing the transformation of minerals during pulverized coal combustion. *Progress in Energy and Combustion Science*, *16*(4), pp.267-279.

Incropera, F.P., and DeWitt, D.P. (2002). Fundamentals of heat and mass transfer. New York: J. Wiley.

Iroba, K.L., Baik, O.D., and Tabil, L.G. (2017). Torrefaction of biomass from municipal solid waste fractions I: Temperature profiles, moisture content, energy consumption, mass yield, and thermochemical properties. Biomass and Bioenergy 106, 8-20. Biomass and Bioenergy 105 (2017a) 320-330.

Iroba, K.L., Baik, O.D., and Tabil, L.G. (2017). Torrefaction of biomass from municipal solid waste fractions II: Grindability characteristics, higher heating value, pelletability, and moisture adsorption. Biomass and Bioenergy 106 (2017b) 8-20.

Khalsa, J., Leistner, D., Weller, N., Darvell, LI., and Dooley, B. (2016). Torrefied Biomass Pellets - Comparing Grindability in Different Laboratory Mills. Energies. Oct 4;9(10):1-16, DOI:10.3390/en9100794

Kiel, J. (2011). Torrefaction for upgrading biomass into commodity fuel. In *Status and ECN Technology Development. EUBIONET III Workshop, Espoo, Finland* (Vol. 15).

Klinger, J., Bar-Ziv, E., and Shonnard, D. (2013). Kinetic study of aspen during torrefaction. Journal of analytical and applied pyrolysis, 104,146-152.

Klinger, J., Bar-Ziv, E., and Shonnard, D. (2015). Unified Kinetic Model for Torrefaction-Pyrolysis, Fuel Processing Technology, 138, 175-183.

Klinger, J., Bar-Ziv, E., Shonnard, D., Westover, T., and Emerson, R. (2015). Predicting Properties of Gas and Solid Streams by Intrinsic Kinetics of Fast Pyrolysis of Wood. Energy and Fuels 30 (1): 318-325. DOI: 10.1021/acs.energyfuels.5b01877

Krimm, S. (1963). Infrared spectra and assignments for polyvinyl chloride and deuterated analogs. Journal of Polymer Science: Part A. 1: 2621-1650.

Kumar, L., Koukoulas, A.A., Mani, S., and Satyavolu, J. (2017). Integrating Torrefaction in the Wood Pellet Industry: A Critical Review. Energy Fuels, 31, 37-54.

Lédé, J. (2010). Biomass Pyrolysis: Comments on Some Sources of Confusions in the Definitions of Temperatures and Heating Rates. Energies 3 (4): 886-898. DOI: 10.3390/en3040886

Luppens, J.A. (2011), A critical review of published coal quality data from the southwestern part of the Powder River Basin, Wyoming: U.S. Geological Survey Open-File Report 2011-1148, 23.

Mason, P.E., Darvell, L.I., Jones, J.M., and Williams, A. (2016). Comparative Study of the Thermal Conductivity of Solid Biomass Fuels. Energy and Fuels 30 (3): 2158-2163. DOI: 10.1021/acs.energyfuels.5b02261

Mayo, D.W. (2004a). Characteristics of alkanes. In: Course Notes on the Interpretation of Infrared and Raman Spectra. Eds. Mayo, D.W; Miller, F.A.; Hannah, R.W., John Wiley & Sons, New Jersey. Pp 33-72.

Mayo, D.W. (2004b). Spectra of carbonyl compounds of all kinds (Factors affecting carbonyl group frequencies). In: Course Notes on the Interpretation of Infrared and Raman Spectra. Eds. Mayo, D.W; Miller, F.A.; Hannah, R.W., John Wiley & Sons, New Jersey. Pp 179-204.

McCabe, J.G. (2014). Addressing Biogenic Carbon Dioxide Emissions from Stationary Sources. United States Environmental Protection Agency.

McKendry, P. (2002). Energy production from biomass (part 2): conversion technologies. Bioresource Technology Volume 83, Issue 1, May 2002, 47-54.

Miller, F.A. (2004). Characteristic frequencies of alkenes (olefins). In: Course Notes on the Interpretation of Infrared and Raman Spectra. Eds. Mayo, D.W; Miller, F.A.; Hannah, R.W., John Wiley & Sons, New Jersey. Pp 73-84.

Miranda, R., Sosa-Blanco, C., Bustos-Martínez, D., and Vasile, C. (2007). Pyrolysis of textile waste I. Kinetics and yields. J. Anal. Appl. Pyrol., 80, 489-495.

Mumin, G.G., Prawisudha, P., Zaini, I.N., Aziz, M., and Pasek, A.D. (2017). Municipal solid waste processing and separation employing wet torrefaction for alternative fuel production and aluminum reclamation. Waste Management 67, 106-120.

Nakamura, D., and Mufson, S. (2014). China, U.S. Agree to Limit Greenhouse Gases. The Washington Post, 12.

Pandey, K.K. (1999). A study of chemical structure of soft and hardwood and wood polymers by FTIR spectroscopy. Journal of Applied Polymer Science. 71: 1969–75.

Patterson, J.E., Miers, R.J., and Carolina, N. (2010). The thermal conductivity of common tubing materials applied in a solar water heater collector, T. Sulbaran (Ed.), 46th ASC Annual International Conference, Wentworth Institute of Technology, Boston, Massachusetts.

Radics, R.I., Gonzales, R., Bilek, E.M., and Kelley, S.S. (2017). Systematic Review of Torrefied Wood Economics. BioResources 12 (3), 6868-6886.

Saleh, S.B., Flensborg, J.P., Shoulaifar, T.K., Sárossy, Z., Hansen, B.B., Egsgaard, H.,(2014). Release of Chlorine and Sulfur during Biomass Torrefaction and Pyrolysis. Energy and Fuels 28 (6): 3738-3746. DOI: 10.1021/ef4021262

Sonawane, Y.B., Shindikar, M.R., and Khaladkar, M.Y. (2017). High Calorific Value Fuel from Household Plastic Waste by Catalytic Pyrolysis, Nature Environment and Pollution Technology, 16(3), 879.

Storm, R.F. (2009). " Blueprint" Your Pulverizer for Improved Performance. *Power*, *153*(3), pp.60-63.

Themelis, N.J., and Mussche, C. (2014). 2014 Energy and Economic Value of Municipal Solid Waste (MSW), Including Non-Recycled Plastics (NRP), Currently Landfilled in the Fifty States.

TRI, ThermoChem Recovery International, (2018). "Reforming gasification," 2017. http://tri-inc.net/steam-reforming-gasification/.

Unapumnuk, K., Keener, T.C., Lu, M., and Khang, S.J. (2006). Pyrolysis Behavior of Tire-Derived Fuels at Different Temperatures and Heating Rates. Journal of the Air & Waste Management Association, 56:5, 618-627, DOI: 10.1080/10473289.2006.10464481

US-EIA, U.S. Energy Information Administration, based on U.S. Environmental Protection Agency, 2010 MSW Facts and Figures Factsheet. https://www.eia.gov/todayinenergy/detail.php?id=8010. Accessed 03-11-2018.

US-EIA, U.S. Energy Information Administration, "Monthly Energy Review," Chapter 6, February 2018, DOE/EIA-0035 (2018).

Wang, C., Li, M., and Fang, Y. (2016). Coprocessing of Catalytic-Pyrolysis-Derived Bio-Oil with VGO in a Pilot-Scale FCC Riser. Ind. Eng. Chem. Res. 55, 3525−3534.

Wang, L., Barta-Rajnai, E., Skreiberg, Ø., Khalil, R.A., Czégény, Z., Jakab, E., Barta, Z., (2017). Impact of torrefaction on woody biomass properties.

Wang, Z., Pecha, B., Westerhof, R., Kersten, S., Li, C-Z., McDonald, A.G., Garcia-Perez, M. (2014). Effect of cellulose crystallinity on solid/liquid phase reactions responsible for the formation of carbonaceous residues during slow pyrolysis. Industrial & Engineering Chemistry Research. 53(8): 2940–2955.

Wei, L., McDonald, A.G., Freitag, C., and Morrell, J.J. (2013). Effects of wood fiber esterification on properties, weatherability and biodurability of wood plastic composites. Polymer Degradation & Stability. 98: 1348-1361.

White, E.D. (2014). The supreme court of the U.S., American Bar Association Journal 7.7 (1921): 341-343.

Yuan, H., Wang, Y., Kobayashi, N., Zhao, D., and Xing, S. (2015). Study of Fuel Properties of Torrefied Municipal Solid Waste, Energy Fuels 2015, 29, 4976-4980, DOI: 10.1021/ef502277u

Zhao, W., Liu, D., and Zhang, Y., (2017). Study on the Influence of Pressure-Assisted Thermal Processing on PET/PE via the Change of Melting Enthalpy. Journal of Food Processing and Preservation, 41(5).

Zhu, Q. (2014). Coal sampling and analysis standards. IEA Clean Coal Centre, London, United Kingdom, 64-65.

Zinchik, S., Klinger, J. L., Westover, T. L., Donepudi, Y., Hernandez, S., Naber, J. D., & Bar-Ziv, E. (2018). Evaluation of fast pyrolysis feedstock conversion with a mixing paddle reactor. *Fuel Processing Technology*, *171*, 124–132. https://doi.org/10.1016/j.fuproc.2017.11.012

4. Properties of torrefied pellets of U.S. wastes

4.1. Summary

With the continued growing U.S. population, solid waste generation will increase, which will lead to undesired and significant growth in landfilling. Thermal treatment can turn these high calorific value wastes into clean fuels that can be used in small-to-large power plants. This article focuses on using blends with 40% plastic and 60% fiber wastes and converting them into clean and densified solid fuel by torrefaction and extrusion. The material was torrefied at 300 °C to obtain torrefied samples with different mass losses, ranging from 0% to a maximum of 51%. The torrefaction results showed a clear synergy between plastics and fibers. The torrefied material was then extruded into 9 mm diameter rods and the products were characterized by molecular functional group analysis, thermomechanical analysis, dynamic mechanical analysis, dynamic rheological measurement, density measurement, flexural testing, water absorption test, size distribution measurement, heat content test, and combustion test. The fiber content in the material decreased as mass loss increased, and the process reduced significantly the variabilities of the material. The heat content increased as the mass loss increased. The plastic in the feedstock acted as a process enabler as it imparted properties like bindability, water resistance, high heat content, and increased degradation reaction rate.

4.2. Introduction

The world is witnessing an unprecedented accumulation of solid wastes with significant, well-documented ecological, environmental, health, and economic consequences (El-Fadel Findikakis, & Leckie, 1997, Arias, et al, 2008). As population increases, the levels of wastes will continue to grow, especially the plastic waste levels that hugely impact landfilling and have been exacerbated by China's ban on plastic waste import (China Daily, 2018). Commingled Plastic waste usually ends up in the landfills since it is not suitable for recycling, thus creating severe problems as well as opportunities for waste management. However, a thermal treatment could turn this feedstock into a clean, safe and low-cost drop-in fuel for the existing power plants.

Torrefied biomass has been proposed as a coal substitute for power generation (Kiel, 2011) and it complies to EPA regulations (US-EPA, 2015) as well as contributes to reduction of greenhouse gases (GHG) (Tsalidis, Joshi, Korevaar, & Jong, 2014; Nunes, Matias, & Catalão, 2014). Torrefaction technology has reached a level of maturity that it can be commercially used, however, it has not yet moved to the market. Three major hindrances to the commercialization of this technology have been identified: (1) the high cost associated with woody biomass feedstock (Kumar Koukoulas, Mani, & Satyavolu, 2017; Radics, Gonzales, Bilek,, & Kelley, 2017), (2) the degradation of lignin during torrefaction (Park et al., 2013), hence lack of a binder for compaction, and (3) the high reactivity of torrefied biomass, as self-heating of the material due to slow oxidization, that imposes tremendous safety risks during the process, transportation, storage and the operation in the power plant (Arias et al., 2008, Ceballos Hawboldt, & Hellleur, 2015). In

this study, we used blends of plastic and fiber wastes as a feedstock, which overcome the above hindrances.

4.3. Materials and methods

4.3.1. Materials

The samples used in this study were a fiber-plastic waste blend (40% plastic and 60% fiber) obtained from Convergen Energy LLC (CE). The wastes blends received by CE comprises a large variety of paper, laminated papers, plastics, and fibers consisting of several impurities (Figure 4.1). CE has been tracking the properties of the waste blends for seven years, and the results are shown by Xu et al. CE removed any ferrous metals using a strong electric magnet, while non-ferrous were removed manually. The material was then shredded to 75-125 mm particle size by a shear grinder and then air-dried to 5-7% moisture content level (Xu et al., 2018).

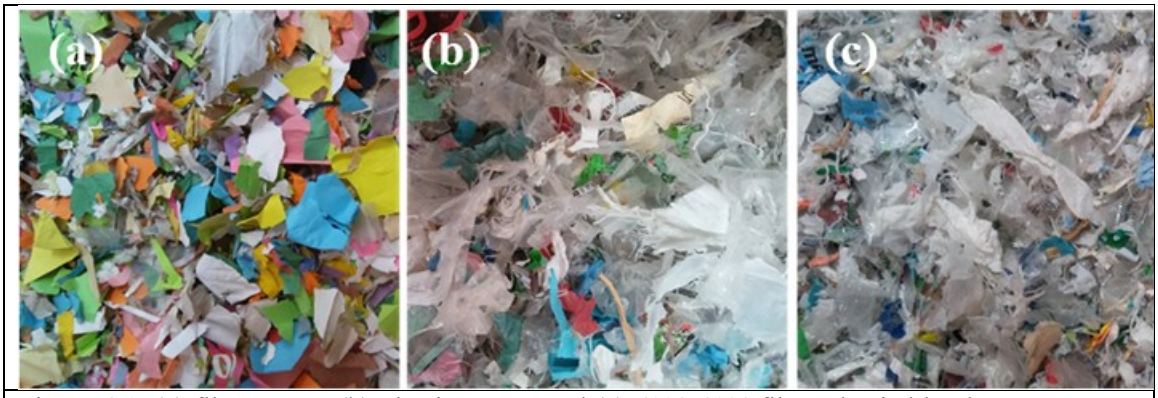

Figure 4.1. (a) fiber waste, (b) plastic waste, and (c) 60%-40% fiber-plastic blend.

4.3.2. Torrefaction

The sample was torrefied by introducing ~150 g of CE waste blends to an aluminum pan that was placed in the center of a muffle furnace (Lindenberg/Blue type BF51828C-1)

heated to 300 °C for 3 to 60 min (Xu et al., 2018). An inert gas purge, either Carbon Dioxide or Nitrogen, was flown at a rate of 30 L/min to avoid oxidation. Figure 4.2 shows a schematic of the torrefaction system. In this study. mass loss was the dependent variable measured as a function of time.

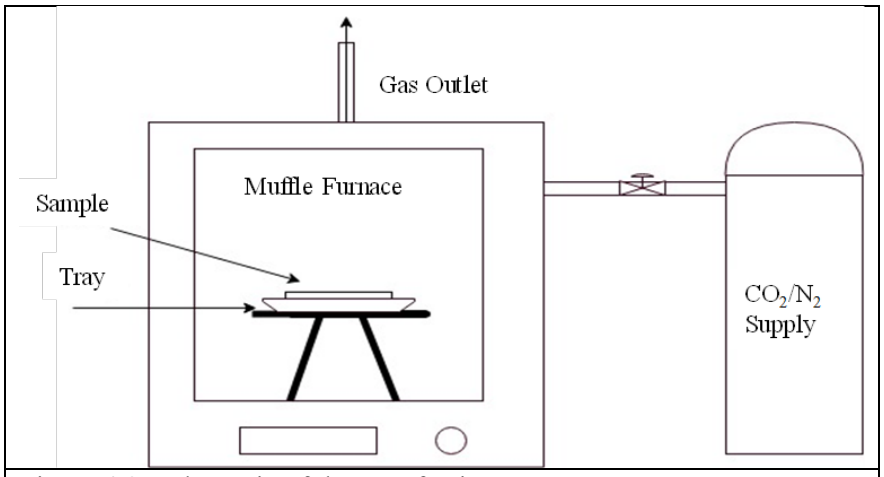

Figure 4.2. Schematic of the torrefaction system.

Modeling of heat-transfer-torrefaction reaction has been developed by Xu et al., under the same conditions of the current study, and has proven to fit the measured data rather accurately (Xu et al., 2018). The model shows the relationships for the temperature and mass loss transients. Eq. (4.1) is the temperature transient (*T(t)*),

$$T(t) = T_w - (T_w - T_o)e^{-t/\tau} \tag{4.1}$$

where T_w and T_o are the temperatures of furnace wall and initial temperature of the particle, respectively, t is time and τ is a characteristic time given by Eq. (4.2)

$$\tau = \frac{mc_p}{hA} \tag{4.2}$$

This can be measured from sample mass (m), heat capacity (c_p), heat transfer coefficient of the furnace walls to the sample (h), and the surface area of sample (A).

The ratio of the sample mass (at a given time) to the initial sample mass is presented by α, and the reaction was assumed to be the first-order reaction, and the reaction rate (R) was given by Eq. (4.3)

$$R = \rho \frac{d(\alpha)t}{dt} = -\rho k(\alpha)t \tag{4.3}$$

where $k(T)$ is a rate coefficient given by Eq. (4.4)

$$k(T) = \frac{A^{\dagger}}{\rho} e^{-T_a/T(t)} \tag{4.4}$$

where ρ and $A^{\dagger}$ are the density of the sample and pre-exponential factor, respectively. T_a is a characteristic temperature given by $T_a=E_a/R$ where E_a and R, are activation energy and the gas constant, respectively. Commonly, mass loss, 1-α, is used to define the extent of torrefaction, which is presented by Eq. (4.5)

$$1 - \alpha = 1 - e^{-\int_0^t k dt} \tag{4.5}$$

Eq. (4.1) and (4.2) enable us to calculate the temperature transient of a given sample in our furnace. By combining Eq. (4.3), (4.4) and fine-tuning the parameters T_a and $A^{\dagger}$, 1-α (measured mass loss) could fit the results of the experiments. This procedure has been applied successfully by Xu et al (Xu et al., 2018).

4.3.3. Densification by extrusion

This study examined the use of extrusion to densify the torrefied fiber-plastic blend. Samples of the torrefied/non-torrefied plastic-fiber waste blends (400 g each batch) were manually fed into an 18 mm co-rotating twin-screw extruder (Leistritz, L/D ratio of 40, 200 rpm, 4.7 kW motor, base torque 18%) and extruded into a rod (9 mm Ø) and cooled

by forced air (Adefisan Wei, & McDonald, 2017). The extruder is divided into 8 zones with temperature controllers. Extrusion parameters, as well as zone temperatures, are given in Table 4.1.

Table 4.1. Extrusion parameters

Torrefaction Mass loss (%)	Extruder barrel zones 2-5 temperature (°C)	Extruder barrel zones 6-8 temperature (°C)	Torque (%)	Die pressure (psi)
0	170	160	50	500-600
10.8	160	150	35	200-300
31.7	160	150	30	100-150
51	155	145	30	100

4.3.4. Characterization

4.3.4.1. Fourier-transform infrared spectroscopy (FTIR) characterization

FTIR spectral analysis was performed for (i) 30 pieces randomly chosen from plastic waste (ii) 30 pieces randomly chosen from fiber waste; (iii) 30 pieces randomly chosen from waste blend and (iv) sliced sections of extruded non-torrefied/ torrefied material with an FTIR spectrometer (Thermo-Scientific Nicolet-iS5), 64 scans, with an attenuated total reflectance accessory (ZnSe crystal, iD5). OMNIC v9.8 software and Aldrich, Hummel, and Nicolet spectral libraries were used to analyze the data. Carbonyl index (CI), cellulose index (CeI), and hydroxyl index (HI) were obtained as a ratio of the band intensity (absorbance) at 1720 cm^{-1}, 1024 cm^{-1}, and 3342 cm^{-1}, respectively, to the band 2916 cm^{-1} for the $-CH_2-$ groups (Wei, McDonald, Freitag, & Morrell. 2013).

4.3.4.2. Thermal analysis

Thermomechanical analysis (TMA) was performed with Perkin Elmer TMA 7 instrument on sliced discs (0.5 mm x 9 mm Ø) from the extruded rod using the penetration probe (static force 10 mN) from 30 to 200 ºC at 5 ºC/min. Data were analyzed using Pyris v8 software to determine the onset softening temperature. Dynamic mechanical analysis (DMA) was carried out in 3-point bending mode (15 mm span) on hot-pressed extruded rod samples (2 x 5.5 x 20 mm^3) using a Perkin Elmer DMA-7 instrument (1 Hz and 0.5 % strain) with refrigerated cooling from -50 to 120 ºC at a ramp rate of 3 ºC/min.

4.3.4.3. Rheology

Dynamic rheological measurements (G′, G″, and η*) were carried out on a Bohlin CVO 100 rheometer, using serrated parallel plates (25 mm Ø), in an oscillating mode with an extended temperature control module on pressed disc (3 mm × 25 mm Ø) samples. Experiments were performed in the linear viscoelastic region. Measurements were carried out at 180 °C in the frequency range of 0.01 to 100 Hz at an applied strain of 0.5% (Luo Cao, & McDonald, 2016). Data were analyzed using the Bohlin rheology v6.51 software.

4.3.4.4. Density

Weight divided by volume. The weight of the pellet was measured using a scale (A&D HR-60) with a readability of 0.0001 g. Since the surface of the extruded pellets was very smooth, cylinder-shaped pellets were cut from them to calculate cylinder volume. The diameter (*d*) and length of the cylinder (*l*) were measured using caliper (Fowler Electronic

Caliper) with a resolution of 0.01 mm. The density was obtained by calculating using the formula *mass/cylinder-volume.*

Volume displacement method. The dry weight of the pellet, m, was measured using a scale (A&D HR-60) with a readability of 0.0001 g. A 100 ml graduated cylinder partially filled with distilled water was prepared, and the reading V_o was recorded. The pellet was placed into water. The volume reading with immersed pellet, V, was recorded. The density was obtained by calculating the ratio $m/(V\text{-}V_o)$.

4.3.4.5. Flexural testing

The extruded rod samples (150 mm long) were hot-pressed (PHI hydraulic press, 300 x 300 mm^2) slowly at 140 ºC over 20 min to a thickness of 3.25 mm, then cooled to room temperature under load. The flattened material was cut into flexural specimens (3.25 x 16 x 60 mm^3). Three-point flexural tests (strength and modulus) were performed on the specimens (≥6 replicates) according to ASTM Standard D 790-07 with a crosshead speed of 1.31 mm/min, span of 52 mm, tested until specimen failure or 5% strain, whichever occurred first on an Instron 5500R-1132 universal test machine (5 kN load cell). Data were collected and processed using Bluehill v3 software (Instron).

4.3.4.6. Water absorption

The extruded sample was put into a vial and then filled with distilled water until the sample was fully submerged or the vial was full. The original weight was recorded, the sample after a certain period was taken out, surface water was removed, and the net weight

was measured. Water absorption is defined as the net weight of the sample over the original weight.

4.3.4.7. Size distribution analysis

For the size distribution analysis, 200g of pellets were ground for 120s. During grinding the motor power was monitored (by Watts Up pro power analyzer and data logger). Grinding was done, up to 1,800s, until grinding power stabilized at an asymptotic value (Xu et al., 2018). The ground sample was then moved to a sieve shaker (W.S Tyler, RX-86) with four screens (sizes of 150 µm, 250 µm, 425 µm, and 850 µm). The sieve shaker was operated for an hour to obtain five different fractions. Each fraction was weighted to determine the material size distribution after grinding.

4.3.4.8. Heat content

Previous experience has shown that the results of the material heat content have large variabilities if the sample was directly taken after grinding. This was due to the nature of the blend, as grinding generates particles of different sizes. To resolve this issue, the ground material was sifted into five different fractions (as discussed above). Each fraction from the size distribution was tested for heat content, measured using a bomb calorimeter (Parr 6100). For each measurement, a crucible containing ~1g of the sample was placed into a bomb filled with oxygen (~400 psi), and the bomb was submerged into a jacket filled with distilled water (2,000 g). The sample was ignited, and the heat released during the combustion was transferred to the water in the jacket. The heat content was calculated by

calorimeter by monitoring the temperature difference of the water in the jacket before and after the combustion. After a full analysis of all fractions from the sifting, a weighted average was calculated to determine the heat content of the sample.

4.3.4.9. Combustion test

The extruded rods with different mass losses were cut into equal dimension pellets (24.8 mm x 9.55 mm Ø, 2g) and were placed on a tared porcelain crucible (Fisher brand FB-965-G) then placed in a muffle furnace (Lindenberg/Blue type BF51828C-1) set at 900 °C. The experiments were done for different times starting from 1 min. After each experiment, the crucible was removed from the furnace and placed in the desiccator, the weight was recorded after it was cooled to room temperature. If there was more than 2 mg difference between the current and previous experiment, the crucible would be re-furnaced until the difference was less than 2 mg (ASTM D 5630-94).

4.4. Results and discussion

4.4.1. Torrefaction

Fiber and plastic wastes were torrefied separately and as a blend. Figure 4.3 shows photos of the original waste blend as well as selective torrefied material used for extrusion.

According to Eq. (4.2), the characteristic time for fiber, plastic and blend were $\tau_{fiber}=136$ (s), $\tau_{plastic}=300$ (s) and $\tau_{blend}=184$ (s), respectively. Figure 4.4 Top portrays temperature transients calculated by Eq. (4.1) for the fiber, plastic and the blend, reaching 300 ºC. The differences between the three transients arise from differences in the properties of the three materials, as summarized by Xu et al., (Xu et al., 2018). Figure 4.4 Bottom

shows measured mass loss for fiber, plastic, and blend torrefied at 300 ºC. For the three materials, mass loss remained zero for 4-5 min then it started to increase gradually. The figure also includes model results for each material and the expected model behavior of the blend. Experimental results for the mass loss for the plastic waste (square symbols) show a slow increase with time, whereas the measured results for the fiber waste (circle symbols) show a much faster increase of mass loss with time. Each of the mass loss transients was also modeled (dashed lines in Figure 4.4 Bottom), showing perfect fit to experimental data, as explained above (see Eq. (4.5)) and the kinetic parameters were drawn from the fitting process.

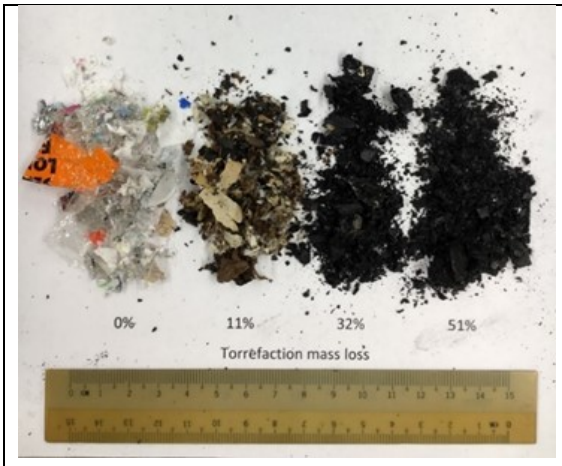

Figure 4.3. The photograph shows the original waste plastic mix and torrefied material at 11%, 32%, and 51 % mass loss.

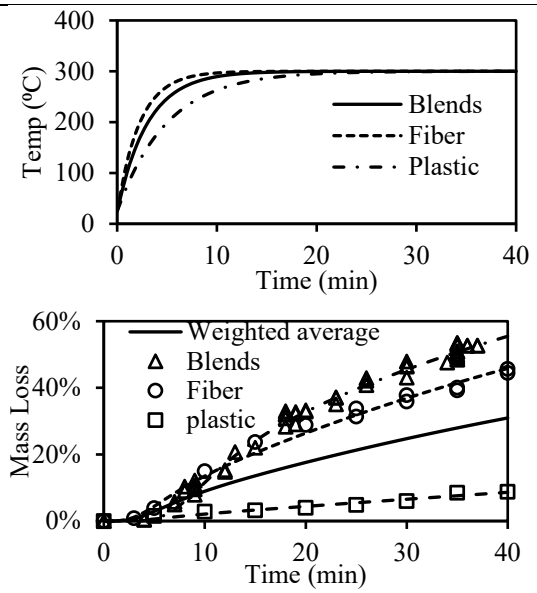

Figure 4.4. Top – temperature transients calculated by Eq. (4.1) for the fiber, plastic, and the blend, reaching 300 °C. Bottom – a mass loss for the fiber, plastic, and the blend. The figure also shows model results for each component and the expected model behavior for the blend.

The parameters obtained by the fitting as follows: (i) *fiber:* $(A^{\dagger}/\rho)_{fiber} = 2{,}997$ and $(T_a)_{fiber} = 5{,}369\ (K)$, (ii) plastic: $(A^{\dagger}/\rho)_{plastic} = 2{,}558$ and $(T_a)_{plastic} = 6{,}383\ (K)$, *and* (iii) blend: $(A^{\dagger}/\rho)_{blend} = 1.2*10^{8}$ and $(T_a)_{blend} = 15{,}258\ (K)$. The important point is that these kinetic parameters were used to predict the mass loss behavior for the plastic-fiber waste blend, assuming each component does not influence the other. In this case, evidently, the resultant behavior should have been between the fiber and plastic transients, as shown by the solid line in the figure. However, the actual experimental data for the blend show much faster mass loss transients (triangle symbols) than expected. This is direct evidence that there is a strong reaction (synergy) between the fiber (mostly cellulose polymers) and the plastic material (mostly hydrocarbon polymers).

Although at this stage we did not carry out solid-state characterization measurements that might shed direct light on the reactions between the two polymers, it can be hypothesized that hydrogen atoms from the hydrocarbon polymer react with either, COOH, CO or OH groups in the cellulosic polymer and enhance the stripping of these groups, thus increasing the reaction rate of the degradation of the cellulosic polymer. Similar behavior was observed by Nallar and Wong, where the existence of high-density polyethylene accelerated the thermal degradation of the cellulose (Nallar & Wong, 2019).

4.4.1. Extruded pellets

Samples of a non-torrefied waste blend (0% mass loss) and torrefied waste blend (11%, 32%, and 51% mass loss) were compounded and extruded into rods (Figure 4.5). Compounding homogenized both the non-torrefied and torrefied materials into a uniform extrudate. The addition of the plastic in the feedstock has enabled the extrusion process

because the high temperature melted the plastic which in turn acted as a lubricant. The molten plastic encapsulated the fiber to form a consistent/uniform extruded rod. The extruder barrel temperature was decreased by at least 10 ºC for the torrefied material than the original waste blend (Table 4.1) to minimize surface cracking. The smoothness of the extrudate surface depended strongly on the die temperature that had to be adjusted to get the desired surface quality.

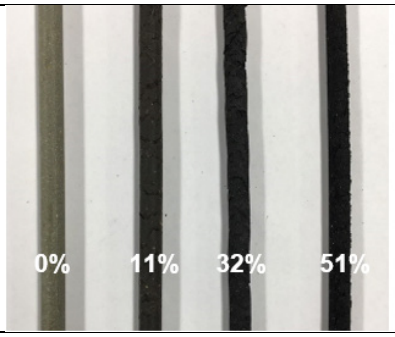

Figure 4.5. Photograph showing the extruded rods made from a non-torrefied waste blend (0% mass loss) and torrefied materials at 11%, 32%, and 51% mass loss.

4.4.2. FTIR spectroscopy

Despite the differences in the relative standard deviations, important information regarding the material in the blend can be obtained. FTIR spectroscopy was employed to examine the major chemical changes that occurred in the waste blend samples upon torrefaction (Balogun, Sotoudehniakarani, & McDonald, 2017). FTIR measurements were performed on samples prior to and after the torrefaction. Details on FTIR measurements and consequent conclusions regarding the chemical changes during torrefaction are given below.

The feedstock used was a blend of 40% plastic and 60% fiber wastes. FTIR experiments were done 30 times for both fiber waste (Figure 4.1a) and plastic waste (Figure

4.1b) to determine the chemical identity prior to the blending. Figure 4.6a showed that plastic wastes mainly consist of low-density polyethylene, polyethylene, polyethylene terephthalate, polyamide nylon, polyvinyl, polypropylene, and some other materials. Figure 4.6b showed that there are silopren, polyester with kaolin filler, and acrylate/paper mix together with cellophane/cellulose in the fiber wastes. The results from Figure 4.6 indicated the large variabilities in the feedstock.

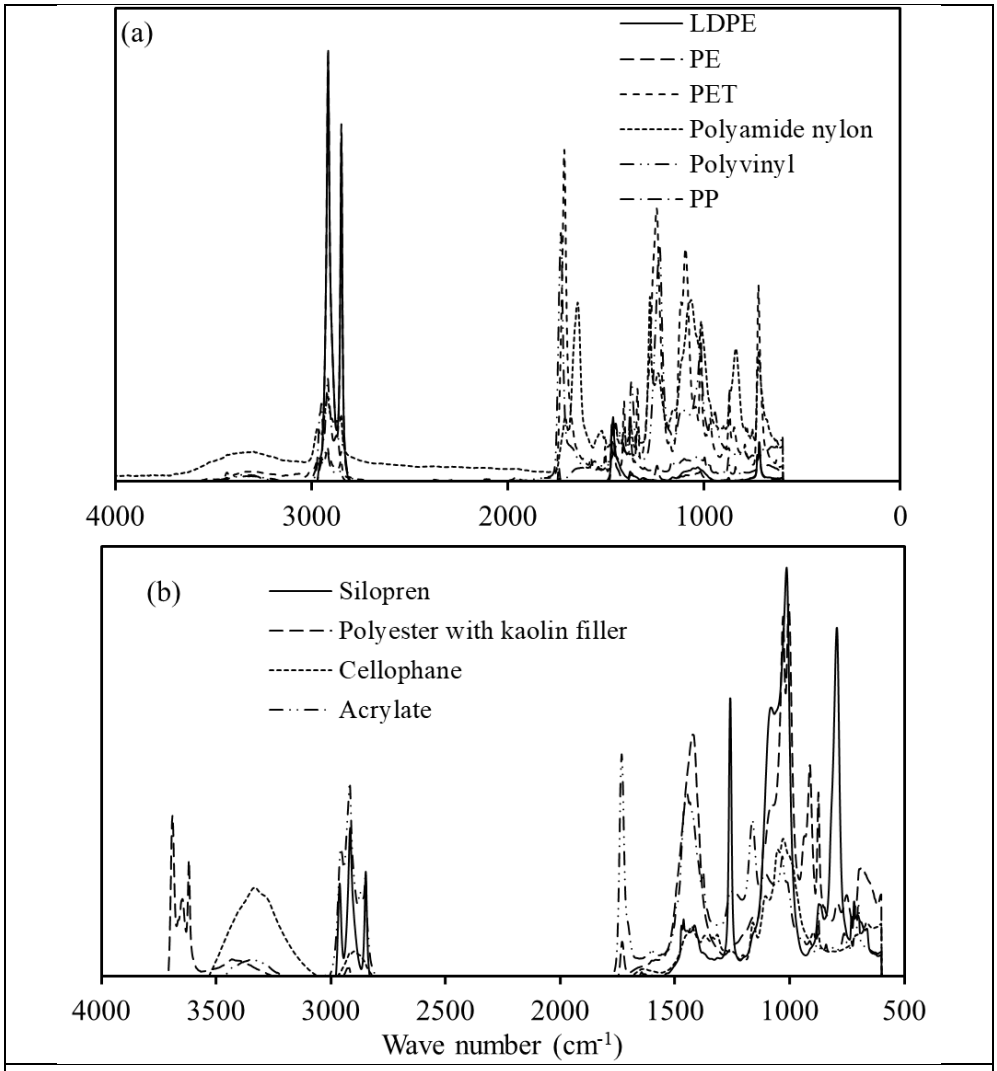

Figure 4.6. Materials identified from raw feedstock, (a) plastics; (b) fibers.

Figure 4.7 shows FTIR spectra of a composite average of 30 waste blend pieces, extruded mixed plastic waste (0 % mass loss) and extruded torrefied (11 %, 32 %, and 51 % mass loss) material. C -H stretching bands were observed in every sample and were attributed to methyl (2960 cm^{-1} and 2870 cm^{-1}) and methylene (2916 cm^{-1} and 2850 cm^{-1}) groups (Mayo, 2004). The two methylene bands were of comparable intensity for all samples and the methyl group decreased with the extent of torrefaction. It was observed that there exists O-H stretching band in all the samples at the region between 3100 and 3600 cm^{-1} and the intensity gradually reduced as mass loss increased. At 1690-1750 cm^{-1}, a broad carbonyl (C=O) band was detected mainly assigned to (i) an ester in linkage in PET and acrylate, and (ii) amide linkage in nylon (Mayo, 2003). Paper was recognized due to a small band at 1505 cm^{-1}. Wood cellulose and hemicellulose were also identified at the region at 1000-1070 cm^{-1} (Pandey, 1999). *Cis*- band at 727 cm^{-1} and *trans*-vinylene bands at 974 cm^{-1} were found in all the samples (Miller, 2003).

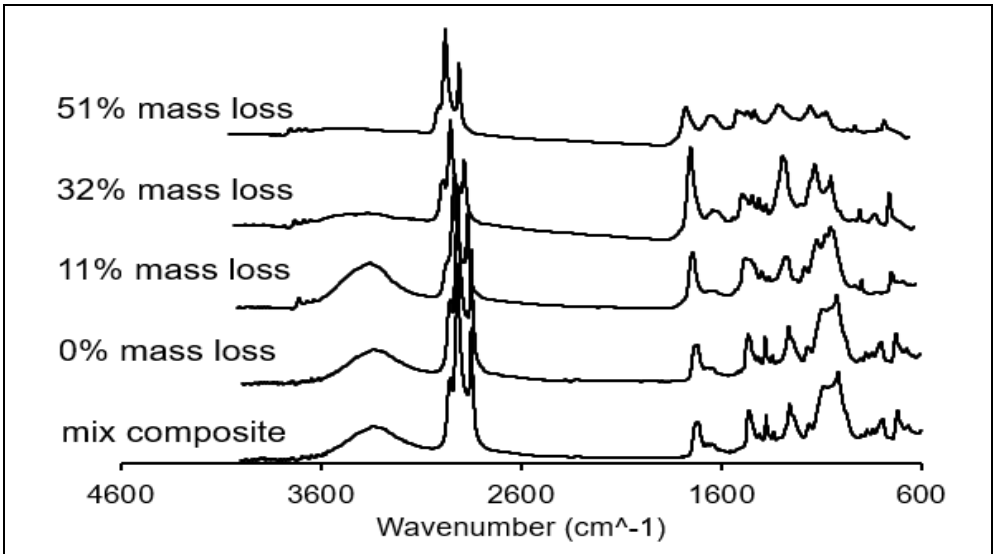

Figure 4.7. FTIR spectra of a composite average of 30 waste blend pieces, extruded mixed plastic waste (0 % mass loss) and extruded torrefied (11 %, 32 %, and 51 % mass loss) material

The relative changes in hydroxyl, carbonyl, and cellulose that occurred during torrefaction were analyzed by calculating HI, CI, and CeI, respectively (Figure 4.8). The HI and CeI decreased respectively from 0.27 to 0.02 and from 0.51 to 0.20 upon torrefaction (0 % to 51 % mass loss). These results support that the reduction in cellulose content was due to dehydration and degradation reactions (Wang et al. 2014). The CI increased from 0.26 to 0.34 at 32 % mass loss then decreased to 0.21 at 51 % mass loss and this change could not be explained.

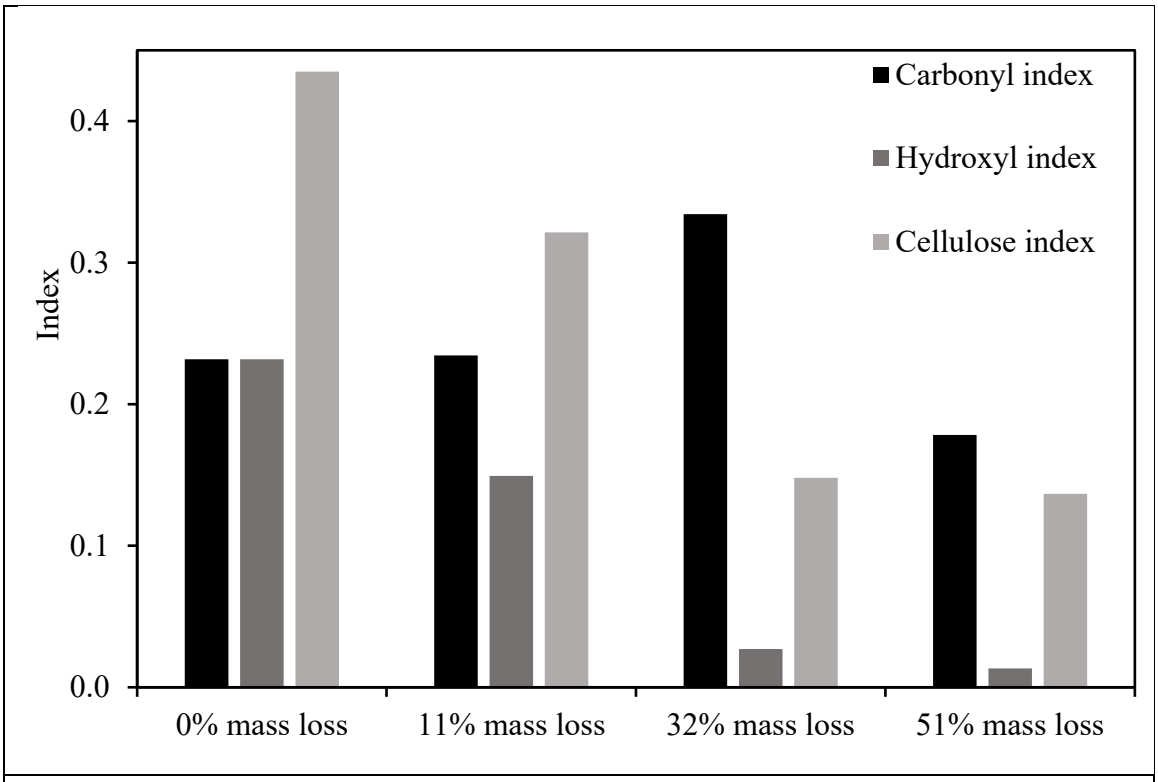

Figure 4.8. Plot showing changes in hydroxyl (HI), carbonyl (CI) and cellulose (CeI) indices with the extent of torrefaction (mass loss).

4.4.3. Material variability and homogeneity

FTIR spectroscopy shows that there exist large variabilities in the raw feedstock (Figure 4.6). Perhaps one of the most important roles of extrusion and torrefaction of

samples containing plastic is the ability to significantly reduce the heterogeneity of the initial waste blend. To note, heterogeneity (or non-uniformity) was defined by the term standard deviation/intensity (STD/In) of the 30 IR spectra measured –larger the term the greater is the heterogeneity of the blend. Figure 4.9 shows the normalized heterogeneity for the various samples: from left to right is the original fiber-plastic blend, followed by same blend that was extruded, which reduced the heterogeneity by ~70%, followed by the 10% mass loss blend, which reduced another 10% of heterogeneity and the number finally stabilized at ~15% after the mass loss reached 32%. The combination of torrefaction followed by the extrusion process decreased the heterogeneity of the original blend by a factor of 7. This indicated that the extrusion process reduced the variabilities of the material since the plastics were melted and the feedstock was well-mixed inside the reactor before getting extruded.

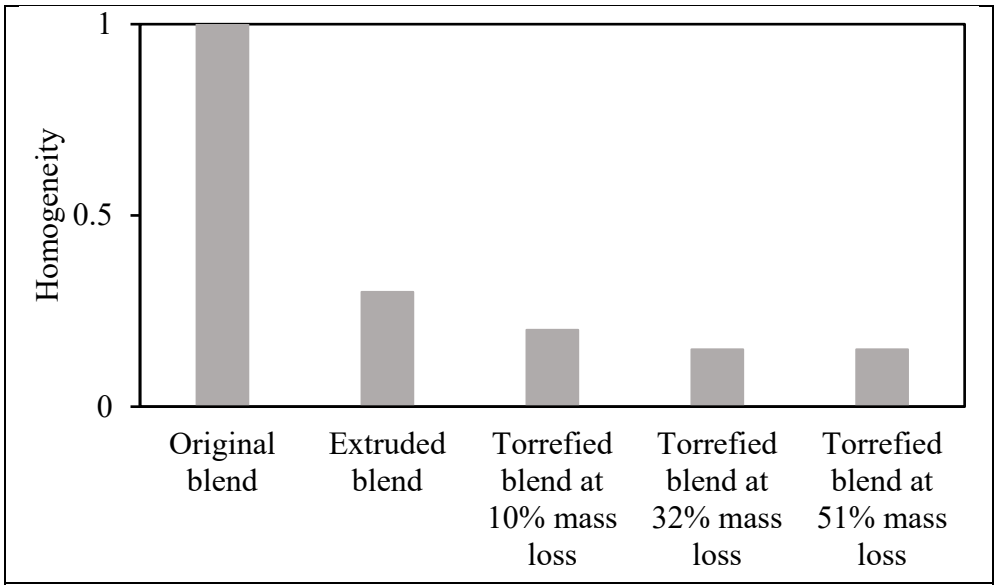

Figure 4.9. Heterogeneity as defined by STD/IN of IR spectra measured.

4.4.4. Thermomechanical analysis (TMA)

TMA was performed on the extruded torrefied material to determine the materials' softening point (Figure 4.10).

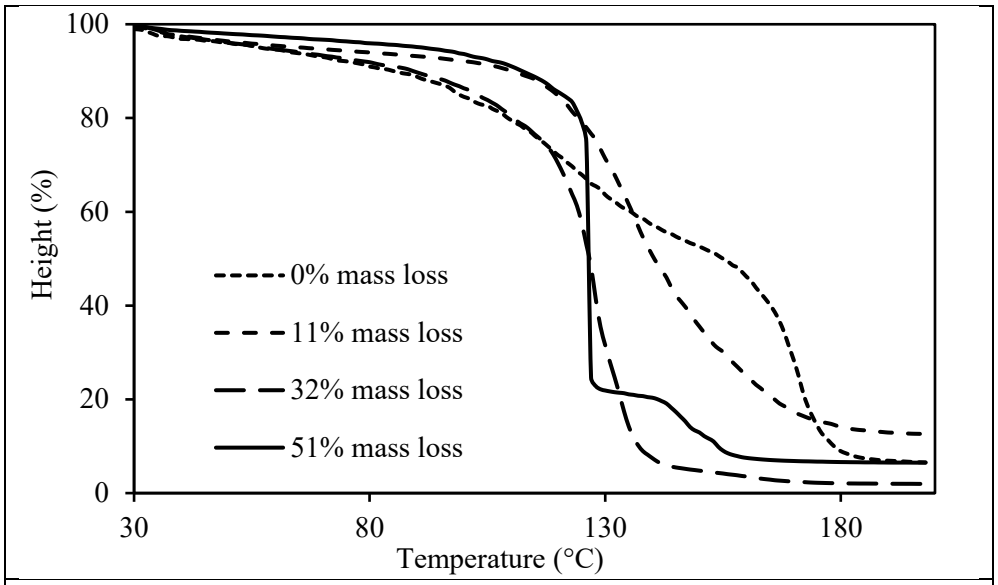

Figure 4.10. TMA thermograms of the extruded torrefied (0% to 51% mass loss) samples

Table 4.2 shows the softening temperature (T_s) onset for the extruded torrefied materials. The waste blend was shown to have two, gradual, softening temperatures (T_{s-1} and T_{s-2}) at 102 ºC and 164 ºC and these coincide with the melting temperatures of low-density polyethylene (LDPE) (98-115 ºC) and polypropylene (160-175 ºC) (Harper, 1999). The gradual change in probe height during the thermal transition is likely due to the reinforcing effect of cellulose/paper in the sample. As the waste blend was torrefied (11% mass loss), T_{s-1} increased slightly to 120 ºf then progressively decreased to 109 ˚C (51% mass loss). Furthermore, the 51% mass loss torrefied material had two other transitions (T_{s-2} and T_{s-3}) at 123 ºC (sharp) and 142 ºC.

Table 4.2. Softening temperatures for the extruded material determined by TMA.				
Torrefied material	0% mass loss	11% mass loss	32% mass loss	51% mass loss
T_{s-1} (°C)	102	120	112	109
T_{s-2} (°C)	164	NA	NA	123
T_{s-3} (°C)	NA	NA	NA	142

4.4.5. Dynamic rheological results

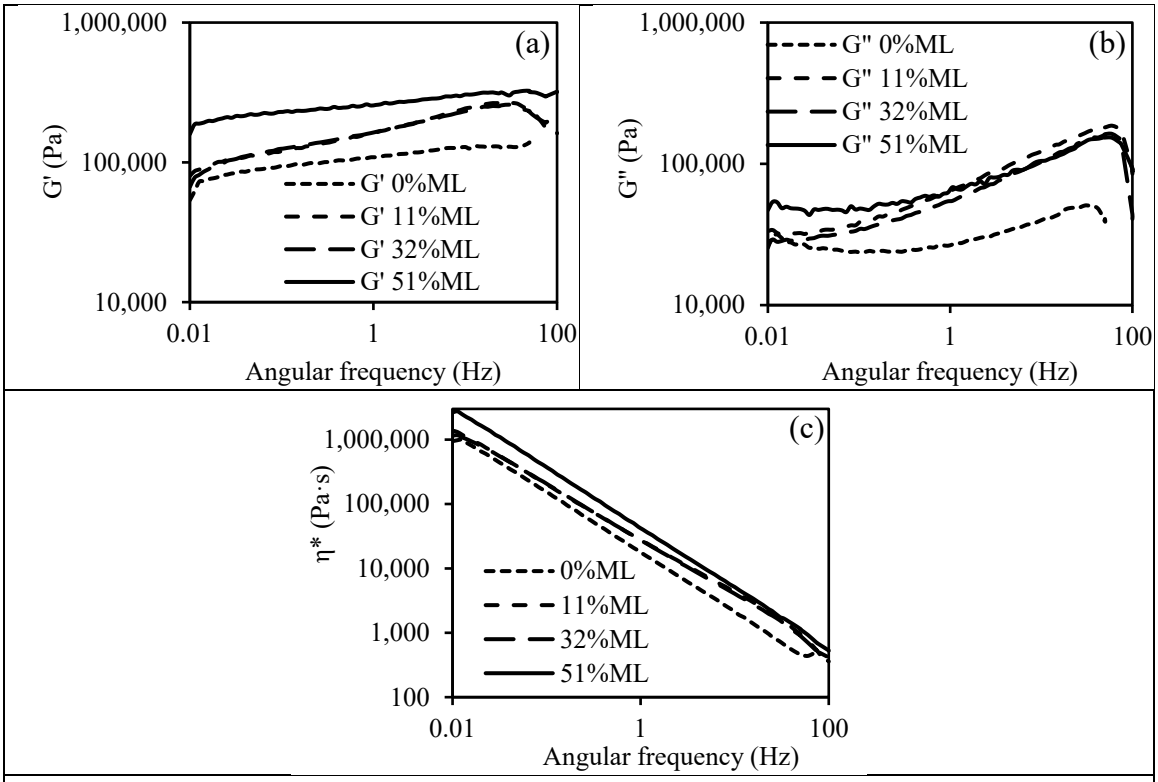

Figure 4.11. Dynamic rheology showing (a) elastic moduli (G'), (b) viscous moduli (G") and (c) complex viscosity (η*) as a function of frequency for torrefied waste blend extrudates at 180 °C.

Dynamic rheological measurements were also obtained on the extruded torrefied melts. Figure 4.11 shows the dynamic elastic (G') and viscous (G") moduli and complex viscosity (η*) as a function of frequency at 180 °C. For all melt samples G' and G" were shown to increase with angular frequency (Figure 4.11a and 11b). Torrefaction of the waste blend to 51% mass loss was shown to increase both G' and G" >2-fold (at 1 Hz). Over the

angular frequency range examined, the G' was higher than G", indicating an elastic response predominated at 180 ºC. The η* was shown to decrease with an increase in angular frequency, showing a shear-thinning behavior for the melts and this trend has been observed in reprocessed mixed plastic wastes (Hamad, Kaseem, & Deri, 2013) (Figure 4.11c). The η^* (at 1 Hz) was also shown to increase from 16,800 Pa·s for the waste blend extrudate to 40,000 Pa·s for the 51% mass loss torrefied extrudate.

4.4.6. Density and mechanical properties

Table 4.3. Density, flexural, and viscoelastic properties of extruded torrefied (0 to 51% mass loss) material.

	0% mass loss	11% mass loss	32% mass loss	51% mass loss
Density* (kg/m^3)	1142 (36)	1082 (21)	1134 (30)	1189 (48)
Density**(kg/m^3)	1124	1087	1144	1191
Flexural modulus (MPa)	1,400 (98)	1,500 (106)	1,404 (82)	1,354 (53)
Flexural strength (MPa)	10.67 (0.77)	8.23 (0.53)	10.94 (0.63)	7.66 (1.22)
Storage modulus E' (MPa) at 20 ºC	389	467	507	670
Tan δ at 20 ºC	0.069	0.068	0.086	0.103
Temperature at max loss modulus E" (ºC)	94	77	59	53

*determined by volume displacement method; **determined by weight divided by volume; Standard Deviation in parentheses.

The density (volume displacement method) of the extruded torrefied rod samples ranged between 1082 to 1189 kg/m^3. The density determined by weight/volume gave comparable values. Results are summarized in Table 4.3.

The results of the flexural tests on the extruded torrefied material are shown in Table 4.3. The mean flexural modulus for the extruded torrefied samples (0 to 51% mass

loss) was between 1,354 and 1,500 MPa. The modulus for the 51% mass loss torrefied material was significantly lower than the other 3 samples. The modulus of these materials was comparable to polypropylene (1,170-1,720 MPa) (Shah, 1998). The mean flexural strength for the extruded torrefied samples (0 to 51% mass loss) was between 7.66 MPa and 10.94 MPa and similar to LDPE (12 MPa) (Kormin, Kormin, Beg, & Piah. 2017). The 0% and 32% mass loss extruded torrefied material was significantly stronger than the 11% and 51% mass loss samples.

DMA analysis was performed on the extruded material (Figure 4.12). The storage modulus (E'), tan δ values at 20 ºC, and temperature at maximum loss modulus (E") of the extruded torrefied material values are given in Table 4.3. The 51% mass loss material had the highest E' value at 670 MPa while the mix plastic waste (0% mass loss) had the lowest at 389 MPa. A similar trend has been found existing on natural fiber polypropylene composites (Tajvidi, Falk, & Hermanson, 2006). This might be due to the lower fiber content at a higher mass loss, while the reinforcement imparted by the fiber could allow stress transfer from the matrix to the fiber (Rana, Mitra, & Banerjee, 1999). Additionally, with an increase in torrefaction mass loss, the temperature at maximum loss modulus showed a shift to a lower value (Jacob & Isac, 2017).

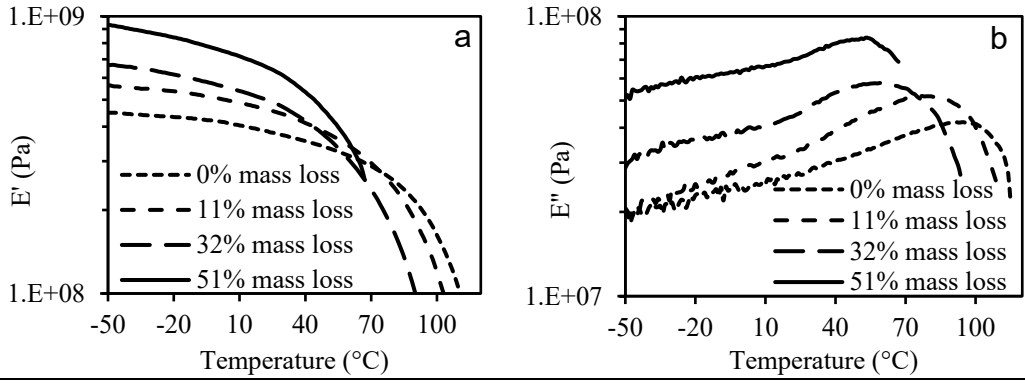

Figure 4.12. (a) storage modulus (E') and (b) loss modulus (E")

4.4.7. Water resistance

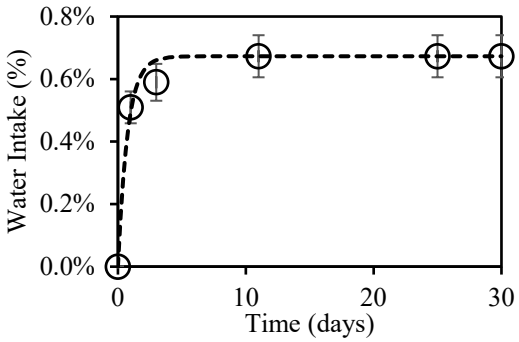

Figure 4.13. Water intake of extruded, 20% mass loss, torrefied material as a function in time.

A sample of torrefied (20% mass loss) and extruded material was used in the water absorption experiment. Four samples were submerged in water for 30 days. Samples were taken out for water intake measurements after 1,3,11,25 and 30 days (Figure 4.13). Surface water was removed, and the weight of the sample was taken. Material disintegration was not observed. The results are given in Figure 4.13, showing water intake (as the weight difference, in percent) reached an asymptotic value after 5 days to 0.7%, indicating that these extruded pellets did not absorb water. This can be attributed to the plastic melted around the fiber. This creates a protective layer that prevents water absorption. In addition, it can be hypothesized that the protective layer prevents oxygen from accessing the active sites created by the degradation of the cellulosic polymers.

4.4.8. Size distribution

As shown by Xu et al., the fractions above and below 850 μm represent the changes in the material structure (physical and structural) as the mass loss increases (Xu et al.,

2018). Figure 4.14 shows the size distribution of the extruded torrefied pellets with 0% 11%, 32%, and 51% mass loss. It was clear that after grinding, the size fraction below 850 µm went up as mass loss increased and it almost reached 100% at 51% mass loss, and size fraction above 850 µm went down accordingly.

4.4.9. Heat content

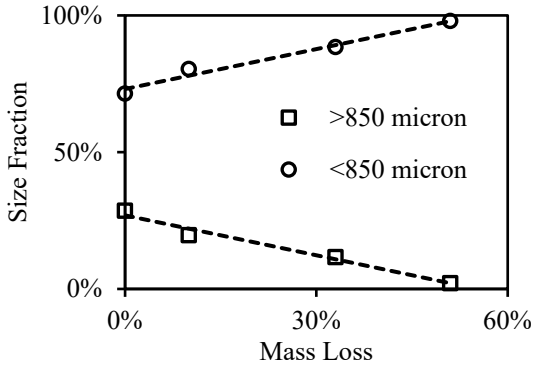

Figure 4.14. Size fractions of the extruded pellets after grinding

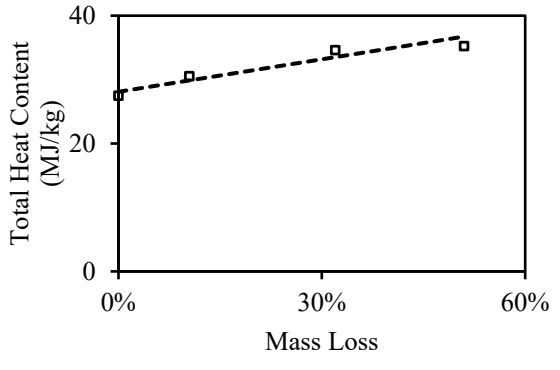

Figure 4.15. The total heat content of the extruded pellets at a different mass loss

To avoid sampling issues the material was ground and sifted to 5 different fractions. The heat content of fractions was measured, and the total heat content was calculated based on the weighted average. Figure 4.15 showed the heat content for the pellets with the function of mass loss. The heat content increased from 28.1 MJ/kg to 35.2 MJ/kg as the mass loss increased to 51%.

4.4.10. Combustion test

The extruded pellets produced can be burned as is in stokers, moving grates and other boilers (Taulbee et al., 2010) without grinding. In this case, it is essential to study the combustion behavior of the pellets. When the pellets are heated up, the volatile matter is

first released and burned in the gas phase at a fast rate, then the fixed carbon burns at a much slower rate; this behavior is comparable to that of biomass and coal combustion.

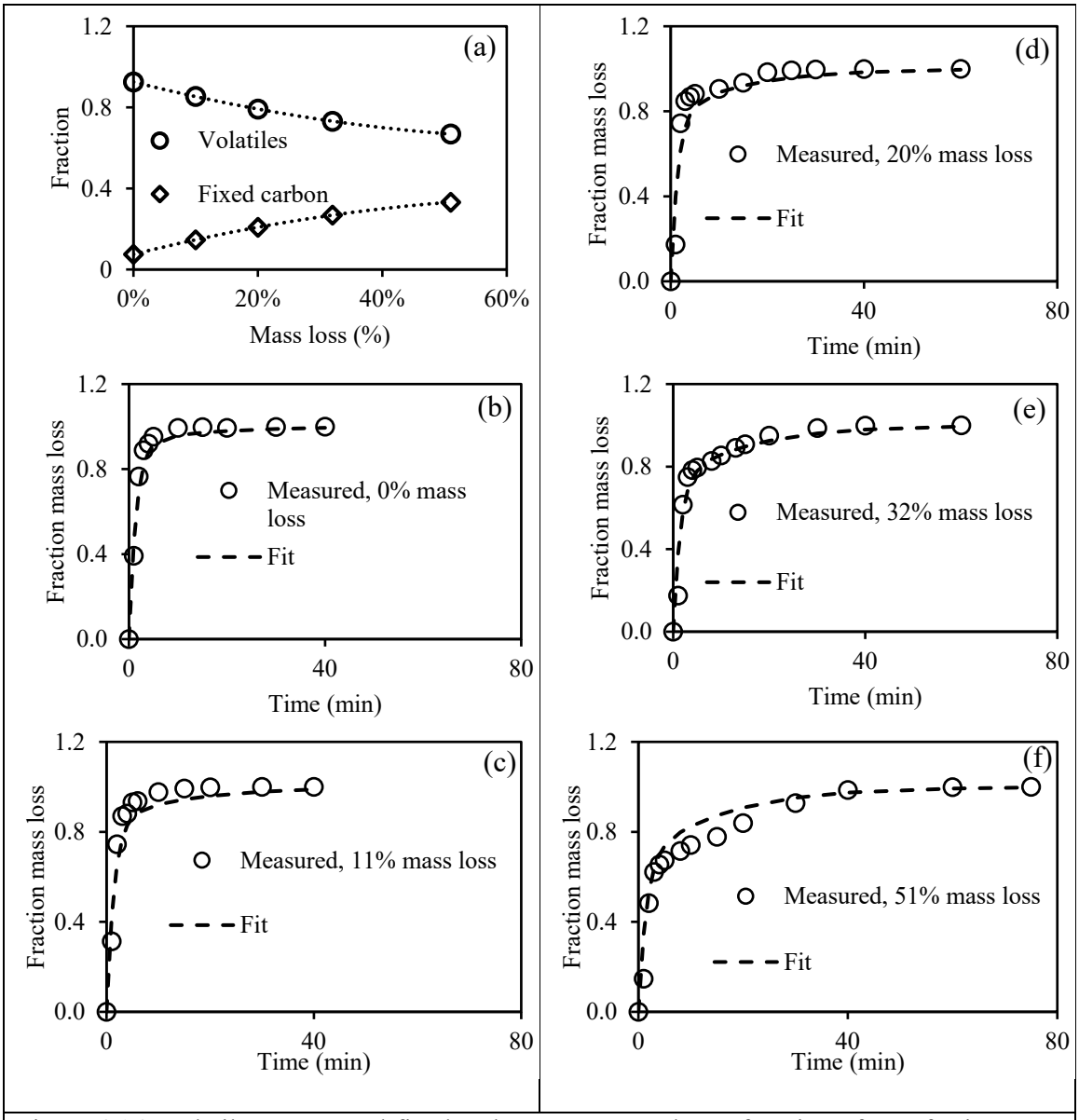

Figure 4.16. Volatile content and fixed carbon as measured as a function of torrefaction mass loss (a). Combustion tests plotted as mass loss fraction vs time for non-torrefied pellets (b), torrefied pellets at 11-51% mass loss (c-f).

The two-stage combustion behavior is expected to behave according to the following equation $\alpha = a_1\left(1 - e^{-\frac{t}{\tau_1}}\right) + a_2\left(1 - e^{-\frac{t}{\tau_2}}\right)$ where α is the fraction of the burned material (pellet), a_1 and a_2 are the fraction of volatile and fixed carbon, respectively. The characteristic times τ_1 and τ_2 represent the volatile burning and fixed carbon burning, respectively. The values of a_1 (Twin Port Testing, 2019) and a_2 were measured for each mass loss. The values τ_1 and τ_2 were fitted from experimental data and were kept identical in all the cases (all the mass loss values). Figure 4.16a shows measured volatile content and fixed carbon as a function of mass loss. It has shown that the volatile matter of the material decreases with the extent of torrefaction, and the fixed carbon increases accordingly. Figure 4.16b-f show combustion test results, plotted as mass loss fraction vs. time, for non-torrefied pellets (Figure 4.16b) and for torrefied pellets with mass losses in the rage of 10-51% (Figure 4.16c-f). The characteristic times for the volatile matter was found to be 1.49 min and 15.62 min, respectively. It is to be noted that these results are for the specific pellet configurations; i.e. if we take the external surface (8.89 cm^2) into consideration as a linear parameter, we will get 0.17 min/cm^2 and 1.76 min/cm^2.

4.5. Conclusions

In this study, waste blends consisting of 40% plastic and 60% fiber at different mass losses were used as the feedstock for the extrusion, and the extruded products were characterized. The FTIR results showed that the fiber to plastic ratio decreased as the mass loss increased, and the extrusion process significantly increased the homogeneities of the feedstock, additionally, the torrefaction also further reduced the variabilities of the

material. Chemical changes (carbonyl, hydroxyl, and cellulose index) also showed that cellulose content reduced due to the dehydration and degradation reactions. Further, these reactions increased the heat content of the material and broke the fiber structure allowing grinding to be more effective. At 51% mass loss, close to 100% of the material was below 850 microns after grinding. As mass loss increased, the temperature at maximum loss modulus, showed a slight shift to a lower value. The dynamic rheological results also showed that the elastic response was predominated at 180 °C, and the melts of the material have a shear thinning behavior which was also observed in reprocessed mixed plastic wastes. It has shown that the volatile matter of the material decreases with the extent of torrefaction, and the fixed carbon increases accordingly. The plastic in the feedstock acted as a process enabler as it imparted properties like bindability, water resistance, high heat content and increasing the reaction rate of the degradation. Overall, the extruded pellets could be a drop-in fuel for small-to-large power plant facilities and reduce the amount of waste going to landfills.

4.6. References

Adefisan, O.O., Wei, L., & McDonald, A.G. (2017) Evaluation of plastic composites made with Laccosperma secundiflorum and Eremospatha macrocarpa canes. *Maderas Ciencia tecnologia.* 19(4): 517-524.

Arias, B., Pevida, C., Fermoso, J., Plaza, M. G., Rubiera, F., & Pis, J. J. (2008). Influence of torrefaction on grindability and reactivity of biomass. *Fuel Processing Technology*, 89(2), 169-175.

ASTM international (ASTM D 790-07). 2008. Standard test method for flexural properties of unreinforced and reinforced plastics and electrical insulating materials. *In Annual book of ASTM standards. Vol 08(01*). West Conshohocken, PA.

ASTM international (ASTM D 5630-13). 2001. Standard test method for ash content in plastics. *In Annual book of ASTM standards*, *Vol 08.03*. West Conshohocken, PA.

Ayomoh, M. K. O., Oke, S. A., Adedeji, W. O., & Charles-Owaba, O. E. (2008). An approach to tackling the env. and health impacts of MSW disposal in developing countries. *Journal of Environmental Management*, 88(1), 108-114.

Balogun, A., Sotoudehniakarani, F., & McDonald, A.G. (2017). Thermo-kinetic, spectroscopic study of brewer's spent grains and characterization of their pyrolysis products. *Journal of Analytical and Applied Pyrolysis*. 127: 8-16. https://doi.org/10.1016/j.jaap.2017.09.009.

Bar-Ziv, E., & Klinger, J. (2016). Logistics and storage of torrefied biomass Safety aspects, Safety Consideration in Biomass Torrefaction. *Energy-Tech Magazine*, Online, October 2016. Retrieved from http://www.energy-tech.com/fuels/.

Ceballos, D. C. C., Hawboldt, K., & Hellleur, R. (2015). Effect of production conditions on self-heating propensity of torrefied sawmill residues. *Fuel*, 160, 227-237.

China Daily. (2018). "China announces import ban on 32 types of solid waste". Retrieved from www.chinadaily.com.cn/a/201804/19/WS5ad83620a3105cdcf65194db.html.

Donepudi, Y. (2017) Impact of pretreatment methods on fast pyrolysis of biomass. [dissertation]. [Houghton (MI)]: Michigan Technological University

El-Fadel, M., Findikakis, A. N., & Leckie, J. O. (1997). Environmental impacts of solid waste landfilling. *Journal of Environmental Management*, *50*(1), 1-25.

US-EPA, Environmental Protection Agency. (2014) "Carbon Pollution Emission Guidelines for Existing Stationary Sources: Electric Utility Generating Units." Federal Register.

US-EPA, Environmental Protection Agency. (2015) Carbon pollution emission guidelines for existing stationary sources: electric utility generation units, EPA-HQ-OAR-2013-0602, pp1560.

Faix, O. (1992) Fourier transform infrared spectroscopy. In: Lin SY, Dence CW, editors. Methods in lignin chemistry. (pp. 83-132). Berlin: Springer-Verlag.

Harper, C.A. (1999) *Modern Plastics Handbook: Modern Plastics*. (pp. C41-C49). McGraw-Hill. N.Y.

Hamad, K., Kaseem, M., & Deri, F. (2013) Recycling of waste from polymer materials: An overview of the recent works. *Polymer Degradation and Stability*. 98: 2801-2812.

Hanaffi Mohd Fuad, M. A., Faizal, H. M., Rahman, M. R. A., & Latiff, Z. A. (2018). Torrefaction of densified empty fruit bunches with addition of plastics waste. *Biofuels*, 1-11.

Iroba, K.L., Baik, O.D., & Tabil, L.G. (2017). Torrefaction of biomass from municipal solid waste fractions I: Temperature profiles, moisture content, energy consumption, mass yield, and thermochemical properties. *Biomass and Bioenergy*, *105*, 320-330.

Iroba, K.L., Baik, O.D., & Tabil, L.G. (2017). Torrefaction of biomass from municipal solid waste fractions II: Grindability characteristics, higher heating value, pelletability and moisture adsorption. *Biomass and Bioenergy*, *106*, 8-20.

Jacob, R., & Isac, J. (2017). Dynamic mechanical analysis and thermal degradation of jute fiber reinforced BSFT (Ba0. 6Sr0. 4FexTi (1-x) O3-δ), (x= 0.1)-polypropylene composite. *Indian Journal of Pure & Applied Physics (IJPAP)*, *55*(7), 497-502.

Kiel, J. (2011). Torrefaction for upgrading biomass into commodity fuel. In *Status and ECN Technology Development. EUBIONET III Workshop, Espoo, Finland* (Vol. 15).

Klinger, J., Bar-Ziv, E., & Shonnard, D. (2015). Unified kinetic model for torrefaction–pyrolysis. *Fuel Processing Technology*, *138*, 175-183.

Klinger, J., Klemetsrud, B., Bar-Ziv, E., & Shonnard, D. (2014). Temperature dependence of aspen torrefaction kinetics. *Journal of Analytical and Applied Pyrolysis*, *110*, 424-429.

Kormin S., Kormin, F., Beg, M.D.H., & Piah, M.B.M. (2017) Physical and mechanical properties of LDPE incorporated with different starch sources. IOP Conf. Series: Materials Science and Engineering 226: 1-9. DOI:10.1088/1757-899X/226/1/012157.

Kumar, L., Koukoulas, A.A., Mani, S., & Satyavolu, J. (2017). Integrating Torrefaction in the Wood Pellet Industry: A Critical Review. *Energy Fuels*, 31, 37-54.

Luo, S., Cao, J., & McDonald, A. G. (2016). Interfacial improvements in a green biopolymer alloy of poly (3-hydroxybutyrate-co-3-hydroxyvalerate) and lignin via in situ reactive extrusion. *ACS Sustainable Chemistry & Engineering*, *4*(6), 3465-3476.

Mayo, D.W., Miller, F. A., & Hannah, R. W. (2004). *Course notes on the interpretation of infrared and Raman spectra*. (pp 33-72). New York: Wiley-Interscience.

Mayo, D.W. (2003). Spectra of carbonyl compounds of all kinds (factors affecting carbonyl group frequencies). In *Course notes on the interpretation of infrared and Raman spectra*. (pp. 199-224). John Wiley & Sons, Inc. Hoboken, New Jersey.

Miller, F.A. (2003). Characteristic frequencies of alkenes (olefins). *Course Notes on the Interpretation of Infrared and Raman Spectra.* (pp. 73-84). John Wiley & Sons, New York.

Nallar, M., & Wong, H. W. (2019). Enhanced Levoglucosan Yields from the Co-pyrolysis of Cellulose and High-Density Polyethylene. *ACS Sustainable Chemistry & Engineering*.

Nunes, L. J. R., Matias, J. C. O., & Catalão, J. P. S. (2014). A review on torrefied biomass pellets as a sustainable alternative to coal in power generation. *Renewable and Sustainable Energy Reviews*, *40*, 153-160.

Pandey, K.K. (1999) A study of chemical structure of soft and hardwood and wood polymers by FTIR spectroscopy. *Journal of Applied Polymer Science*. 71: 1969–75.

Park, J., Meng, J., Lim, K. H., Rojas, O. J., & Park, S. (2013). Transformation of lignocellulosic biomass during torrefaction. *Journal of Analytical and Applied Pyrolysis*, *100*, 199-206.

Radics, R.I., Gonzales, R., Bilek, E.M., & Kelley, S.S. (2017). Systematic Review of Torrefied Wood Economics. *BioResources* 12 (3), 6868-6886.

Rana, A. K., Mitra, B. C., & Banerjee, A. N. (1999). Short jute fiber-reinforced polypropylene composites: Dynamic mechanical study. *Journal of Applied Polymer Science*, *71*(4), 531-539.

Stelte, W., Bar-Ziv, E., & Klinger, J. (2016). Logistics and storage of torrefied biomass Safety aspects, Safety Consideration in Biomass Torrefaction. *Energy-Tech Magazine*, Online, October 2016. Retrieved from http://www.energy-tech.com/fuels/.

Stelte, W., Sanadi, A. R., Shang, L., Holm, J. K., Ahrenfeldt, J., & Henriksen, U. B. (2012). Recent developments in biomass pelletization–A review. *BioResources*, *7*(3), 4451-4490.

Shah, V (1998). *In* Handbook of Plastics Testing Technology, 2nd Ed (pp. 509). Wiley Interscience, NY.

Tajvidi, M., Falk, R. H., & Hermanson, J. C. (2006). Effect of natural fibers on thermal and mechanical properties of natural fiber polypropylene composites studied by dynamic mechanical analysis. *Journal of Applied Polymer Science*, *101*(6), 4341-4349.

Taulbee, D., Neathery, J., Patil, D., Sowder, N., O'Daniel, B., & Montross, M. (2010). Combustion of Briquettes and Fuels Pellets Prepared from Blends of Biomass and Fine Coal. In *International Coal Preparation Congress 2010 Conference Proceedings* (pp. 161-170). SME.

Tsalidis, G. A., Joshi, Y., Korevaar, G., & de Jong, W. (2014). Life cycle assessment of direct co-firing of torrefied and/or pelletised woody biomass with coal in The Netherlands. *Journal of Cleaner Production*, *81*, 168-177.

Tumuluru, J. S., Wright, C. T., Hess, J. R., & Kenney, K. L. (2011). A review of biomass densification systems to develop uniform feedstock commodities for bioenergy application. *Biofuels, Bioproducts and Biorefining*, *5*(6), 683-707.

Twin Port Testing. (2019, Feb 26). Retrieved from https://www.twinportstesting.com/.

US-EIA, U.S. Energy Information Administration, based on U.S. Environmental Protection Agency. (2010) 2010 MSW Facts and Figures Factsheet. Retrieved from https://www.eia.gov/todayinenergy/detail.php?id=8010.

Wang, C., Li, M., & Fang, Y. (2016). Coprocessing of catalytic-pyrolysis-derived bio-oil with VGO in a pilot-scale FCC riser. *Industrial & Engineering Chemistry Research*, *55*(12), 3525-3534.

Wang, X., Yu, Z., & McDonald, A.G. (2019) The effect of biochar as reinforcing filler on the properties of wood plastic composites. *Journal of Bionic Engineering.* 16(2): 337-353. https://doi.org/10.1007/s42235-019-0029-0.

Wang, Z., Pecha, B., Westerhof, R., Kersten, S., Li, C-Z., McDonald, A.G., & Garcia-Perez, M. (2014) Effect of cellulose crystallinity on solid/liquid phase reactions responsible for the formation of carbonaceous residues during slow pyrolysis. *Industrial & Engineering Chemistry Research*. 53(8): 2940–2955. dx.doi.org/10.1021/ie4014259

Wei, L., McDonald, A.G., Freitag, C., & Morrell, J.J. (2013) Effects of wood fiber esterification on properties, weatherability and biodurability of wood plastic composites. *Polymer Degradation & Stability*. 98: 1348-1361.

Xu, Z., Zinchik, S., Kolapkar, S. S., Bar-Ziv, E., Hansen, T., Conn, D., & McDonald, A. G. (2018). Properties of Torrefied U.S. Waste Blends. *Frontiers in Energy Research*, *6*(65), 1–13. https://doi.org/10.3389/fenrg.2018.00065

5. Paddle mixing-extrusion reactor

5.1. Summary

In Chapter (2) we presented the development of a paddle reactor that can work up 1 kg/hr with woody biomass particle of about 1 mm in size. We studied the mixing characteristics of the reactor, its thermal characteristics and the effect of mass flow rate and rotation frequency and the residence time. We also measured the heat capacity and heating rates with and without heat transfer material. Lastly, we demonstrated both torrefaction and pyrolysis and showed that our results are in agreement with literature data. A paper has evolved from this study (Zinchik et al., 2018).

In chapter (3) it was noted that woody biomass as a feedstock is a major economic hindrance for the development of the conversion to fuels (both solid and liquid). We, therefore, suggested the use of wastes, such as municipal solid waste, industrial residues, and plastic and fiber wastes. In Chapter (3) we carried out a comprehensive study on the torrefaction of waste blends and the properties of their torrefied material. Grinding energy, FTIR, and energy and chlorine content were thoroughly investigated and concluded that the produced solid torrefied fuel is a suitable and clean fuel for power applications. A second paper has evolved from this study (Xu, 2018).

In Chapter (4) we furthered the investigation of the torrefied waste blends to densification by means of extrusion and expanded our characterization methods to include thermomechanical analysis, density, FTIR, water resistance, grindability, heat content, and combustion characteristics. The results showed clearly that the extrusion yielded a significant improvement of the solid fuel with a clear indication of the suitability of the

extruded solid fuel from waste for coal power plants. A third paper has been submitted for publication (Zinchik et al., 2019).

The studies carried in Chapter (3) and (4) were carried out in bench-scale reactors with the notion to understand the behavior of waste thermal treatment and the properties of the products. As a consequence of the studies presented in Chapters (2)-(4) we decided to upscale the paddle reactor and to integrate it with an extrusion mechanism and the reach a mass flow rate of up to 70 kg/hr. If successful, it would be a significant step to move this technology towards a commercial scale. Chapter (5) presents this study with a clear indication that the integration approach is indeed valid and that the properties of the extruded torrefied products are similar to those obtained in the bench-scale studies. Further, we attempted to carry out pyrolysis experiments and showed the modification required to use this approach for fast pyrolysis.

5.2. Introduction

The motivation for the development and investigation of an up-scaled paddle-extrusion reactor is to study the controlling parameters and processes towards the further up-scaling to industrial-scale size. Clearly, mass and heat transfer plays a major role and a great deal of the current Chapters will deal with this.

The objective of this development is to increase significantly the mass flow rate of the material with the new reactor and yet to obtain products with properties that consistent with their use for power applications.

5.3. System description

5.3.1. Overview

Our approach for the development of an integrated paddle-extrusion system is presented in Figure 5.1. The feedstock is introduced in a feed hopper (1), conveyed by a Bucket elevator (2) into a Surge hopper (3) that has an agitator (4) to prevent bridging, the material drops into a feed auger (5), then an Airlock, a Rotary valve (6) – to prevent air from leaking into the reaction zone, the material then flows into the Paddle mixer with a shaft comprises an extrusion configuration (7); the reactor is fed continuously with Nitrogen generator (8) to ensure oxygen-free environment, the off-gases are being sucked by an ID fan into a furnace (10) to burn the organic material in this stream, which is then vented through a stack (according to environmental regulations). The extruded material is cooled and cut by a Cutter (9) to produce pellets. We note the outlet extruder acts also as an airlock to prevent air from entering the reactor.

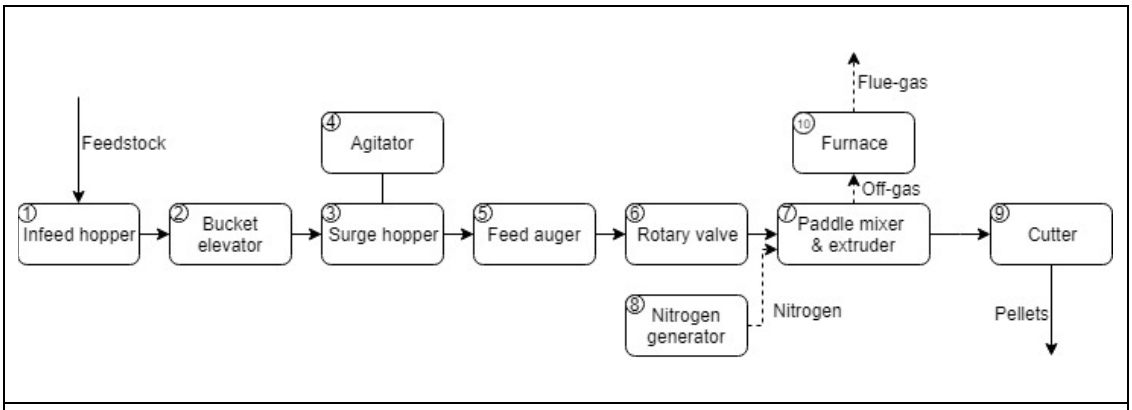

Figure 5.1. Block flow diagram.

In the next sections, we will provide details of the various components in the entire system.

5.3.2. Material handling and feeding system

The material used and conveyed in this study is similar to the one described in Chapter (3) and (4). Its density is rather low (50-300 kg/m^3) and has the tendency to bridge. For this reason, care should be given to avoiding bridging. Figure 5.2 is a schematic of the feeding system, with a surge hopper with a conical shape at an angle that is accepted in this industry, yet, due to the fact that bridging is always happening, an Agitator was added to break bridging. The material is flood fed into a screw auger with a VFD to control the mass flow rate. The material then drops by gravity into an airlock (Rotary valve).

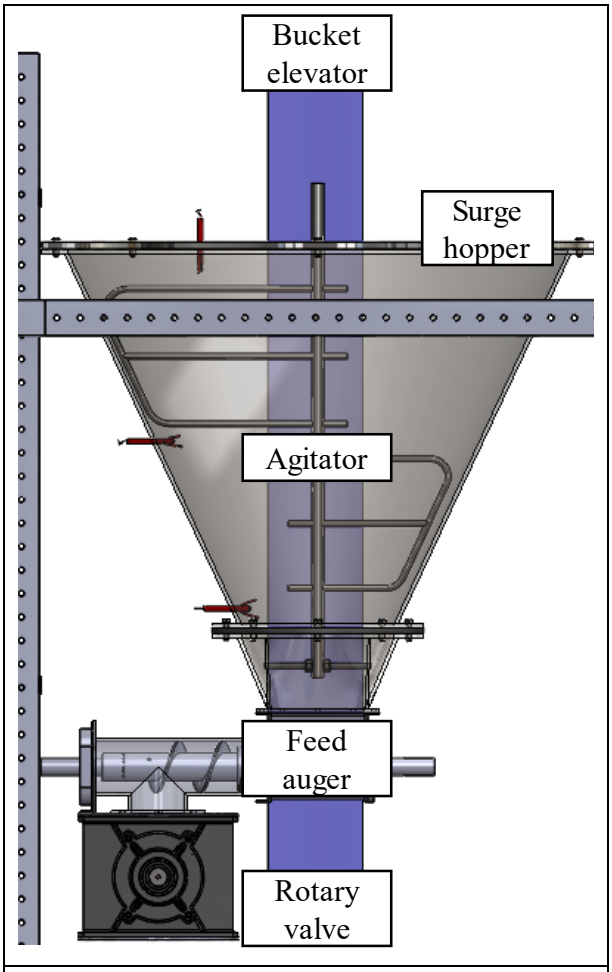

Figure 5.2. Feeding system configuration.

5.3.3. Reactor configuration

The material from the airlock falls into the paddle extruder reactor. The reactor heated electrically (detailed below) by 12 heaters with 14 thermocouples, operated by a PID controller for each heater (see below), thus with strong and accurate temperature control. Figure 5.3 a drawing of the integrated reactor with its shell, the heaters, and the thermocouples. The figure also shows the various sections in the reactor (transition zone where the material falls from the feeding system and the material is conveyed into the mixing-heating-grinding zones, the material is then moved into the extrusion zone and exits through a guiding cone and a die with 25.4 mm opening (see Figure 5.4).

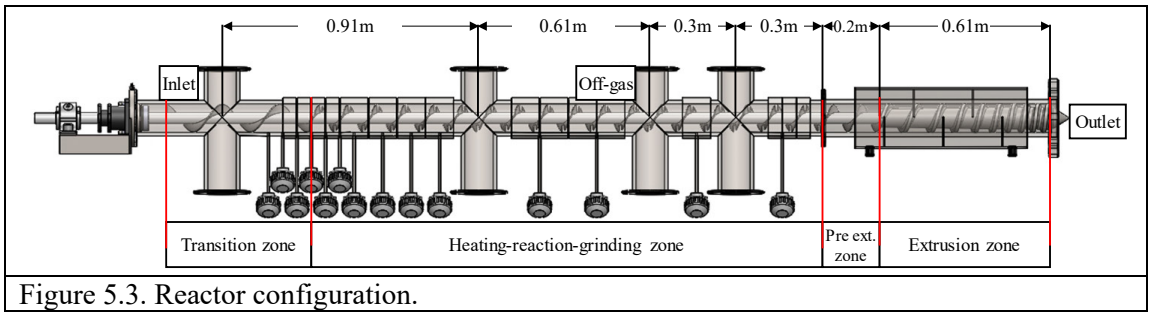

Figure 5.3. Reactor configuration.

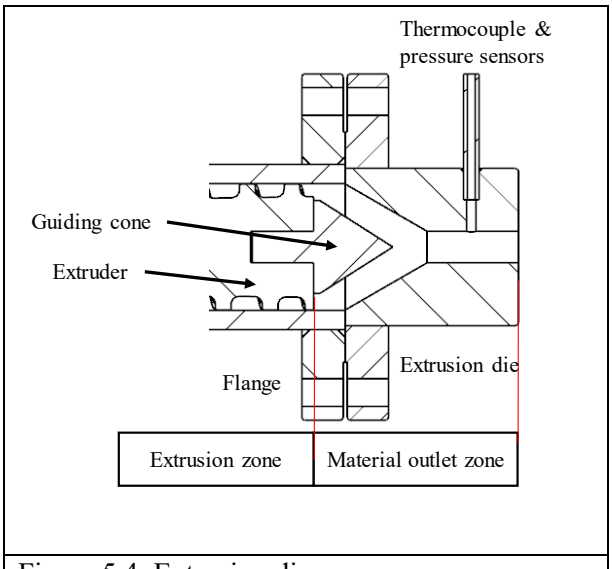

Figure 5.4. Extrusion die.

5.3.3.1. Paddle mixing

The configuration of the shaft, with its conveying screw, paddles, and extrusion parts are presented in a drawing in Figure 5.5. The shaft (38.1 mm in diameter) is made from PH15-5 stainless steel that has a higher-yielding point than regular steel to accommodate for the high pressure (from extrusion) and length (prevent bulking). The transition zone is a double-diameter pitch screw auger with three flights (totaling 0.61 m). Then, a paddle section (made from modified screw auger), 1.83 m long with 18 pitches, with a paddle pitch of 1 diameter (0.1 m). The paddles are made of screw flights (as seen in Figure 5.6) with a cut at 29% of their area. At the end of the paddle section, two pitches of uncut 1-diameter flights convey the material into the extrusion zone (detailed below).

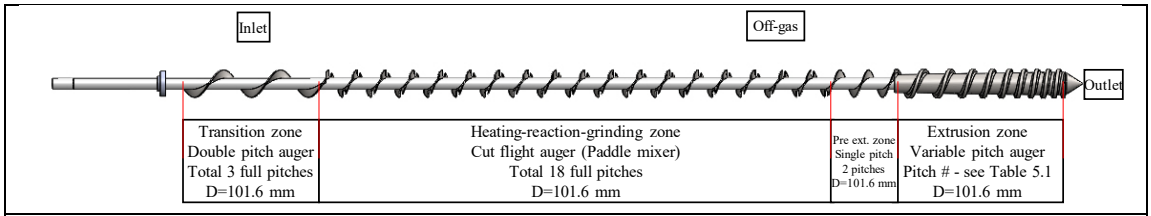

Figure 5.5. Shaft configuration.

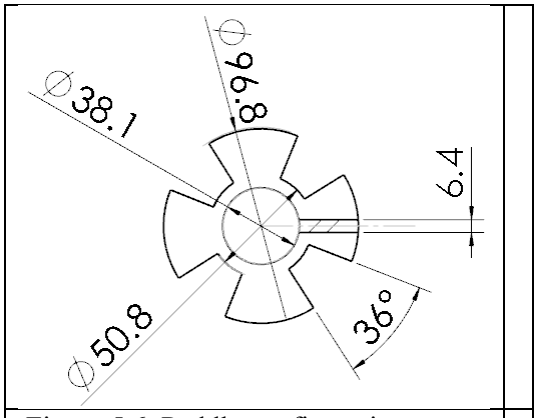

Figure 5.6. Paddle configuration.

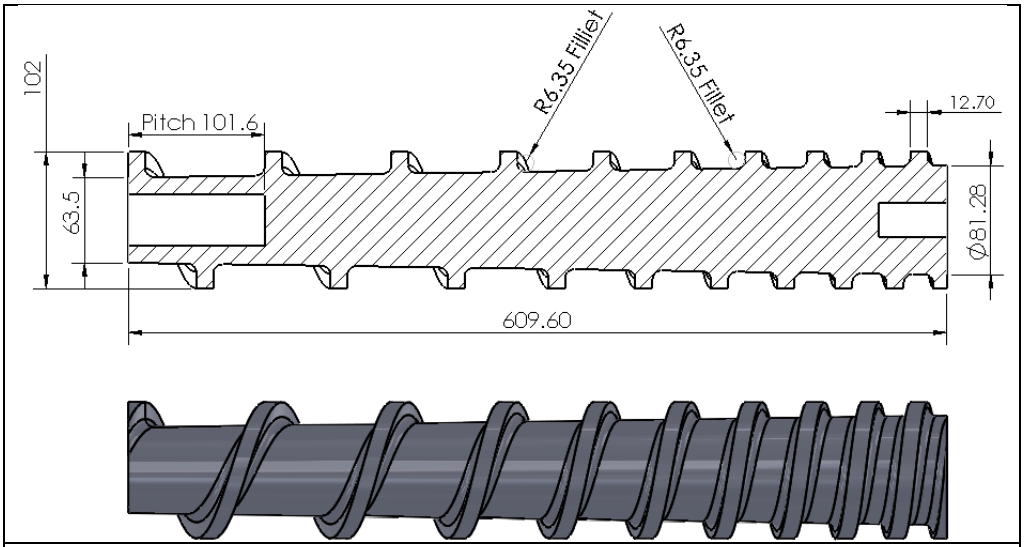

Figure 5.7. Extruder configuration.

5.3.3.2. Extrusion

The extrusion zone is drawn in Figure 5.7 with the pitch configuration detailed in Table 5.1, starting with a one-diameter pitch, which is decreased gradually in order to densify the material such that the last pitch reaches its maximum density and 100% fill (of the pitch).

Table 5.1. Extruder design parameters.

pitch #	Shaft dia, mm	Pitch, mm	Filling, %	accumulated, mm
1	63.5	101.6	13%	101.6
2	65.0	88.0	16%	189.6
3	66.3	76.4	20%	266.0
4	67.4	66.6	24%	332.6
5	68.4	58.4	29%	391.0
6	69.2	51.4	34%	442.3
7	70.0	45.4	42%	487.8
8	70.6	40.4	50%	528.2
9	79.9	36.2	80%	564.3
10	81.3	45.3	100%	609.6

The extrusion section ends with a cone and a 25.4 mm diameter die (See Figure 5.4), where the extruded material exits the reactor as a rod. This configuration with the extruded at the end of the shaft creates a plug (airlock) and separates between the reaction zone and the environment.

5.3.3.1. Heater Configuration

As indicated, the reactor shell is heated by 12 heaters (numbered 3-14), shown in detail in Figure 5.8 (in red) with a respective thermocouple for each heater. The distance of each thermocouple and heater is shown in Table 5.2.

Table 5.2. Heaters and thermocouples location and power.

TT #	Distance from the inlet, m	Heater #	Distance from inlet, m	Heater power, kW
1	0.17	1	NA	NA
2	0.22	2	NA	NA
3	0.27	3	0.24	2
4	0.32	4	0.29	2
5	0.37	5	0.34	2
6	0.42	6	0.39	2
7	0.47	7	0.47	4
8	0.57	8	0.57	4
9	0.67	9	0.67	4
10	0.77	10	0.77	4
11	1.13	11	1.13	8
12	1.33	12	1.33	8
13	1.69	13	1.69	4
14	1.99	14	2.02	6

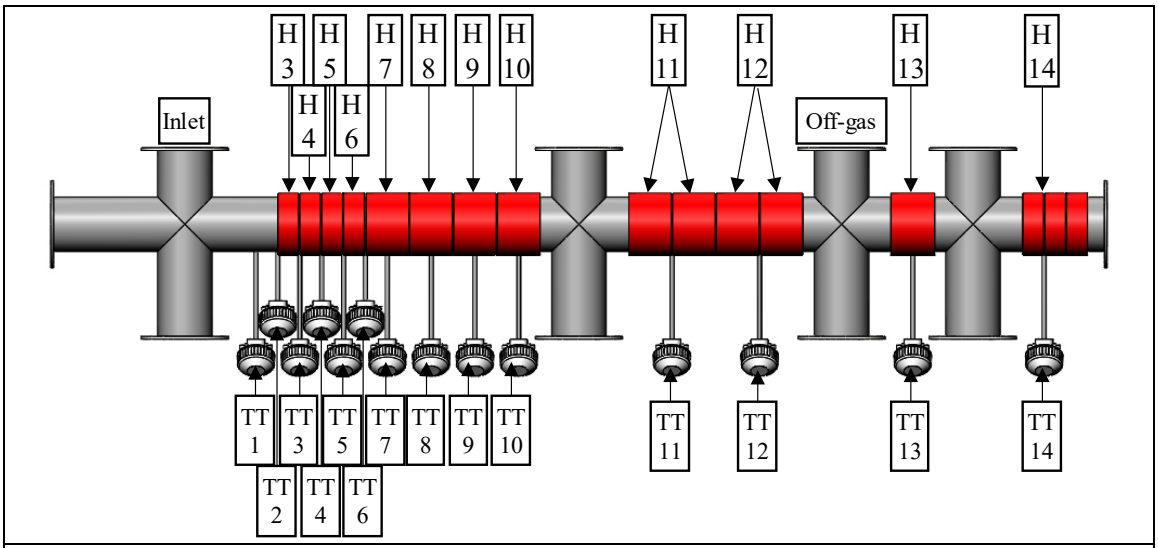

Figure 5.8. Heater and thermocouple configuration.

5.4. System behavior

5.4.1. Reactor thermal dynamics

The reactor should be heated prior to introducing material into it, therefore, understanding the dynamics of start-up and stabilization are rather important. We note that thermocouples 1 and 2 have no respective heaters and therefore they do not have set points; all other heaters are connected each respectively to a specific heater.

Figure 5.9 shows a start-up example when all thermocouples were set al 250°C. Figure Top show thermocouples 1-10 and Bottom shows thermocouples 11-14. The PID control parameters of the heaters were tuned for a fast stabilization period. All thermocouples went through an overshoot, during which the heaters were turned off automatically until the setpoint has been reached. It is important to mention we determined the PID parameters to have only one overshoot period. The cooling down is clearly dependent upon the overall heat capacity of the reactor and the quality of insulation of the heaters. Note from Figure 5.9 that Thermocouples 1-12 behave in a similar manner and

reached stabilization after 3 hours of operation. Thermocouples 13-14 have different dynamic behavior and reach stabilization after 4 hours of operation. This is because of their location. These Thermocouples operate Heaters 13-14 which are close to the extruder zone that has a significantly lower temperature, hence has different dynamic behavior.

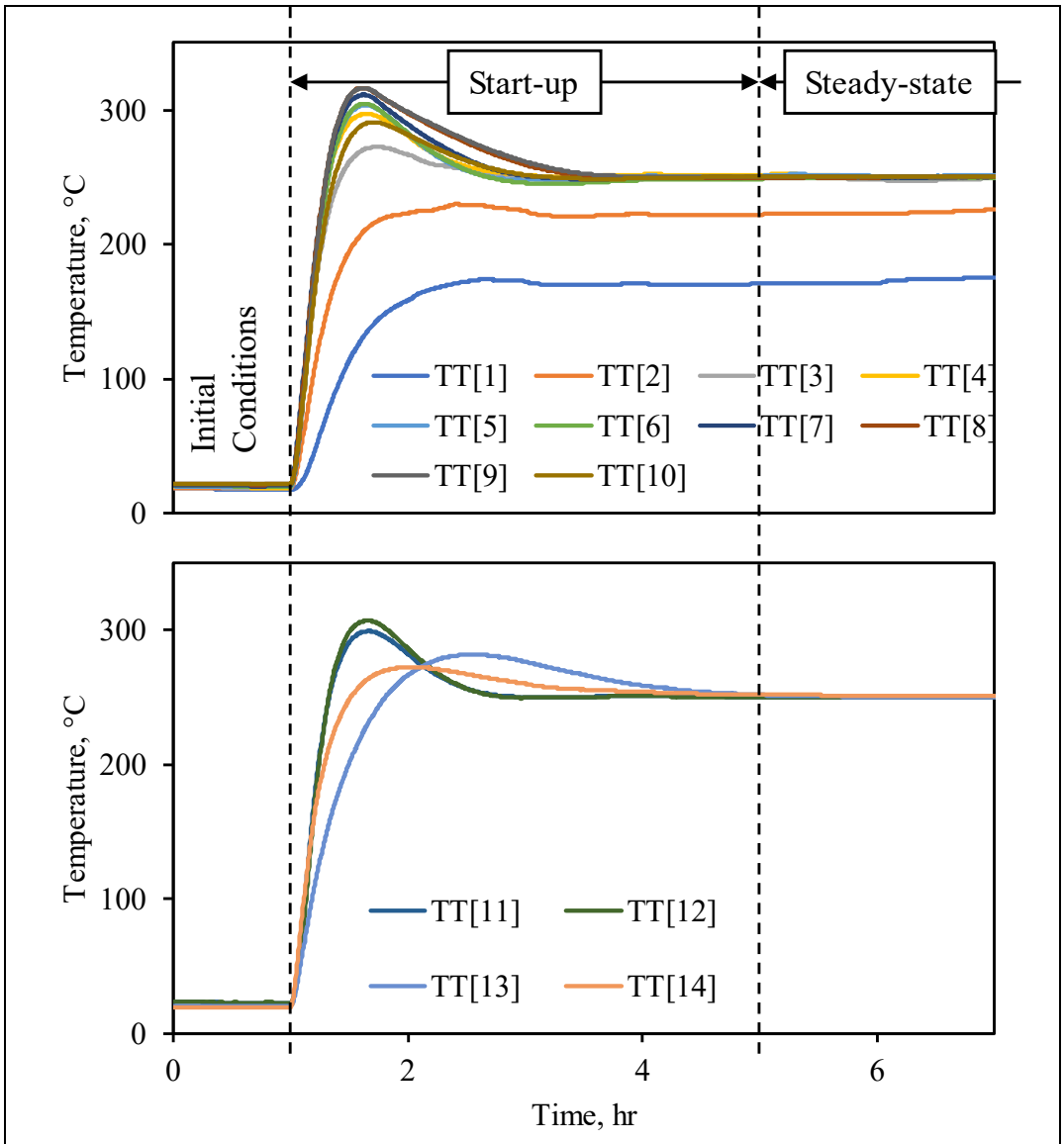

Figure 5.9. Typical heating experiment temperature transient.

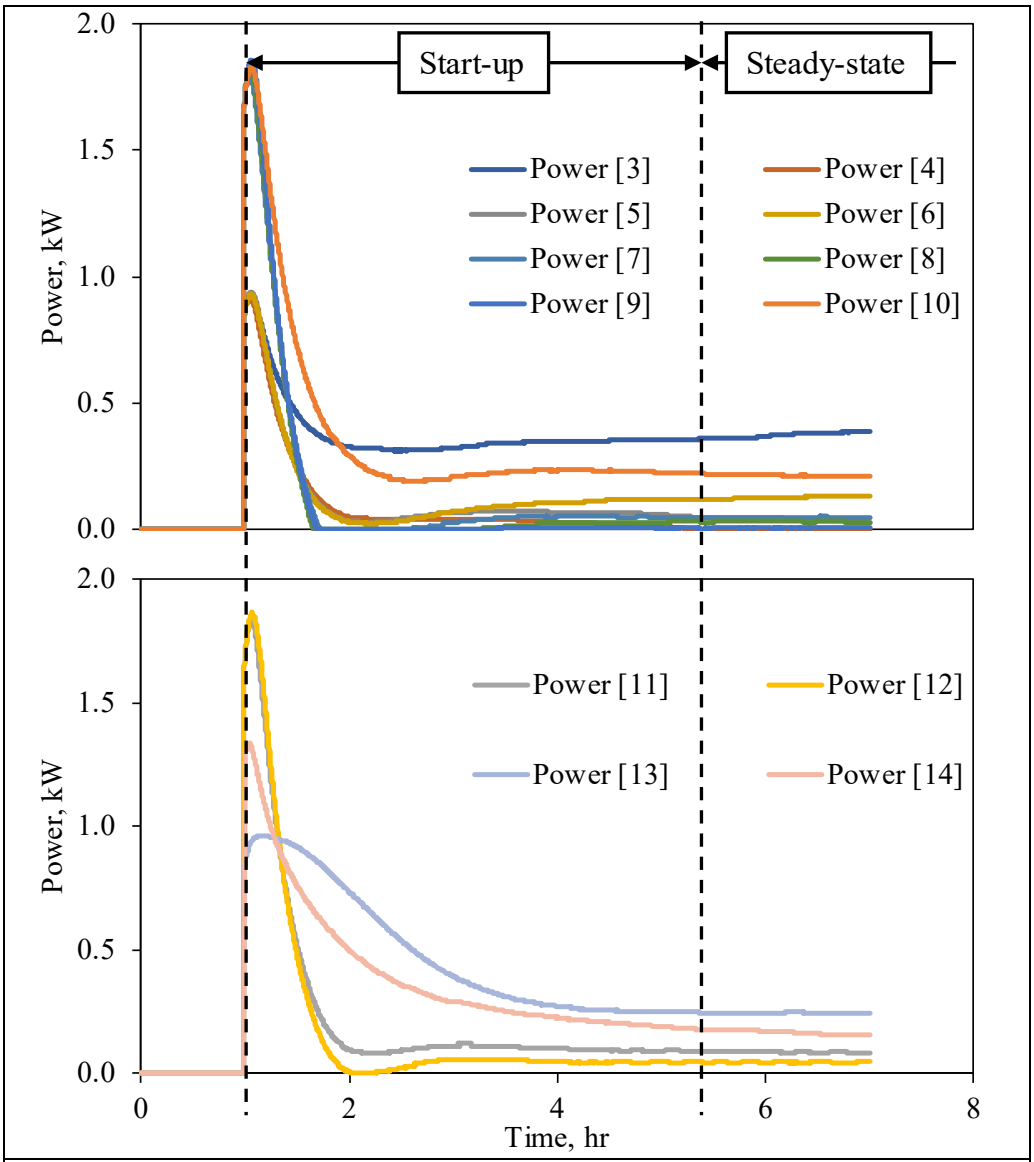

Figure 5.10. Typical power transient for a heating experiment.

Figure 5.10 shows power transients in the start-up period for Heaters 1-14. We note that without material, the power (kW) of Heaters 1-14 provides the heat losses to the surroundings. The values vary from 0-to-0.4 kW. Heater (3) is located close to the inlet of the material and to the edge of the reactor thus has the highest heat losses. Heater (14) is close to the extruder (that is not heated) and has low heat losses. However, Heater (13) is close to the gas outlet (note that nitrogen is flown at all times) and helps to heat the gas

outlet line, thus its high heat losses to the surroundings. All other Heaters show total heat losses that are less than 5% of the total heat provided to the reactor which indicates rather good insulation.

A typical experiment with material flowing in the reactor was carried out as follows:

- All reactor temperatures were let to stabilize (at the respective setpoint) without material flow until reaching stabilization, which normally took about 4 hours.
- After stabilization, the material was fed into the reactor, normally in 4-6 stages in order to avoid abrupt changes, until the mass flow rage reached its steady-state value.
- Once the system reached stabilization (in mass flow rate and temperature), the following measurements were carried out: (i) outlet mass flow rate; (ii) extruded samples were taken for characterization; (iii) electric power measurements were recorded; and (iv) heater duty cycle were recorded.
- At some point, the system was shut down, as follows: material flow was reduced gradually while the heaters were let to control the temperature as required, till the reactor reached ambient temperature. During the shutdown, nitrogen was flown to prevent internal oxidation within the reactor.

Figure 5.11 shows a typical dynamic behavior of the reactor temperatures during an entire experiment - the temperatures increase till they reach the set point. The feed stages are more clearly observed from the heater's power as shown in Figure 5.12.

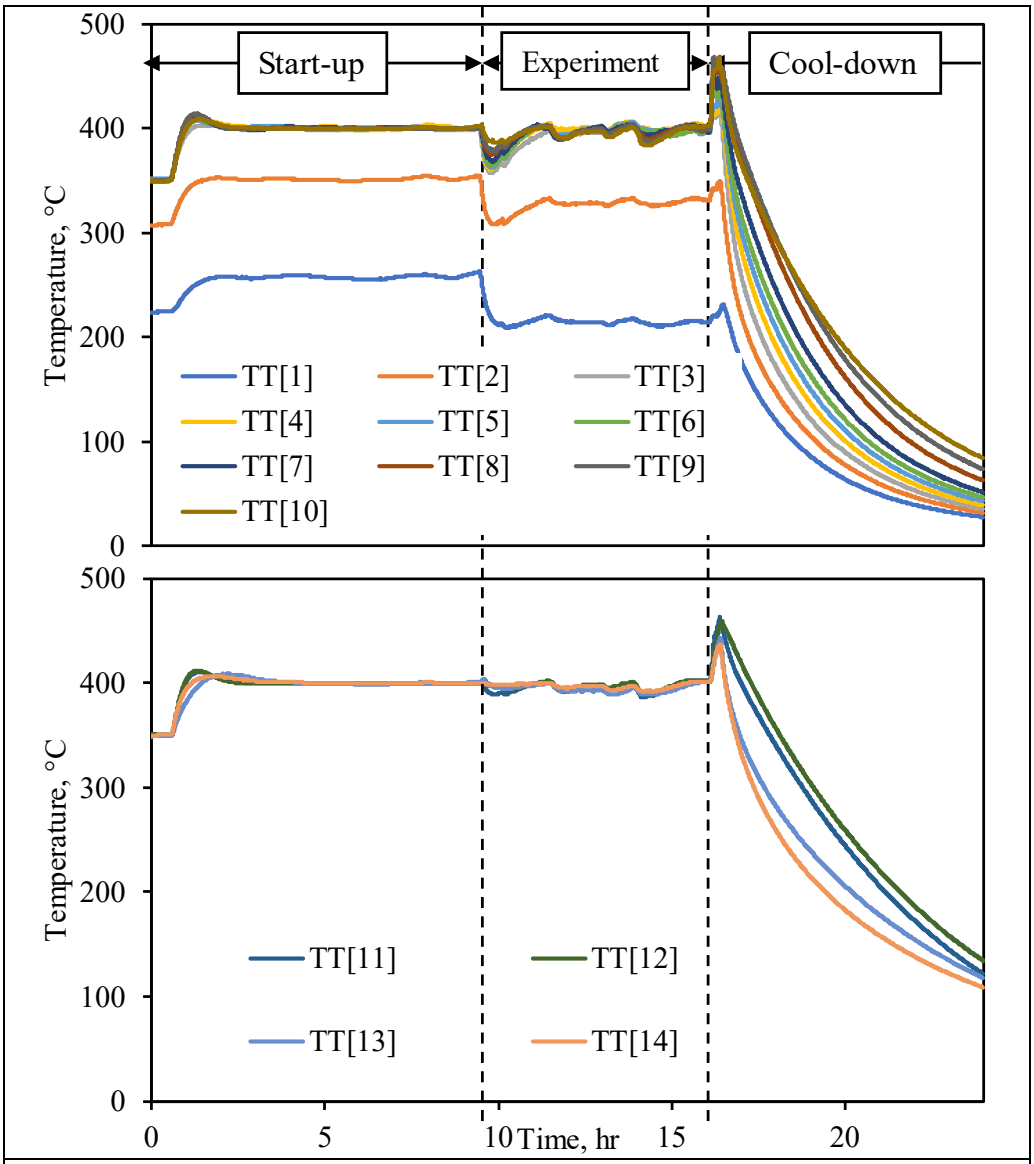

Figure 5.11. Typical experiment temperature transient.

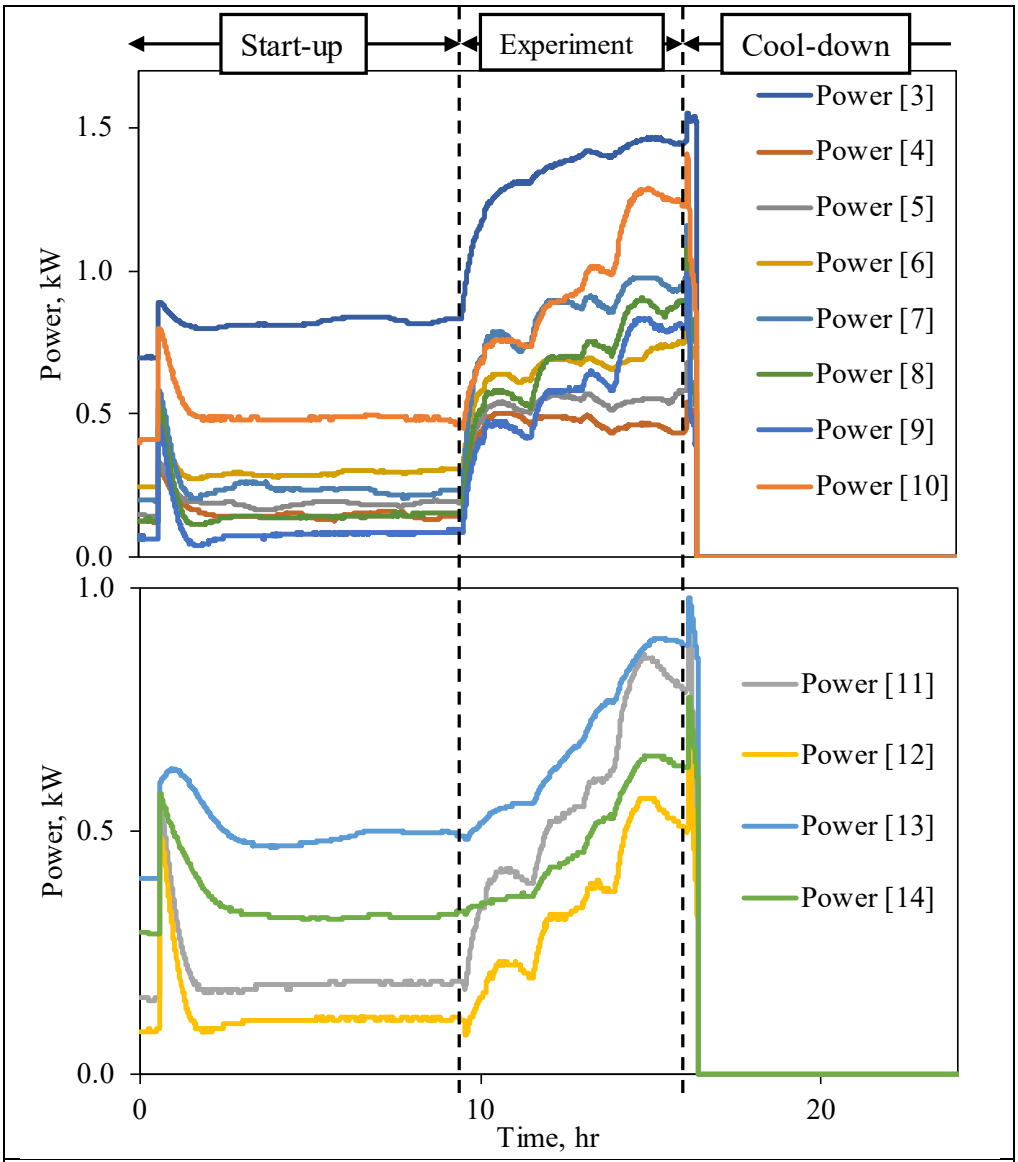

Figure 5.12. Typical power transient for an experiment.

5.4.2. Mass flow rate

The mass flow rate was measured in two different methods:

(i) When the feed auger was NOT connected to the reactor. The weight was measured automatically with a weighing scale that was connected to an acquisition system that recorded data in real-time. The mass flow rate

results showed a linear behavior with the feeding auger shaft rotation frequency with an R2~1.

(ii) When the feed auger was connected to the reactor. We note that in order for the material to be conveyed in the reactor, the reactor temperature should be at least 180°C, which is when the plastic wastes melted, and the blend was able to be conveyed through the extruder. Figure 5.13 shows schematics of these measurements, where a weighing scale was placed under the outlet of the extruder (die) and the weight was monitored continuously. Figure 5.14 shows an example of the accumulated weight vs. time with R2=0.99, from which the mass flow rate was calculated.

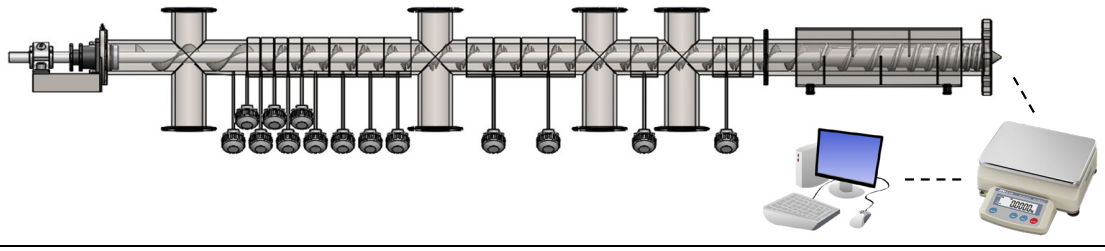

Figure 5.13. Schematic of flow rate measurement.

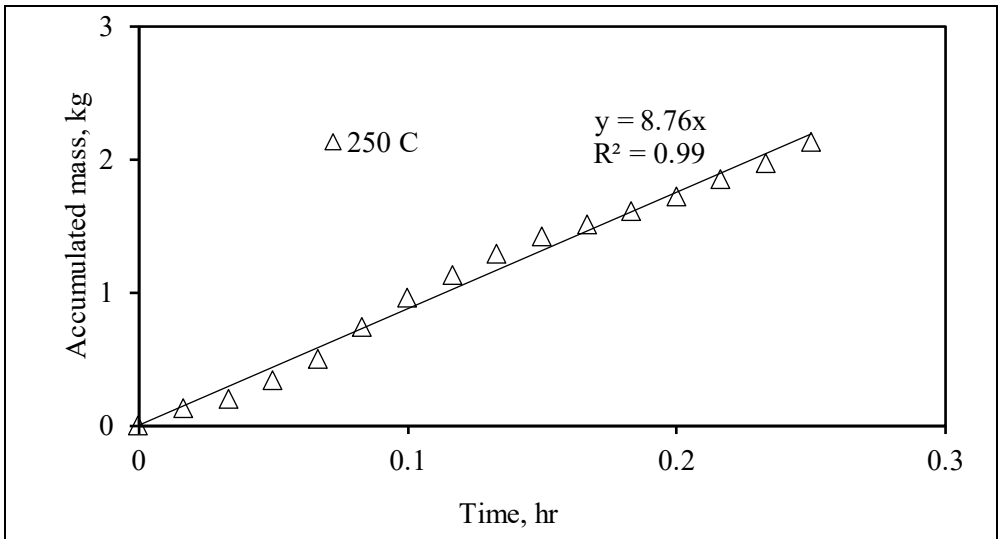

Figure 5.14. Typical mass flow rate experiment results.

Figure 5.15 shows the results of the mass flow rate vs. the feed auger rotation frequency showing the expected linear behavior with R^2=0.98. The bulk density of the material was calculated by dividing the mass flow rate in the feed auger, by the volume flow rate of the feed auger (the volume between one flight), to yield a bulk density of 212 kg/m^3 for the material.

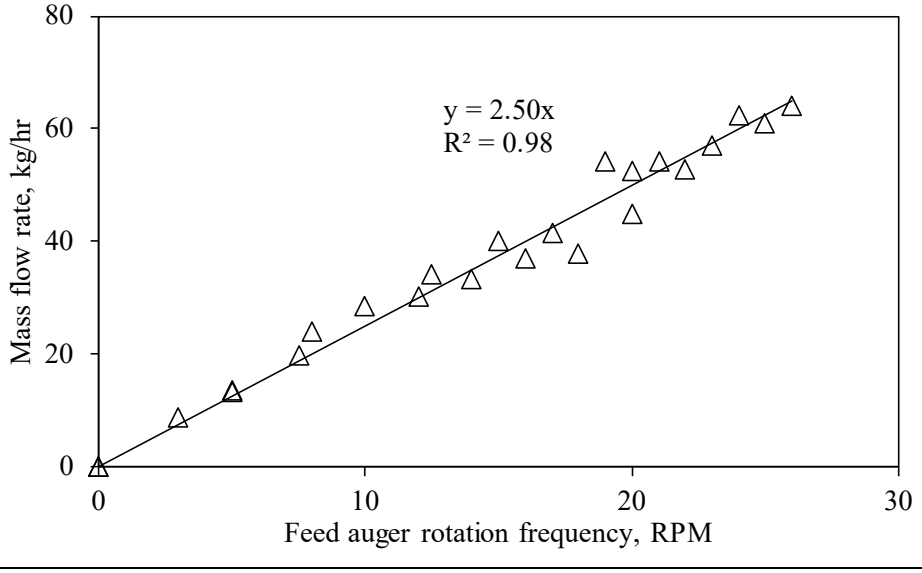

Figure 5.15. Mass flow rate experiments summary.

5.4.3. Residence time

Residence time is an essential variable to control the extent of reaction, thus should be measured. In this reactor, the relevant residence time is right before the material flows into the extruder, as the temperature drops significantly, and no reaction occurs at this zone. As we could not use the same method developed in Chapter (2) for residence time measurements, we developed a new method based on the reactor motor power. The idea is that when the material reaches the extruder zone, there should be a sudden increase in the motor power rotating the shaft. The experiment was carried out as follows: (i) the feed auger motor was turned off; (ii) the reactor motor was rotating continuously to empty the

reactor; (iii) the feed auger was turned on at a given frequency, then turned off at a predetermined time interval, (iv) the auger and reactor motor loads were monitored continuously, and (v) after a given experiment, the rotation frequency of the reactor motor was changed and stems (i-iv) were repeated.

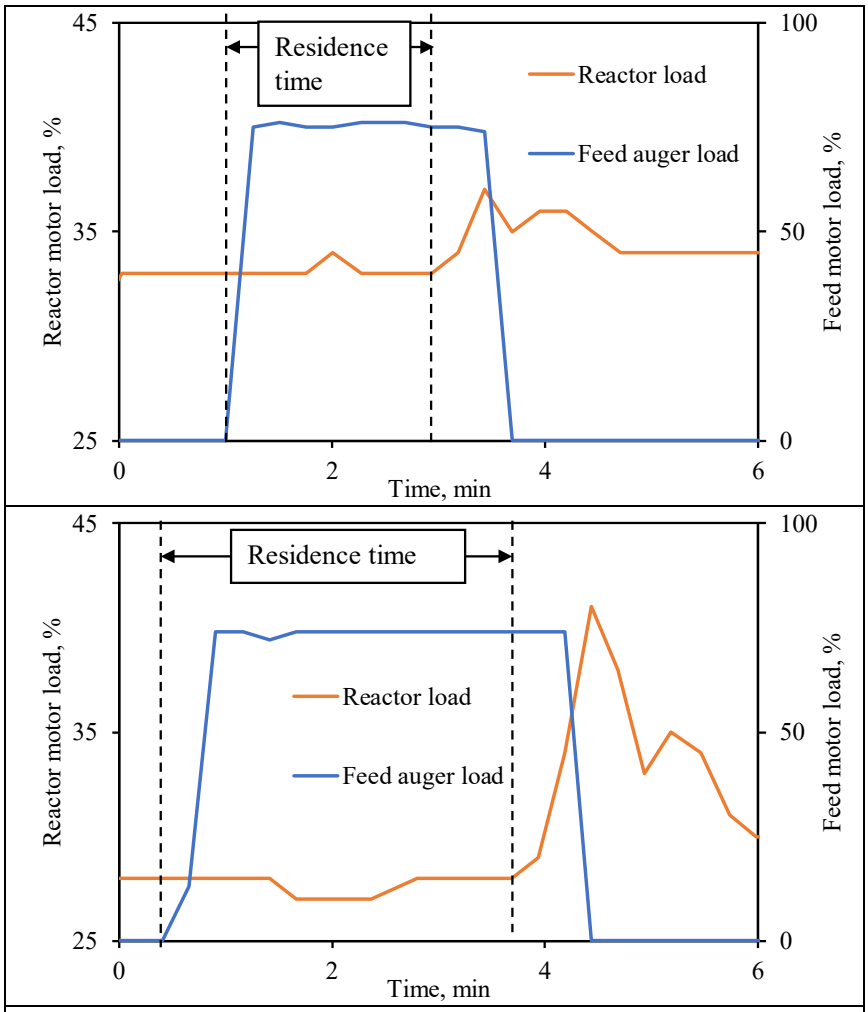

Figure 5.16. Typical residence time motor load transiants.

Figure 5.16 shows typical examples of the feed auger and reactor motor loads. The figure also shows the time where there was an abrupt increase in the reactor motor load that was used to determine the residence time. Figure 5.17 is a plot of the residence time as a function of the rotation frequency of the reactor shaft, showing a linear behavior with

R=0.99. The figure also includes a dashed line, which is the expected residence time if the reactor had a screw configuration. As there are paddles that delayed the material movement, it is expected that the paddle reactor would have a longer residence time. Indeed, the residence time is a factor of two and half longer than for a screw auger. Since the length of the reactor is known the residence time is a direct indication of the mean axial velocity in the Heating-reaction-grinding zone (see Figure 5.3). This velocity depends on the rotation frequency (RPM) of the reactor shaft and equal to 0.58 mm/s per RPM of the reactor.

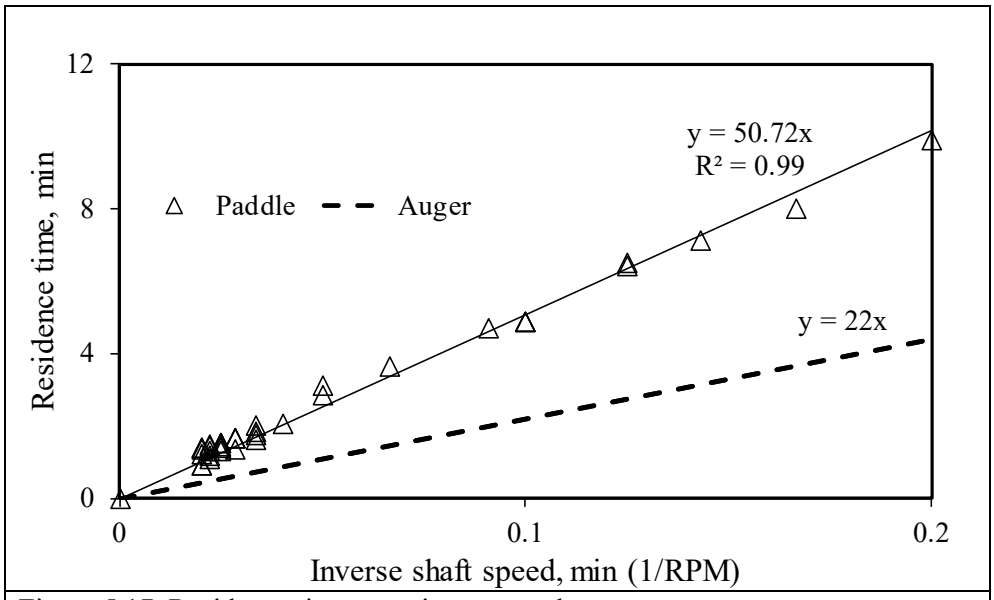

Figure 5.17. Residence time experiments results.

5.4.4. Process energy requirement

An important aspect of the industrial operation of such a system is the electric energy required for the process. In a common extruder with L/D=12-40 (Giles, Mount, & Wagner, 2004), while our extruder has a value for L/D=6. To measure the electric energy required we carried out the following experiment: (i) the reactor was emptied and operated without material, (ii) the reactor shaft frequency was set at a given value and the motor

power was recorded, (iii) the shaft frequency was then changed and the power was measured and so on till covered the reactor shaft frequency in the range 8-50 rpm. The motor power was plotted vs the shaft rotation frequency. The same measurements were carried out with material flowing through the reactor, keeping the material volume fraction in the reactor constant. The volume fraction, α, is given by Eq. (5.1)

$$\alpha = \frac{\dot{m}tres}{\rho V_{reactor}} \tag{5.1}$$

where $\dot{m}$ is mass flow rate, t_{res} is residence time, and ρ is material density. To keep constant volume fraction while changing the rotation frequency (inverse to residence time as seen in Figure 5.18) the mass flow rate has to be modified accordingly. Figure 5.18 shows reactor motor power vs. rotation frequency for an empty reactor (triangles); it also shows the motor power when the reactor was loaded to keep a constant volume fraction. As seen, there is only a slight difference between and empty reactor and a loaded one. To determine the specific electric energy, the motor power was plotted vs. the mass flow rate, as seen in Figure 5.19, from which a value of 0.14 kWh/kg (MWh/ton) was determined.

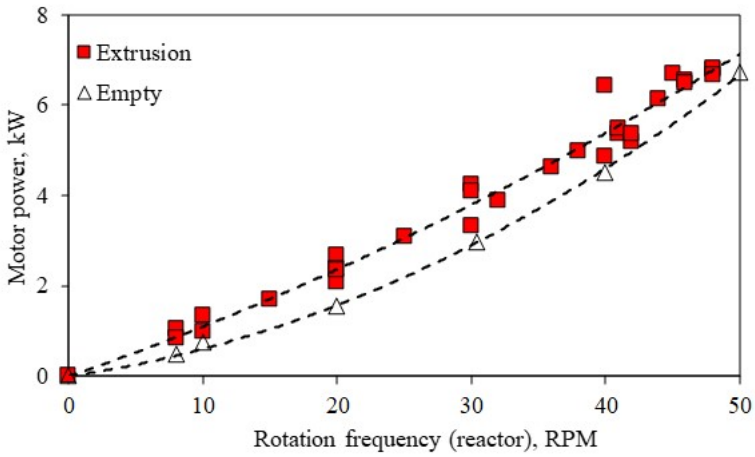

Figure 5.18. Motor load vs. rotation frequency of the reactor, empty and loaded.

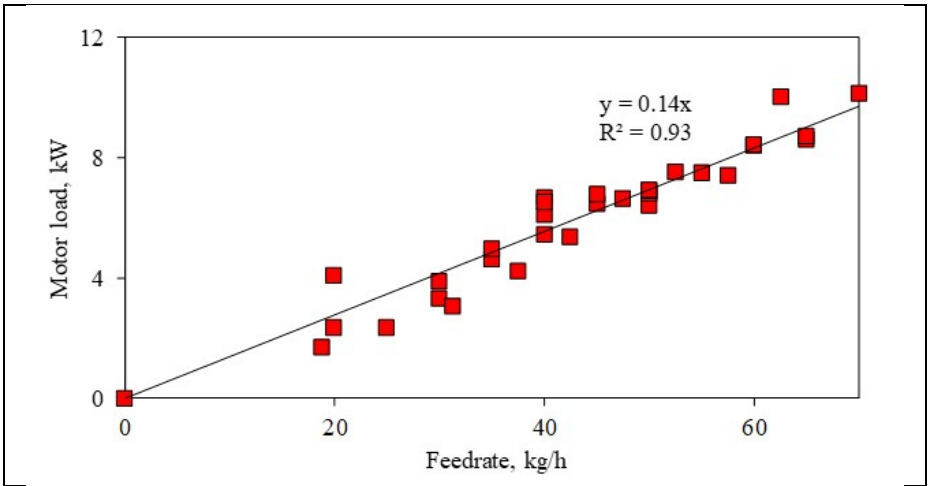

Figure 5.19 – Motor load vs feed rates.

5.5. Waste thermal degradation

The term degradation refers to the decomposition of the polymer and other groups in the waste blend. As noted in Chapters (3) and (4) our motivation was focused on waste blends as the feedstock to produce fuels. The degradation process is a coupled reaction-heat-mass-transfer system, which depends on (i) reactor and shaft configurations, (ii) thermal properties of the feedstock (thermal conductivity and heat capacity), (iii) material characteristics size, (iv) reactor temperature profile, (v) chemical reaction rate, and (vi) residence time. These factors can be strongly inter-correlated to each other except the residence time that depends on the reactor configuration (geometry, dimensions), the shaft configuration (screws, paddles, etc.), and rotation frequency. For this reactor and for two different shaft configurations the residence time was measured in Sections 5.4.3 and 7.1. The other factors are strongly coupled:

(i) Reactor temperature profile depends on the thermal properties of feedstock, its mass flow rate, and material characteristic size.

(ii) The reaction rate, on the other side, depends on the temperature profile as well as the residence time. However, the products produce material that has different thermal properties than the original feedstock and hence affects the temperature profile.

Thus, the first step is to determine the temperature profile of the material within the reactor, the next Section deal with this issue.

5.5.1. Reactor temperature profile and radial uniformity

To determine the degradation kinetics of our waste in this reactor system, we need to know the reaction rates, the residence time, and the temperature. The reaction rates were measured in Chapters (3) and (4) for our material and will be used here. The residence time was determined in Section 5.4.3 and a correlation between the residence time and the reactor shaft frequency was found. To have an unambiguous determination of the extent of thermal degradation of our material, we must know: (i) the axial temperature within the reactor for a given rotation frequency (or residence time), and (ii) whether or not the radial temperature at a given axial distance is uniform. This section will deal with the determination of the temperature and its radial uniformity.

We note that the setpoints of the temperature are controlling the reactor wall temperature. This said the question is whether the material temperature is equal to the wall temperature. Heat balance calculations can provide an estimate of the material temperature, at a given axial distance, from the heat provided by the heaters to the reactor walls.

For a given axial distance and mass flow rate (at thermal steady state), the heat rate transferred to the flowing material is given by Eq. (5.2)

$$\dot{Q}_{net}(x) = \dot{Q}_{tatal}(x) - \dot{Q}_{loss}(x) \tag{5.2}$$

where $\dot{Q}_{net}(x)$ is the net heat rate transfer to the material as a function of the axial distance, $\dot{Q}_{total}(x)$ is the total heat rate as a function of the axial distance, and $\dot{Q}_{loss}(x)$ is the heat rate losses as a function of axial distance. Figure 5.20 shows a schematic of material (at a mass flow rate $\dot{m}$) flows through a control volume defined by axial distance x and $x + \Delta x$, with $\dot{Q}_{net}(x)$ responsible to heat the material from the reactor walls. From heat balance considerations, the temperature at $x + \Delta x$ is given by Eq. (5.3). It is noted that the axial distance can be converted into residence time as described in Section 5.4.3.

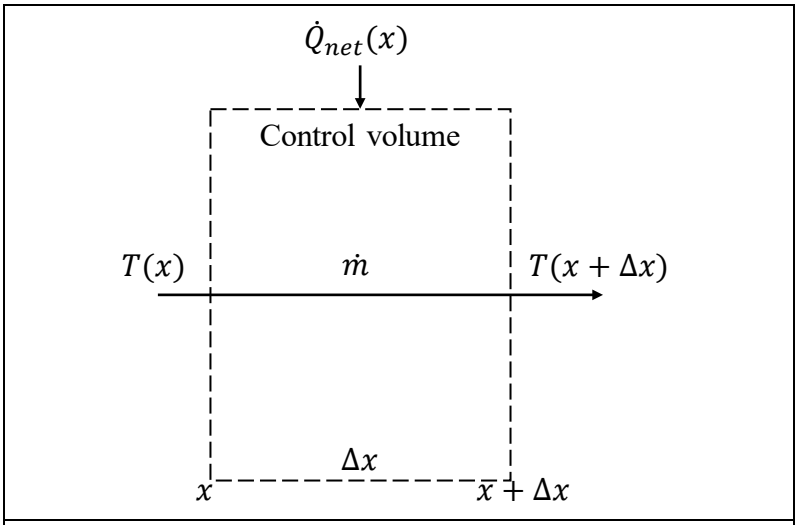

Figure 5.20. Schematic of the net heat rate and a control volume.

$$T(x + \Delta x) = \frac{\dot{Q}_{net}(x)}{c_p \dot{m}} + T(x) \tag{5.3}$$

The temperature determined by Eq.(5.3) provides the effective temperature but does not necessarily indicate whether the temperature is uniform through the radial coordinate. To obtain radial temperature uniformity the characteristic heating time the

material moving in the axial direction should be smaller than the residence time in the control volume. The characteristic heating time can be defined as presented in Eq. (5.4)

$$Characteristic\ heating\ time = \frac{Heat\ required}{Heat\ transfer\ from\ walls} \tag{5.4}$$

Therefore, the characteristic heating time, τ, given by Eq. (5.5)

$$\tau = \frac{mc_p \Delta T_{axial}}{\lambda A \frac{\Delta T_{radial}}{\Delta r}} \tag{5.5}$$

where m is mass in the control volume, c_p is the specific heat capacity, ΔT_{axial} is the temperature difference between the boundary layers in the control volume (axial), λ is the feedstock thermal conductivity coefficient, A is the area through which heat is transferred from the walls into the feedstock, $\frac{\Delta T_{radial}}{\Delta r}$ is the temperature gradient from the wall into the layer of material (or characteristic length Δr). The mass, m, is given by Eq. (5.6)

$$m = V_{contol} \alpha \rho \tag{5.6}$$

where $V_{control}$ is the control volume, α is the volume fraction of the material in the control volume, given by Eq. (5.1), and ρ is its density. Introducing α into Eq. (5.6) yields Eq. (5.7)

$$m = \frac{V_{control} \dot{m} t_{res}}{V_{Reactor}} \tag{5.7}$$

The ratio of the control volume to the reactor volume is given by Eq. (5.8)

$$\frac{V_{control}}{V_{Reactor}} = \frac{\Delta x}{L} \tag{5.8}$$

where Δx is the axial length of the control volume and L is the reactor length. Introducing Eq. (5.8) into Eq. (5.7) yields Eq. (5.9).

$$m = \frac{\dot{m} t_{res} \Delta x}{L} = \frac{\dot{m} \Delta x}{v} \tag{5.9}$$

where $v = \frac{L}{t_{res}}$. Introducing Eq. (5.9) into Eq.(5.5) yields Eq. (5.10)

$$\tau = \left(\frac{\dot{m} c_p}{\lambda v}\right)\left(\frac{\Delta T_{axial}}{\Delta T_{radial}}\right)\left(\frac{\Delta x \Delta r}{A}\right) \tag{5.10}$$

where $A = \pi D \Delta x$ and when combined with the above equation yields Eq. (5.11)

$$\tau = \left(\frac{\dot{m} c_p}{\lambda v}\right)\left(\frac{\Delta T_{axial}}{\Delta T_{radial}}\right)\left(\frac{\Delta r}{\pi D}\right) \tag{5.11}$$

The term $\frac{\dot{m} c_p}{\lambda v}$ is a constant regardless of reactor location that depends on the mass flow rate, $\dot{m}$, the material thermal properties, $\frac{c_p}{\lambda}$, and the shaft configuration and rotation (v). The term $\frac{\Delta T_{axial}}{\Delta T_{radial}}$ is a dimensionless variable that governs the heat transfer rate from the reactor walls into the material such that the smaller the term the faster the heat transfer. Because the heat source is the reactor walls this term can never be larger than unity. This term depends on the reactor location; it is the smallest in the inlet and increases with axial distance and equals unity when the material temperature equals the wall temperature (no more heat transfer). The last term, $\frac{\Delta r}{\pi D}$ represents the dimensionless variable that governs the depth of heat propagation into the material. Under the assumption that the material is distributed equally over the circumference of the inner wall and this layer is thin ($\frac{\Delta r}{D} \ll 1$) we can define Δr by Eq. (5.12).

$$\Delta r = \frac{\alpha V_{reactor}}{\pi D L} = \frac{\dot{m}}{\rho \pi D v} \tag{5.12}$$

For a given set of conditions (i.e., $\dot{m}$, shaft rotation frequency, c_p, λ and set temperature for the reactor walls), the significance of the value of τ is whether or not the moving material became uniform in temperature in the radial directions. In other words, does the material have a uniform effective radial temperature for a given axial distance? For the given case, if τ is smaller than Δt (the time interval in the control volume), the radial temperature is uniform and can be calculated from Eq. (5.13)

$$T(t + \Delta t) = \frac{\dot{Q}(t)}{c_p \dot{m}} + T(t) \tag{5.13}$$

We will present here results for the axial temperature profile as well as the characteristic time for the radial heat transfer for three cases, representing the temperature range of 250-500°C.

Figure 5.21 Top shows the power of the heaters as a function of residence time for the following set point: 250°C, 400°C, and 500°C. Generally, the heating power decreases with time (axial distance) for all temperatures and the total heating power decreases with temperature. We used these heating power profiles to calculate the effective temperature by Eq. (5.13) and presented in Figure 5.21. To calculate the temperatures, the value of c_p should be known, which depends on temperature. Further, due to the reaction, the material changes its properties, including the value of c_p, and its temperature dependence. As this information is not available in the literature, we estimated the values of c_p for each case from the heating power, the mass flow rate, and the temperature difference, which yielded an average value of 1.8±0.2 kJ/kg-°C. Clearly, this is an average value that assumes no

dependence on c_p on temperature. The next study should develop an accurate method of measuring c_p as a function of temperature and mass loss. For the current study, this average value will be used. For 250°C case the temperature gradually increases and reached ~250°C after ~5.5 minutes. For the 400°C case, the temperature reaches this value after ~6.2 minutes. For the 500°C case, the temperature reached this value only at the end of the reactor, i.e., after 6.5 minutes.

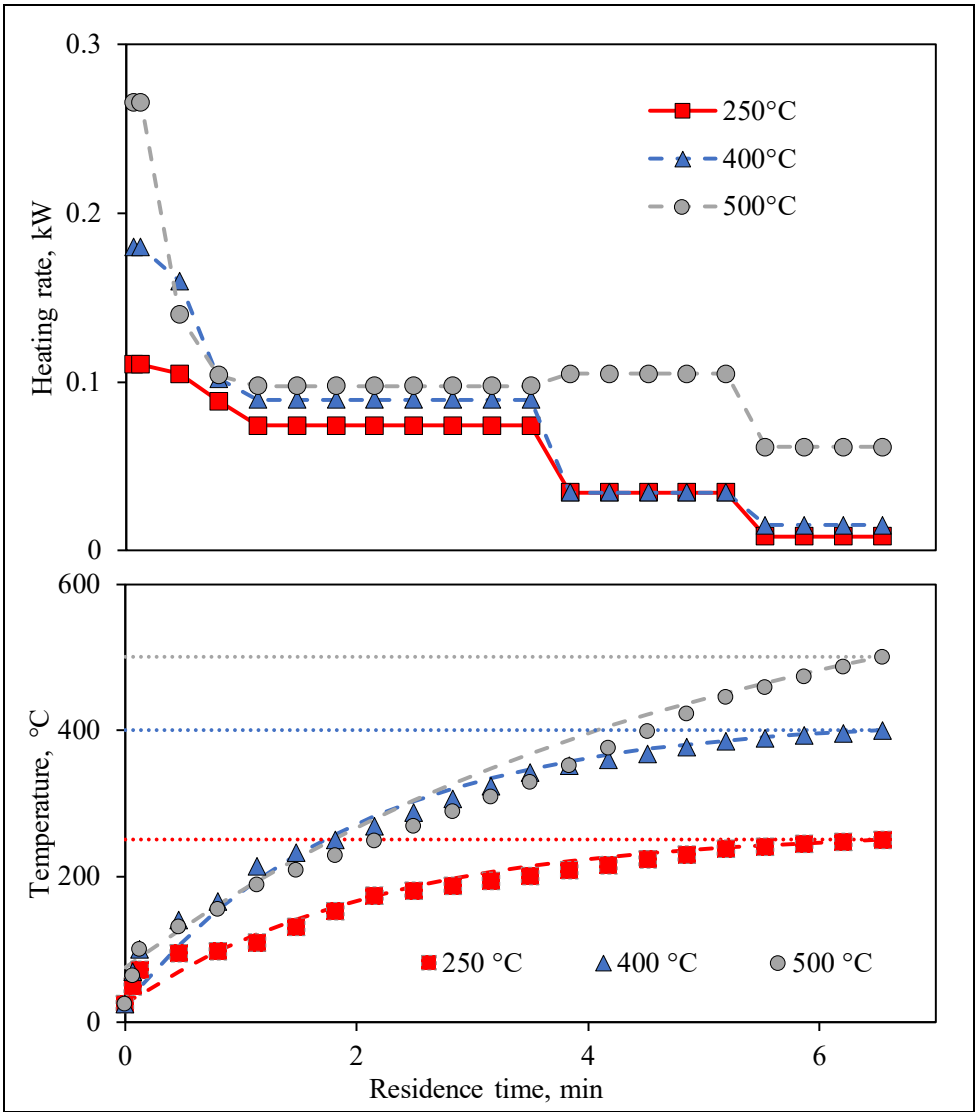

Figure 5.21. Top – heating rate vs. residence time, Bottom – the calculated material temperature vs. residence time. The residence time is derived from the axial coordinate.

The temperature uniformity, defined by the characteristic time, τ, was studied using Eq. (5.11). The residence time in the reactor depends on pitch shape and dimension. The residence time for each pitch in the reactor (Δt), for the specific configuration provided in Figure 5.5, at a rotation frequency of 8 RPM, was calculated and presented in Figure 5.22. As seen, the residence time starts from low values due to the use of a double diameter pitch (two of them), which is followed by much longer residence time, due to the (1) cuts in the flights, and (2) the pitch is a one-diameter long. The characteristic times for the radial heat transfer was determined by Eq. (5.9) for the three cases described above and plotted in Figure 5.22, noting that τ for all cases is approximately equal for all cases and all residence time and has values ranging in 3-5 s, whereas the residence time in each flighting is 7.5 seconds in the first two flights and is 23 seconds in the rest. The values τ are significantly smaller than the residence time in all cases, which indicates that the material has a uniform radial temperature in the entire reactor.

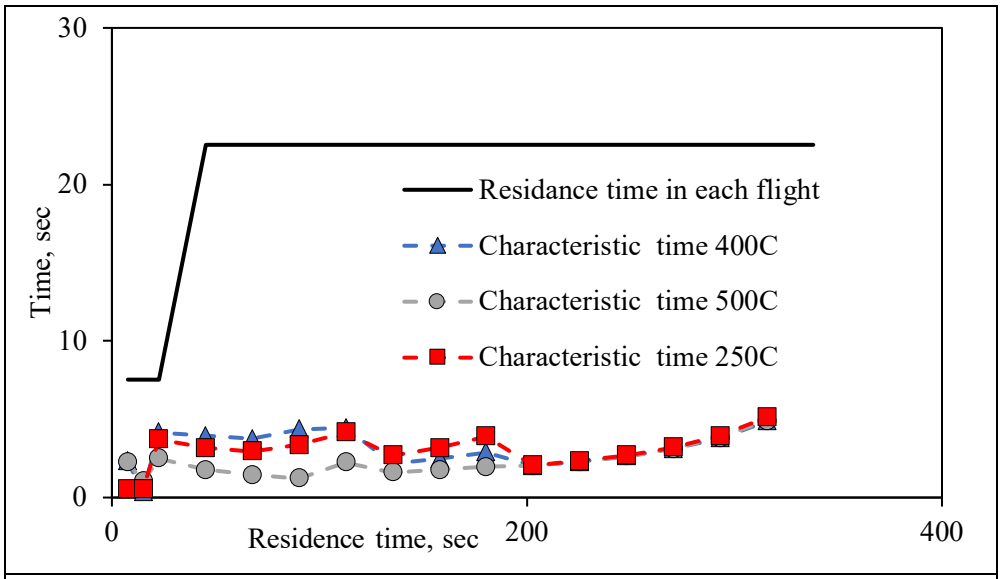

Figure 5.22. Residence time vs time, measured and characteristic.

5.5.2. Reaction extent

From the results of temperature vs. time presented above in Figure 5.21 Bottom, the reaction rate propagates as a function of temperature and time. As noted above, the activation energy (denoted by a characteristic temperature) of this reaction used here was $T_a=15{,}500\ (K)$ as determined in Chapters (3) and (4), thus knowing the temperature, residence time, and using the reaction rate, one can calculate the extent of reaction in the reactor. Using the results of temperatures from Figure 5.21 Bottom, the extent of reaction (mass loss) was calculated as a function of the residence time and presented in Figure 5.23 at 250°C, 400°C, and 500°C. The figure includes two presentations for the mass loss axis: (1) linear scale, and logarithmic scale. In the former only the 500°C results show noticeable change, whereas in the latter it is clear that there mass loss for all temperatures.

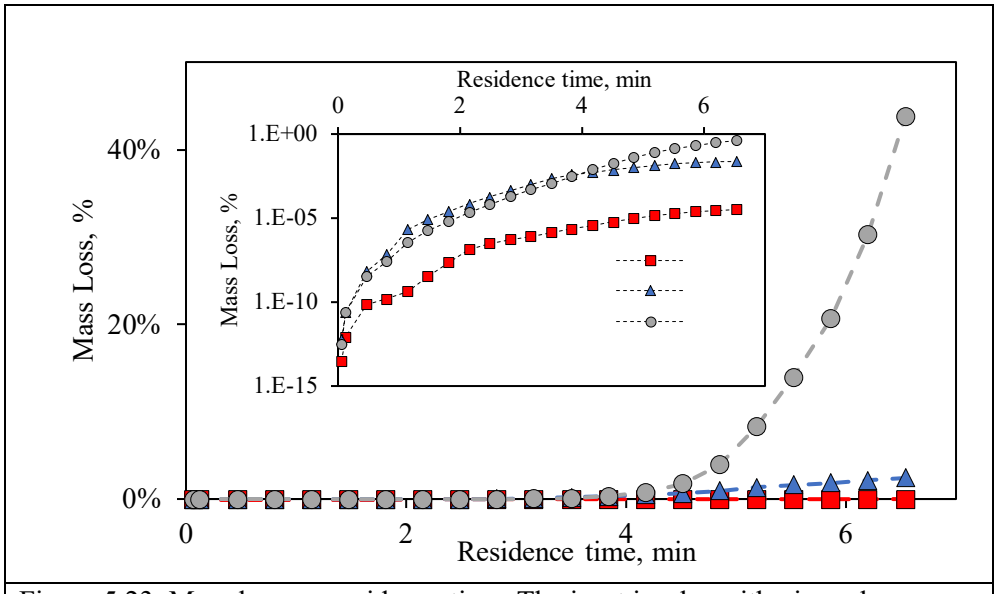

Figure 5.23. Mass loss vs. residence time. The inset is a logarithmic scale.

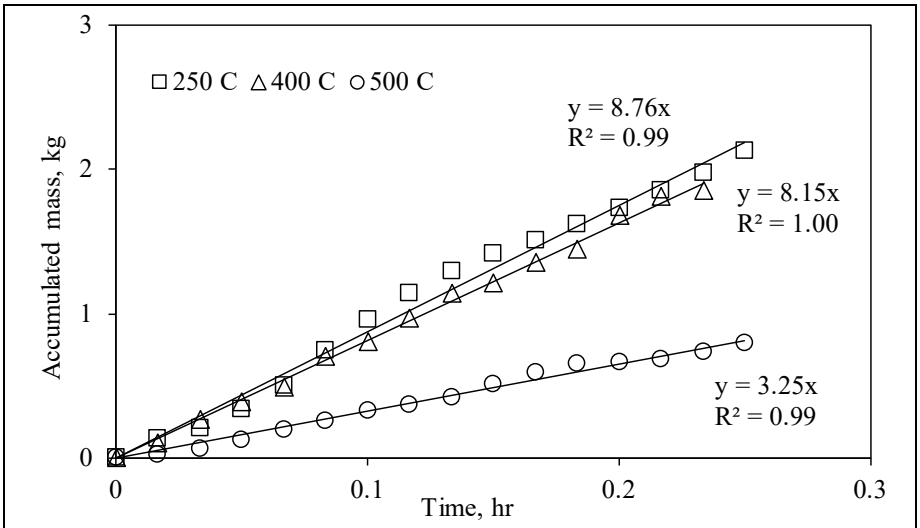

Figure 5.24. Feed rates at 250°C, 400°C and 500°C.

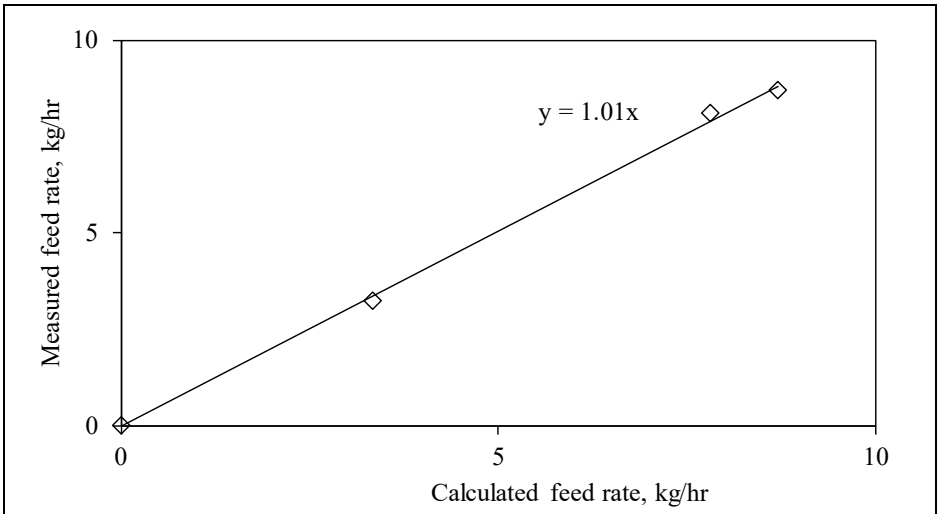

Figure 5.25. Measured feed rate vs. calculated feed rate

We note that the mass flow rate was measured only at the reactor outlet, as shown in Figure 5.24 where the output accumulated mass was plotted vs. time, from which the outlet mass loss was determined for the three temperatures, with slope values (kg/hr) and R^2 is indicated in the figure. However, as we did not measure the mass loss as a function of residence time in the reactor, we can compare measured outlet mass loss to those

calculated from the reaction rate (see Figure 5.22). Figure 5.25 is a plot of the measured feed rate vs. the calculated one, showing a good fit between the results.

5.5.3. Torrefied extruded pellets

Figure 5.26. extruded rods. Top – no thermal degradation, reactor temperature at 250°C, Bottom - (left) low torrefaction, reactor temperature at 350°C, and (right) high torrefaction, reactor temperature at 500°C.

Numerous torrefaction experiments were carried out in order to study the properties of the extruded solid fuel produced. Figure 5.26 shows the die outlet for three cases: Top – material that was flown in the reactor when the sent point was 250°C, noticing no apparent reaction. Bottom-Left: the material was flown in the reactor when the sent point was 350°C, with some torrefaction apparent (color change from grey to light brown).

Bottom-Right – the material was flown in the reactor when the setpoint was 500°C, with a very clear change in the color (black), indicating a high extent of torrefaction. The rods exiting the extruder die were cooled down and cut mechanically to produce samples for characterization.

Figure 5.27. Mild degradation pellets (left) and (right) high degradation pellets (right).

Figure 5.27 shows two types of material: low torrefaction extruded material (Left) and high torrefaction extruded material (Right). It should be noted that during the torrefaction there is a significant size reduction as can been observed in Figure 5.28 that shows microscopic image (taken by AmScope UM300) of a cross-section of a pellet. In the un-torrefied material, one observes large particles that are encapsulated within molten plastic. The large particles are fiber pieces that did not change their size from its initial value of ~3 mm. In the torrefied material, one observes that all the plastic has melted and the only the fibers are visible. The fiber has significantly smaller particles, in the range

0.06-0.5 mm. This size reduction of 1-2 order of magnitudes is due to the embrittlement of the material and the consequent size reduction due to the shear forces caused by the mechanical rotation of the paddles.

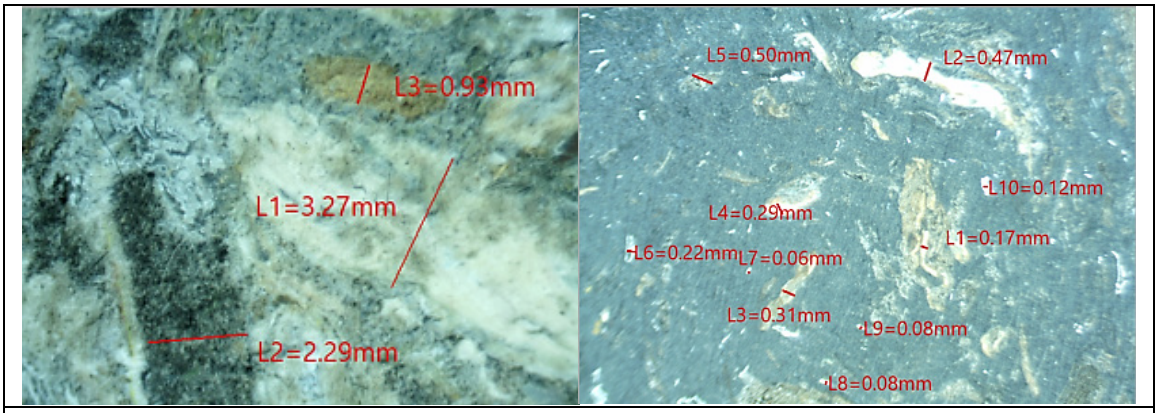

Figure 5.28. Cross-section under a microscope (X4 meginified) of mild degradation pellets (left) and high degradation (right).

One should note an observation regarding the role of the torrefied material as a lubricant. In Section 5.4.4 the specific process energy was discussed showing that although most of the motor the energy is required to overcome the friction in the extruder section, some energy was added when the material was flown in the reactor. We assert that the torrefied material acts as a lubricant thus reduces the process-specific energy in comparison to non-torrefied material. Figure 5.29 shows the motor power vs. shaft rotation frequency for three cases: An empty reactor (open triangle) where the power increases with the rotation frequency. A loaded reactor (at 8.7 kg/hr) at 250°C (no torrefaction) where the motor power is plotted vs. the rotation frequency (solid squares), showing a clear increase of the power. A loaded reactor (at 8.7 kg/hr) at 400°C (with torrefaction) where the motor power is plotted vs. the rotation frequency (solid circles), showing a clear decrease of the power to the values without material.

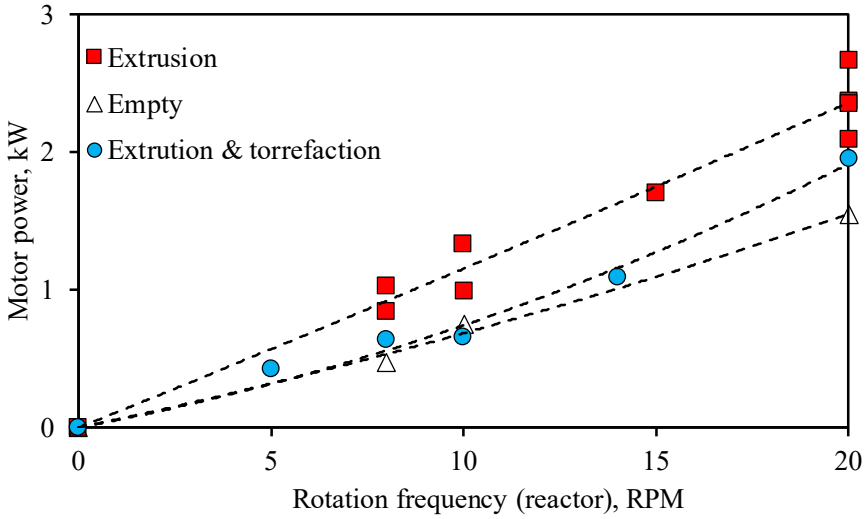

Figure 5.29. Motor power vs. rotation frequency with torrefied material.

5.5.3.1. Pellet characterization

It should be noted that the produced pellets were characterized as those in Chapter (4). The results for all properties except density were identical to those obtained in Chapter (3) and will not be repeated here. The density of the material produced in this reactor is measured and yielded an average value of 850 kg/m^3, in comparison to the 1,100 kg/m^3 obtained for the other pellets. The reason for this difference is that the current extruder L/D value was 6, in comparison to 30 for the other pellets. The higher density pellets required significantly more specific electric energy for the process; for comparison, in the 101.6-mm reactor with L/D=6 the specific energy was found 0.15 MWh/ton (see Section 5.4.4).

One should note that the heating rate within the 101.6-mm reactor is slower than that observed in the 25.4-mm reactor (Chapter (2)). Yet, the 101.6-mm reactor was found to produce non-torrefied and torrefied pellets that are consistent and reproducible. Clearly, the observed heating rates in the 101.6-mm reactor do not fit fast pyrolysis as it requires at

least 50 °C/s. In the next section, we will discuss some modification to increase the heating rate in this reactor.

5.6. Conclusions

This study was carried out in a unique shaft configuration, which is an integration of a paddle mixer, a grinder, and an extruder. The paddle configuration was designed to increase the mixing characteristics (compared to a screw auger) and, in turn, increasing the residence time, and the homogeneity of the material. The extrusion section was designed to densify the material and create a separation of the reaction zone and the environment.

The mass flow rate was studied in this system, showing a linear behavior of mass flow rate with feed auger rotation frequency. The current paddle configuration was found to increase residence time by a factor of 2.3 in comparison to a screw auger. The axial temperature profile was determined from the heating rate from the walls, the mass flow rate, and the residence time. We also defined a characteristic time for radial heating and found that it is significantly smaller than respective axial segment, concluding that the radial temperature is uniform. The temperature profile has been used to estimate the rate and extent of thermal degradation of wastes inside the reactor and was found to have a good fit with experimental results. Microscopic visualization show that the original material size was reduced in size by a factor of 10-30 after existing the extruder. The reduction was attributed the mixing, the reaction and the consequent downsizing.

5.7. Reference

Giles Jr, H. F., Mount III, E. M., & Wagner Jr, J. R. (2004). Extrusion: the definitive processing guide and handbook. William Andrew.

Xu, Z., Zinchik, S., Kolapkar, S. S., Bar-Ziv, E., Hansen, T., Conn, D., & McDonald, A. G. (2018). Properties of Torrefied U.S. Waste Blends. *Frontiers in Energy Research*, *6*(65), 1–13. https://doi.org/10.3389/fenrg.2018.00065

Zinchik, S., Klinger, J. L., Westover, T. L., Donepudi, Y., Hernandez, S., Naber, J. D., & Bar-Ziv, E. (2018). Evaluation of fast pyrolysis feedstock conversion with a mixing paddle reactor. *Fuel Processing Technology*, *171*, 124–132. https://doi.org/10.1016/j.fuproc.2017.11.012

Zinchik, S., Xu, Z., Kolapkar, S. S., Bar-Ziv, E., & McDonald, A. G. (2019). Properties of pellets of Torrefied U.S. Waste Blends. Manuscript submitted to *Waste Management*

6. Overall thesis conclusions

From the above studies, chapter (2) through chapter (5) we can conclude the following:

- Paddle mixers are preferable to screw augers when it comes to mixing and heat transfer and as a consequence are better suited for thermal degradation processes such as torrefaction and pyrolysis. This is due to the better mixing capabilities that generate a more homogeneous blends, thus consistent products.
- The addition of heat transfer material to the operation of the paddle mixer increases significantly the heating rates to 530 °C/s, similar to circulating fluidized bed.

As for the use of waste as a feedstock for torrefaction we can conclude the following:

- We can control the properties of the outcome material by controlling the thermal degradation extent; i.e., heat content, grindability characteristics combustion behavior etc.
- After extrusion the melted plastic encapsulates and protect the thermally treated fibers from the environment those creating a safe, durable and water-resistant pellet.

From the large integrated system we have found the following:

- Integration of the paddle-mixer and extruder in a 10-cm reactor was successful.

- Paddle mixer can process wastes without plugging issues.
- Significant increase of mass flow rate as compared to the 2.5-cm reactor.
- The integrated system has a smaller footprint when compared with an industrial reactor due to the reduction on operating components.

7. Future work

The results obtained above for the 101.6-mm reactor system indicated that some modifications should be made to improve the performance of the reactor. One issue that has not been discussed in this study is the requirement for chlorine removal that can actually be done during torrefaction. Albrecht et al., performed a comparative study on this issue that concluded that longer residence time is required for better reduction of chlorine during torrefaction (Albrecht et al., 2019). The following section relates to increasing the residence time that is suggested by (i) changes in the paddle configuration, and (ii) increasing the initial temperature. Another issue is the application of this system for fast pyrolysis as it requires significantly higher heating rates. In this reactor configuration, higher heating rates can be achieved by an (i) better radial mixing, which can be achieved by different paddle configuration and higher rotation frequency and (ii) significantly smaller particle sizes (100-micron range, in comparison to ~30 mm in the current study).

7.1. Increasing residence time

As for the paddle configuration, we have made a modification in the paddle configuration by doubling the area of the cuts in all flightings. This was expected to increase the residence but also to generate a better mixing. Figure 7.1 shows the paddle configuration made; Left – the original paddle configuration and Right – the modified configuration. The residence time was measured with this new configuration and the results are shown in Figure 7.2, showing a 60% increase in the residence time. Figure 7.3 shows

simulation results that compare the temperature (reaching 300°C) and mass loss vs. residence time for three cases:

- The current configuration, with an initial temperature of 25°C showing that the material temperature barely reached the setpoint and a mass loss of ~8%.
- The configuration with the longer residence time (modified paddles) with an initial temperature of 25°C, showing that temperature reaches the set value at 6.5 minutes and remains at that temperature for ~3 minutes, reaching a mass loss of 22%.
- The configuration with the longer residence time initial temperature of 200°C, showing that the temperature reached the set point at about 4.5 minutes, remains constant for 5.5 minutes, reaching a mass loss of ~30%.

Figure 7.1. Shaft before (left) and after (right) modifications.

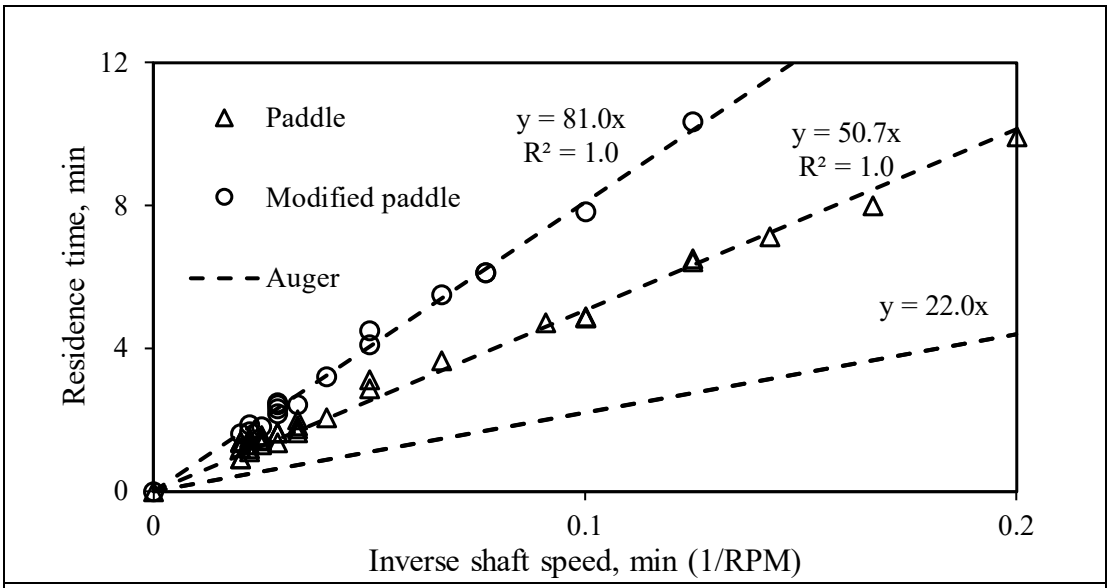

Figure 7.2. Inverse shaft speed vs. residence time with a modified shaft.

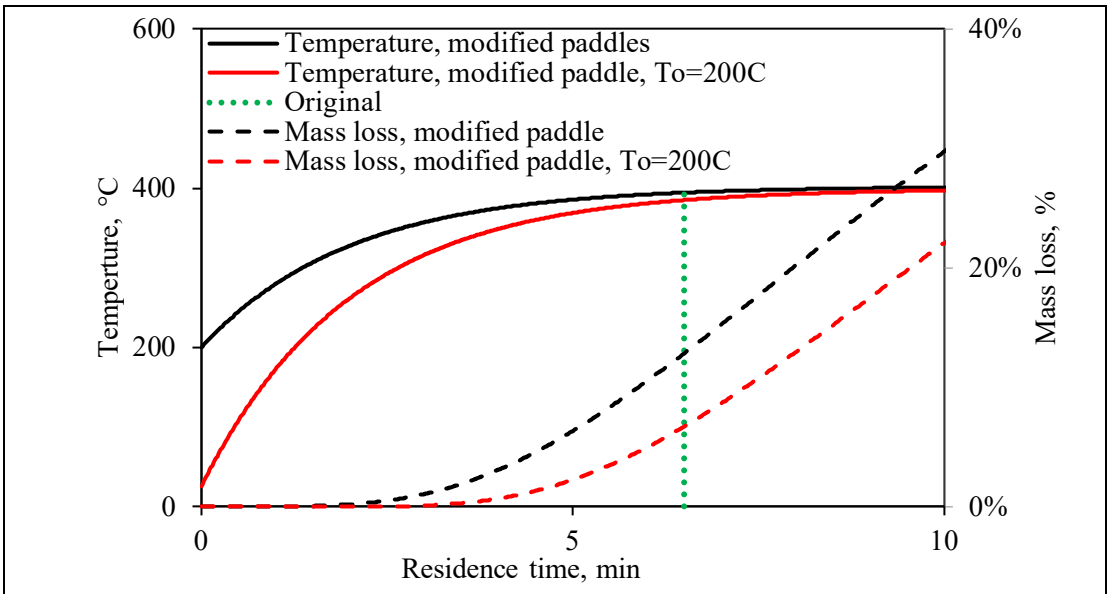

Figure 7.3. Temperature and mass loss simulation. Red – initial temperature is 25°C, Black initial temperature 200°C.

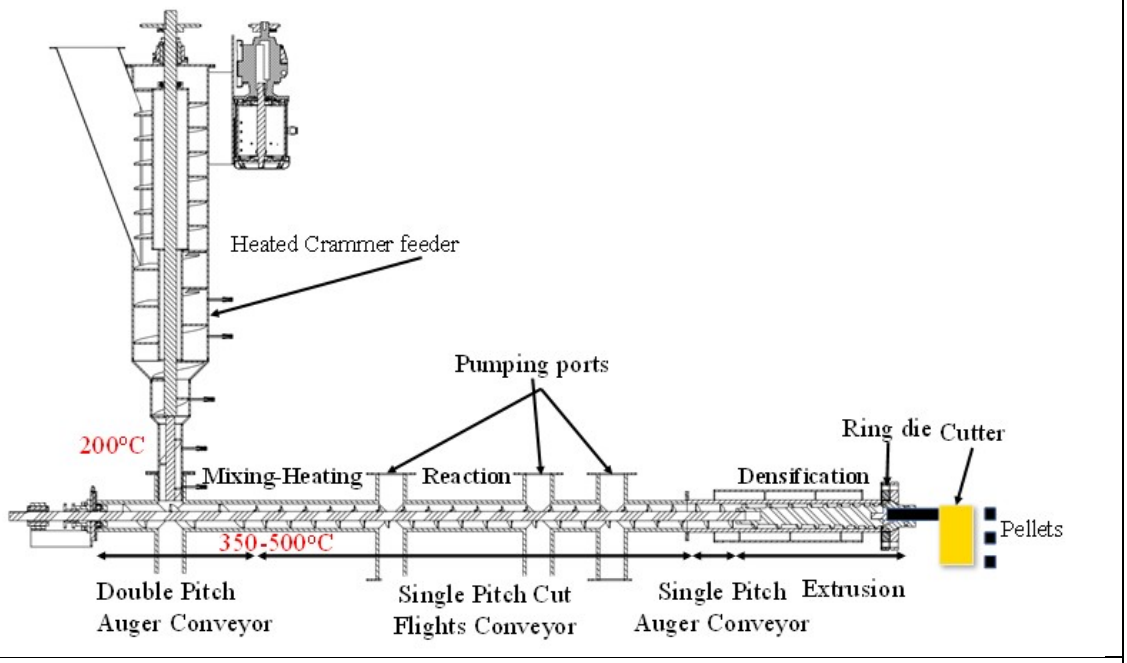

Figure 7.4. New feeding system.

To increase the initial feedstock temperature, a new design for the feedstock feeder was made, fabricated and assembled and preliminary experiments were carried out that indicated clearly that the temperature at the feeder outlet can be adjusted as required. Figure 7.4 shows a drawing of the new feeder assembled in the reactor.

7.2. The decrease in particle size

The particle size has a critical effect on the heating rate. The current characteristic size of the waste samples is about 30 mm, which clearly yielded in slow heating rates of 2-3 °C/s. If the particles would be decreased to 300 microns, the heating rate would increase accordingly. Figure 7.5 presents simulation results for the temperature and mass loss when the particles were pulverized to 300-micron size. The question is, of course, how do we get the waste feedstock to reach this size range. The answer is by partially torrefying the waste

feedstock, it becomes brittle to enable pulverizing the material to any size required. Indeed, in Chapters (3) and (4), grindability was performed to validate this point.

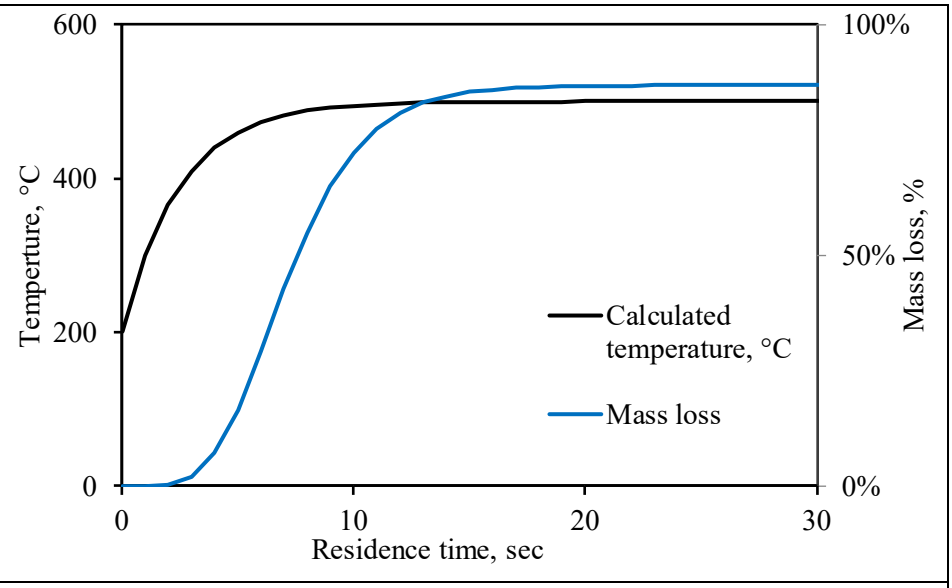

Figure 7.5. Temperature and mass loss simulation with small particles

7.3. Reference

Albrecht, J., Xu, Z., Kolapkar, S. S., Zinchik, S., Bar-Ziv, E., McDonald, A. (2019). "Dechlorination of Industrial Wastes". To be submitted to *Waste Management.*